Fabrication and Characterization of Nanostructured Metallic Thin Films and Periodic Structures for Plasmonic Applications

By

SUDHEER

Enrolment Number: PHYS03201204014

Raja Ramanna Centre for Advanced Technology
Indore-452013, India

A thesis submitted to the

Board of Studies in Physical Sciences

In partial fulfillment of requirements

for the Degree of

DOCTOR OF PHILOSOPHY

of

HOMI BHABHA NATIONAL INSTITUTE

July 2018

Homi Bhabha National Institute

Recommendations of the Viva Voce Committee

As members of the Viva Voce Committee, we certify that we have read the dissertation prepared by Shri Sudheer entitled "Fabrication and characterization of nanostructured metallic thin films and periodic structures for plasmonic applications " and recommend that it may be accepted as fulfilling the thesis requirement for the award of Degree of Doctor of Philosophy.

Chairperson – Dr. Rama Chari	Ramachari	**Date:**	5.7.19
Guide / Convener – Dr. Arvind Kumar Srivastava	Srivastava	**Date:**	5/7/19
Examiner - Dr. A. Mitra	Anirban Mitra	**Date:**	5.7.19
Member - Dr. Tapas Ganguli		**Date:**	05/07/2019
Member - Dr. S.M. Gupta		**Date:**	05.07.2019
Member - Dr. Tarun Kumar Sharma		**Date:**	05.07.2019
Member -Prof. Mohammed Hussein Modi		**Date:**	5.7.19
Member - Dr. Maulindu Kumar Chattopadhyay	M K Chattopadhyay	**Date:**	05/07/2019
External Member - Dr. N.P. Lalla	Niranjan Pd. Lalla	**Date:**	05.07.2019

Final approval and acceptance of this thesis is contingent upon the candidate's submission of the final copies of the thesis to HBNI.

I/We hereby certify that I/we have read this thesis prepared under my/our direction and recommend that it may be accepted as fulfilling the thesis requirement.

Date: 5/7/19

Place: RRCAT

Guide: Srivastava

(Dr. Arvind Kumar Srivastava)

STATEMENT BY AUTHOR

This dissertation has been submitted in partial fulfillment of requirements for an advanced degree at Homi Bhabha National Institute (HBNI) and is deposited in the Library to be made available to borrowers under rules of the HBNI.

Brief quotations from this dissertation are allowable without special permission, provided that accurate acknowledgement of source is made. Requests for permission for extended quotation from or reproduction of this manuscript in whole or in part may be granted by the Competent Authority of HBNI when in his or her judgment the proposed use of the material is in the interests of scholarship. In all other instances, however, permission must be obtained from the author.

Sudheer

Sudheer

DECLARATION

I, hereby declare that the investigation presented in the thesis has been carried out by me. The work is original and has not been submitted earlier as a whole or in part for a degree / diploma at this or any other Institution / University.

Sudheer

Sudheer

List of Publications arising from the thesis

Journal:

Published:

1. Fabrication of large area plasmonic nanoparticle grating structure on silver halide based transmission electron microscope film and its application as a surface-enhanced Raman spectroscopy substrate;
   Sudheer, P. Tiwari, S. Bhartiya, C. Mukherjee, M. N. Singh, A. K. Sinha, V. N. Rai, and A. K. Srivastava
   Journal of Applied Physics, (2015) *118*, 064303 (1-9).

2. Diffraction efficiency of plasmonic gratings fabricated by electron beam lithography using a silver halide film;
   Sudheer, S. Porwal, S. Bhartiya, B. T. Rao, P. Tiwari, Himanshu Srivastava, T. K. Sharma, V. N. Rai, A. K.Srivastava, and P. A. Naik
   Journal of Applied Physics, (2016), *120*, 043101 (1-8).

3. A study of growth and thermal dewetting behavior of ultra-thin gold films using transmission electron microscopy;
   Sudheer, Puspen Mondal, V. N. Rai, A. K. Srivastava
   AIP Advances, (2017), *7:7*, 075303 (1-13).

Communicated:

1. Plasmonic surface relief gratings for tunable optical band-pass filter application;
   Sudheer, S. Porwal, S. Bhartiya, C. Mukherjee, P. Tiwari, T. K. Sharma, V. N. Rai, and A. K. Srivastava, Journal of Applied Physics.

2. Effect of ambient aging on the optical properties of ultra-thin gold films: A detection of enhanced plasmonic response, **Sudheer**, C. Mukherjee, S. Bhartiya, A. K. Sinha, S. K. Rai, V. R. Reddy, V. N. Rai, A. K. Srivastava, Journal of Applied Physics.

Conference/Symposium

1. Large area fabrication of plasmonic nanoparticle grating structure by conventional scanning electron microscope;
   Sudheer, P. Tiwari, C. Mukherjee, V. N. Rai, and, A. K. Srivastava,
   AIP Conf. Proc. **(2015)**, 1665, 050049 (1-3).

2. Plasmonic characterization of photo-induced silver nanoparticles extracted from silver halide based TEM film;
   Sudheer, P. Tiwari, G. K. Varshney, V. N. Rai and A. K. Srivastava,
   AIP Conf. Proc., (2016) 1731, 140035 (1-3).

3. Influence of natural oxidation to control the particle size and enhance the number density during subsequent sputtering growth of silver nanoparticle thin film;
   Sudheer, P. Tiwari, Velaga Srihari, K. K. Pandey, V. N. Rai, A. K. Srivastava and P.A. Naik,
   AIP Conf. Proc. (2017) 1832, 140040 (1-3).

4. Superiority of localized surface plasmon resonance technique in characterization of ultra-thin metallic films;
   Sudheer, P. Tiwari1, S. Bhartiya, C. Mukherjee, S. K. Rai, A. K. Sinha, V. N. Rai, A. K. Srivastava,
   J. Phys.: Conf. Ser.(2017) 961, 012013 (1-6).

5. Experimental investigation of room temperature instability in sputtered grown ultra-thin gold films using transmission spectroscopy and x-ray reflectivity techniques;
   Sudheer, C. Mukherjee, S. K. Rai, V. N. Rai, A. K. Srivastava
   AIP Conf. Proc. (2018) 1942, 050103 (1-5).

Sudheer

Sudheer

I dedicate this thesis to

My Family

ACKNOWLEDGEMENTS

The present thesis is the part of research work that has been done since my joining in RRCAT as a research scholar. The constant support, enormous contribution and ample affection of a great number of people from a different disciple of the RRCAT Indore and other institutes made me able to complete the research work and bring this thesis to its presentable form.

First of all, I thanks to my Ph. D. supervisor **Dr. A. K. Srivastava**, for introducing me with the fascinating field of nanophotonics and especially the importance of plasmonics in the current research of nanotechnology. I owe my deep sense of gratitude to him for the successful completion of this thesis. He infused enthusiasm at every step in my research work and made me realized my potential and passion for research. His continuous encouragement, constant support, valuable suggestions along with constructive criticism were always productive for my research work. He thought me, how should do the proper planning to perform the series of experiments for the appropriate outcome of the research work. I certainly benefited with his profound experimental skills and analytical expertise and immense basic conceptual knowledge throughout the Ph.D. tenure. The willingness to share his knowledge and experience, keeping a high level of patience and ability to keep the person motivated also broadened my perspective. It was a wonderful and rich experience for me to work under him.

I am extremely thankful **Dr. Pragya Tiwari**, for helping me in various aspects including counsels, enthusiastic support and all kinds of freedom for the research work throughout Ph.D. tenure. Her disciplined attitude full of politeness and hardworking nature has left a deep impression on me. I am very much thankful to her for giving me moral support during the project work.

I sincerely give special gratitude to **Dr. V. N. Rai**, for helping me in analysis and interpretation of the scientific results as well as support in writing manuscripts that eventually helped me in achieving the targets throughout my Ph.D. work.

I thank Lithography & Microscopy Laboratory group members especially **Dr. Pragya Tiwari, Dr. Himanshu Srivastava, Mr. Puspen Mondal and Mr. Mahendra Babu** for assist in learning the basic concept and operation of sputtering system, scanning electron microscopy (SEM), field emission scanning electron microscopy (FESEM), energy dispersive spectroscopy (EDS), transmission electron microscopy (TEM), clean room technologies and also for help at every step of research work for my betterment. I also thank Dr. Himanshu Srivastava for Matlab programming for simulating the diffraction efficiency curves for plasmonic grating structures.

I would like to thanks to **Dr. A. K. Sinha**, Mr. M. N. Singh, Dr. Archna Sagdeo and Mr. Anuj Upadhyay for x-ray XRD measurement beam-line-12 of Indus-2 and fruitful discussion.

I sincerely thank to **Dr. C. Mukherjee**, Mr. Rajiv Kamparath and Mr. Naveen Sharma of optical coatings laboratory, RRCAT for absorbance and atomic force microscopy (AFM) measurements. The highly disciplined nature full of benevolence and sportive attitude of Dr. Mukherjee always motivates me.

I especially thank **Dr. T. K. Sharma** and **Mr. S. Porwal** for assembling the custom-made setup for diffraction efficiency measurement of plasmonic grating structures and helping me to understand the recorded data.

I thank **Dr. B. T. Rao** and **Kum. Shweta Verma** of Materials Engineering Section of RRCAT for absorbance measurement of grating and gave important suggestions during manuscript writing. His hardworking and enthusiasm in nature always motivated me.

My thanks are due to **Mrs. S. Bhartiya** of Laser Materials Section of RRCAT for performing AFM measurements of nanostructured Au thin film and grating structures.

I would like to thanks to **Dr. M. K. Tiwari,** Mr. Ajay Khooha and Mr. Ajit Kumar Singh for XRR at beam-line-16 of Indus-2.

I would like to thanks to **Dr. Velaga Srihari** and **Dr. K. K. Pandey** of High Pressure and Synchrotron Radiation Physics Division (HP&SRPD), Bhabha atomic Research Centre (BARC) for XRD and GIXRD measurements at beam-line-11.

I am thankful to **Dr. S. K. Majumder, Mr. H. S. Patel** and Mr. Sandeep Kumar of Laser Biomedical Applications Section for providing active help in surface-enhanced Raman spectroscopy (SERS) measurements

My thanks are due to **Dr. S. K. Rai** for allowing me to performs XRR measurement, **Mr. Ashok Kumar** for analyzing the XRD data and Mr. **Rajnish Dhawan** for helping in XRR fitting.

I am indebted to members of Indus-2 operation crew without their valuable support it would have been not possible to measure data on synchrotrons beam-lines.

My thanks are due to **Dr. V. R. Reddy** and **Mr. Anil Gome** of IUC Indore for x-ray reflectivity (XRR) measurement. My thanks are due to **Dr. Dilip Gupta**, Ms. Sadhana Singh and Arun Singh Dev of IUC Indore for many conductive discussion.

I sincerely thank our **HBNI Doctoral** members (current and previous) especially Dr. (Ms.) Rama Chari (Chairmen), Dr. Tapas Ganguli (Co-chairmen), Dr. N. P. Lalla (External member, UGC DAE CSR Indore), Dr. S. M. Gupta, Dr. T. K. Sharma, Dr. M. H. Modi, Dr. M. K. Chattopadhyay, Dr. S. M. Oak , Dr. S. K. Dev, Dr. G. S. Lodha, Dr. H. S. Rawat, Dr. S. K. Dixit, Dr. Aparna Chakraborty for their monitoring research work, continuous care and guidance in over the past years.

I am very grateful to **Dr. P. A. Naik,** Director RRCAT for his consistent help, advice and cooperation during my stay in RRCAT. His guidance for me started since my interview for selection in the Ph.D. programme, he was the chairmen of the interview committee, is continued as head of ISUD division. I am extremely thankful for Dr. Naik to give permission for the entry of personal computer in the technical area for research work.

I am also grateful to **Dr. Arup Banerjee (Dean Academic)**, **Dr. C. P. Paul (Dean Student Affairs)** and all professors/associated professors who tough us as during 1styear course work. I especially thank **Dr. M. P. Singh** and **Dr. H. Ghosh** for various scientific discussions.

Further appreciation and thanks to all **Synchrotrons Utilization Section (SUS)** and other division members including Dr. Ravindra Jangir, Mr. Suraj Das, Dr. Pooja Gupta, Dr. C. Kamal, Mr. Kiran Baraik, Mr. Arijit Das, Dr. S. D. Singh, Dr. Shailendra Kumar, Madhusmita Baral, Nageswararao Pothana, Praveen Yadav, Dr. M. Nayak, Dr. Rahul Shukla and Dr.V. P. Dhamgaye etc.

I thank **my school and B.Sc. friends**: Pawan Kumar Sharma, Manoj Kumar Dularia, Mohan Lal Kumawat, Gauri Sankar, Pappa, and Jitendra et al.

I thank **my M.Sc. friends**: Anmol Singh, Sunil Soni, Kaidar Mal Jangir, Praveen, Neelam, and Sanju et al.

I thank to **my Ph.D. friends**: Dr. C. Banerjee, Dr. P. C. Pradhan, Dr. A. N. Pandey, Dr. G. Das, S. Kintali, Dr. T. Roy, Dr. D. Mondal, Dr. A. Chakraborty, Dr. V. Gupta, S. Saxena, Sandeep Kumar, Subhash Prajapati, Dr. G. K. Varshney, Dr. Paromita Sarbadhikary, Dr. H. Chandra, Dr. K. K. Mondal, Dr. E. Rani, Dr. S. Sundar. Dr. A. Singh, Sudhir Joshi, Hemant Krishna, Khan Mohambat Khan, Dr. Y. kalkal, Dr. S. Sen, Dr. D. Jana, Dipanjana, Mangalika, Ajam, Avdhesh, Abyay, Subhomoy, Sahdeb, Charu, Dhanshree, Preeti, Sabina, Somya, Sumit, Rijul, Mudi, Nitish, Jinoop, Soumyadeep, Megha, Kavish, Ayushi, Arkadev, Majhi, Subhash, Arshdeep, Vikas, Rahul Rana, Sona Chandran, Rinki Dhingra,Vijay Pal Verama, Ramjaan, Durga, Rajiv, Parth, Saurab, Sumit, Kiran, Surekha, Mahesh, Prachi, Ashutosh, Shiv, Julfikar, Akshita, Geeta, etc..

I am conveying my inmost sense of gratitude to my respected parents, brothers, sisters and relatives for their continuous encouragement, love and affection. It would have not been possible to accomplish the goal without their moral support.

Last but not least, I would like to thank God for giving me strength for achieving this happiest moment of life.

Contents

Summary

Research on plasmonic nanostructured thin films and periodic structures is constantly expanding, covering a wide range of materials, for useful technological applications. The self-organized nanostructured plasmonic thin films and periodic plasmonic nanostructures mostly based on noble elements silver (Ag) and gold (Au) have wide potential applications in the field of the solar cell, sub-wavelength waveguide, and optical response based chemical, biological and gas sensors. The thesis is mainly focused on the fabrication of plasmonic nanostructured thin films and period structures for surface-enhanced Raman spectroscopy (SERS) and optical diffraction studies. The effect of various process parameters (sputtering current, deposition time, annealing temperature, and dwelling time) on growth and post-deposition thermal dewetting of the nanostructured gold thin film is studied using ex-situ and in-situ transmission electron microscope imaging as well as by electron diffraction techniques. The effects of various process parameters (sputtering current and deposition time) on localized surface plasmon resonance (LSPR) characteristic of the nanostructured gold thin film are also studied using absorption spectroscopy. The change in LSPR characteristics with thickness is correlated the different type of morphology present in the as-deposited samples. The instability in LSPR response of the nanostructured gold thin film at ambient temperature is also investigated by recording the absorbance spectra at various stages of aging. The island film shows ~70 nm blue shift in LSPR peak position and 105 nm reduction in its broadening after 120 days of aging. The rate of the blue shift in plasmonic peak for island film is fitted with single exponential decay having 19.3 days time constant. The continuous film also shows the void formation of ~95 nm in size after 30 days of aging which is responsible to excite LSPR in the film. Along with the work on thin films, the fabrication of large-area plasmonic nanoparticle arrays is carried out using a conventional scanning electron microscope (SEM). The raster scan of the electron beam in conventional SEM system is used to fabricate the silver nanoparticle arrays of the different period (2.5, 3.4, 5, and 10 microns) and different depth (~20-500 nm) on silver halide based film. A matrix of eighteen identical or different plasmonic nanoparticle arrays of about 12.5 mm^2 area can be integrated on a 40 mm by 20 mm size sample in a single processing cycle. The electron beam exposure time was very short (<20 s) for the fabrication of an array in the matrix. The fabricated nanoparticle grating structures are used as a SERS substrate. The 10 μm period grating provides an enhancement by two orders of magnitude in comparison to the sputtered deposited silver nanoparticle film. As the period of the grating reduces 10 to 2.5 μm additional three-time enhancement in the SERS signal is achieved. Accelerating voltage of electron beam (10, 15, and 30 keV) is also used to change the depth and shape of the silver nanoparticles grating structures. The fabricated plasmonic gratings also found application in tuning the optical diffraction efficiency (2.8 to 7.2 %) as well as band width (200-400 nm). Maximum 7.2% optical diffraction efficiency is achieved for grating fabricated at 15 keV.

List of Figures

List of Tables

Chapter 1

Introduction

1.1 Foreword

The nanostructured metallic thin films and periodic structures have become two of the most contemporary plasmonic structures for chemical sensors, surface-enhanced Raman spectroscopy and nanophotonics devices applications in the visible to the infrared spectral range. The nanostructured metallic thin films are self-organized structures grown during the early stage of thin film deposition or formed by transformation of the continuous film during post-deposition annealing called dewetting. However, metallic periodic structures are lithographically fabricated pattern structures. Both self-assembled and patterned metallic structures show extraordinary light-matter interaction via collective oscillation of conduction band electron called localized surface plasmon resonance (LSPR). In the present thesis, both metallic nanostructured thin films having various morphologies (island as well as percolated) and nanoparticles embedded grating structures supporting to LSPR are the systems of interest.

In the starting part of the introduction, the brief history of the plasmonics, the major observations achieved by the researchers in the past and the glimpse of up-to-date overview of the field is summarized. In the following sections, a short description of optical properties of metallic nanoparticles in broad frequency range is described that forms a background to study the surface plasmons. Further, the classification and the key equations for excitation of propagating and localized surface plasmon (PSP and LSP) will be presented. In the subsequent section of the chapter, the types of plasmonic structures required for excitation of LSP along with various available fabrication techniques are discussed. After that potential modern application of plasmonic structures, recent trends and current status followed by pertaining issues and challenges of the field are pointed out. Finally, motivation behind the carried out work is presented. This chapter closes with the plan of organization of rest of the chapters in the thesis.

1.2 History of plasmonics

Plasmonics is known since long back and it was frequently used in home decoration, architecture and artwork in the Egypt and China during 4th or 5th century BC. The famous Lycurgus Cup engineered by Romans technologist in the 4th century (presently located in British Museum London) and stained glass artisans are the two most chronicle example for the existence of plasmonic in the past. In both of these objects, gold (Au) and silver (Ag) nanoparticles are used to produce ruby red and deep yellow color respectively. Firstly, Faraday reported variation in colour ranging from ruby red to amethyst in colloidal particles in 1857 [1]. In 1904 Maxwell-Garrett gave the *"Effective Medium Theory"* which rationalized the color of different metal nanoparticles [2]. At present, it is well known that different sizes and shapes of metal nanoparticles define the change in the color due to suspenseful variation in the material properties at the nanoscale [3]. Although, the characteristic color of metal nanoparticles originate from the vigorous interaction with light, so a robust understanding of the optical properties of nanostructures was necessary for concrete direction of the field. During the early 19th century, other scientists also worked on the metal nano-cluster systems, but in-depth theoretical explanation on primary optical properties (absorption, scattering and extinction) of metal cluster published by Gustav Mie in 1908 is highly recognized [4]. The "*Mie Theory*" established the basis of the insight understanding of optical properties of metal nanoparticles and presently it provides the first guideline for the simulation of experimental response of complex metal nanoparticles through numerical modelling. Meanwhile, in 1928 Indian scientists Raman and Krishnan experimentally measured the characteristic inelastic scattering of light corresponding to vibrational modes of a molecule, known as "*Raman scattering*" [5]. The feeble intensity of the Raman signal (14 orders weaker in comparison to the Fluorescence) was the primary barrier in the pertinent applicability for more than half-century. The boom in the field of plasmonics came in 1977, when Jeanmaire and Van Duyne discovered the Surface-Enhanced Raman Scattering (SERS), in which weak Raman signal was enhanced using roughened metal surface [6]. After that, the field of plasmonics quickly expanded and turned the attention of researcher for a wide range of potential applications in chemical and biological science. In 1998, the reports on extraordinary transmission and absorption of light through the hole-arrays in metallic sheet also explosively invited enormous number of researchers to pursue the work in the field of nanophotonics [7]. At present, availability of advanced fabrication techniques, high sensitivity optical characterization and speedy modern computational methods for potent numerical modelling set many benchmarks in the sub-wavelengths waveguide for transportation of light, plasmonic mirrors, solar cells, catalysis and SERS [8]–[11]. The interaction of electromagnetic radiation with metallic nanoparticles is described in next section in terms of dielectric function of metals.

1.3 Dielectric function of the metals

The optical properties of metals is described by "*Drude theory"* of free electrons. In which a gas of electron can freely move around the fixed positive lattice cores, which is known as "*plasma model"*. In this model, screening of the free electrons due to the bound electron (the effect of inter-band transition) and electron-electron interaction are not taken into account. The collision of free electron with the positive lattice can only damp their motion. In the presence of external electromagnetic field *E*, the electrons oscillate, and the movement of an electron can be written by the following equation [12]

$$m_e \frac{d^2r}{dt^2} + m_e \gamma \frac{dr}{dt} = -eE \qquad \textbf{1.1}$$

where e is the charge on free electron. The γ and m_e are damping constant and effective optical mass respectively. For driving field $E = E_0 e^{-i\omega t}$, the solution of the above equation 1.1 can be written as $r = r_0 \, e^{-i\omega t}$ and by solving the equation 1.1

$$m_e(-i\omega)^2 r_0 e^{-i\omega t} + m\gamma(-i\omega) r_0 e^{-i\omega t} = -eE_0 e^{-i\omega t}$$

$$-m_e \omega^2 r_0 - im\omega\gamma\, r_0 = -eE_0$$

we obtained the amplitude (r_0) of the displaced electrons as

$$r_0 = \frac{eE_0}{m_e(\omega^2 + i\omega\gamma)} \qquad \textbf{1.2}$$

If p is the dipole moment for the displaced electrons then it can be defined as

$$p = -er_0 = \frac{-e^2 E_0}{m_e(\omega^2 + i\omega\gamma)} \qquad \textbf{1.3}$$

The dipole moment per unit volume called polarization P can be defined as

$$P = np = \frac{-ne^2 E_0}{m_e(\omega^2 + i\omega\gamma)} \qquad \textbf{1.4}$$

where n is the number density of free electrons. The dielectric function of the free electron gas can be defined as [13]

$$\varepsilon(\omega) = 1 + \frac{P}{\varepsilon_0 E_0} = 1 - \frac{ne^2}{m_e \varepsilon_0 (\omega^2 + i\omega\gamma)} = 1 - \frac{\omega_p^2}{(\omega^2 + i\omega\gamma)} \qquad \textbf{1.5}$$

where $\omega_p = (ne^2 / m_e \varepsilon_0)^{1/2}$ is the plasma frequency of free or conduction band electrons and ε_0 (8.85×10^{-12} F/m) is the permittivity of the vacuum. The dielectric function presents the response of the damped oscillations of the free electrons in the electromagnetic field which is the complex quantity and can also be written as

$$\varepsilon(\omega) = \varepsilon_1(\omega) + i\varepsilon_2(\omega)$$

Here $\varepsilon_1(\omega)$ and $\varepsilon_2(\omega)$ are the real and imaginary part of the material dielectric function. Now the equation 1.5 can also be written in the following form

$$\varepsilon(\omega) = 1 - \frac{\omega_p^2}{(\omega^2 + \gamma^2)} + \frac{i\omega_p^2\gamma}{\omega(\omega^2 + \gamma^2)}$$

Now the real and imaginary part of the dielectric function $\varepsilon(\omega)$ can be separated as

$$\varepsilon_1(\omega) = 1 - \frac{\omega_p^2}{(\omega^2 + \gamma^2)}; \ \varepsilon_2(\omega) = \frac{\omega_p^2\gamma}{\omega(\omega^2 + \gamma^2)} \qquad \textbf{1.6}$$

In plasma model the γ for a free electron is about 100 THz at room temperature. In the visible and infrared wavelength range, when $\omega >> \gamma$ (negligible damping) then the real and imaginary part of the dielectric function $\varepsilon(\omega)$ become like free-electron metals and can be written as

$$\varepsilon_1(\omega) = 1 - \frac{\omega_p^2}{\omega^2}; \qquad \varepsilon_2(\omega) = \frac{\omega_p^2 \gamma}{\omega^3} \qquad \textbf{1.7}$$

The equation 1.7 tells that the real part of the dielectric $\varepsilon_1(\omega)$ becomes zero at $\omega = \omega_p$. This frequency is named as volume plasmon frequency, which is the characteristic of material.

1.4 Bulk plasmon

The collective longitudinal oscillation of the conduction electron with respect to the fixed positive background of the ion cores is called bulk plasmon. The schematic diagram in Figure 1.1 indicates a collective shift of electron gas in metal plate by a displacement "u" leads to a surface charge density $\sigma = \pm neu$ at the plate edge. Where n and e are the number density and charge of the electron respectively. This creates a uniform electric field $E = neu / \varepsilon_0$ inside the plate.

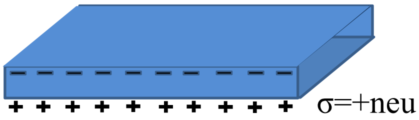

Figure 1.1 Schematic of the metal plate showing surface charge density distribution during longitudinal collective oscillation of conduction band electron [12].

The uniform electric field will exert a coulombic restoring force on the shifted electron gas and if we ignore retardation by collision with ion core then their moment can be defined by the following equation

$$nm_e \frac{d^2u}{dt^2} = -neE \qquad \textbf{1.8}$$

Inserting the expression for the electric field $E = E_0 e^{-i\omega t}$ in equation 1.8, then we obtained the equation as

$$\frac{d^2u}{dt^2} + \omega_p^2 u = 0 \qquad \textbf{1.9}$$

where $\omega_p = (ne^2/m_e\varepsilon_0)^{1/2}$ is called the characteristic frequency of natural free oscillation of the electron gas. Note that the above expression is derived for the large wavelength values in which electron move coherently. The quanta of these free charge oscillations are called bulk plasmon. The bulk plasmon can only be generated by particles striking due to its longitudinal nature and do not link with the transverse electromagnetic waves. In bulk state, plasmon energy E_p can be define as

$$E_p = \hbar\omega_p = \hbar\sqrt{\frac{ne^2}{m_e\varepsilon_0}} \qquad \textbf{1.10}$$

where $\hbar$ *(1.054×10^{-34} J-s)* is the Plank′s constant. In the next section the key relationship is derived for the interaction of metals with electromagnetic wave that has been presented for both PSP and LSP. Especially, for LSP the critical dependency of key equation on parameters like material composition, particle size, and, shape as well as surrounding medium are explained for simulation of experimental plasmonic response.

1.5 Surface plasmon

The coupling of incident light with the free electron gas of the metal film or nanostructures is known as surface plasmon [9], [13]. The surface plasmon are mostly classified as PSPs and LSPs depending on nature and the type of interaction as well as on the feature sizes of the material. For excitation of the PSPs, phase matching techniques are required, while LSPs can be generated by direct light. We shall not look into the vast area of PSPs and will limit our self upto its basic introduction. There are several contemporary and recent reviews which covers in-depth development and explanation of this topic. Here, we have focused our attention for better understanding of the basics of LSPs and exploring its potential applications [14].

1.5.1 Propagating surface plasmon

The propagating surface plasmon (PSP) is also termed as surface plasmon polariton (SPP). The nature of SPP electromagnetic wave is dispersive [15]. These are associated with the smooth metal (Ag and Au) thin films (about 20-200 nm thick) or corrugated metallic surface wherein plasmon experiences a constraint due to planer metal/dielectric interface or periodic metal surfaces. On the smooth metallic surfaces, the mixed electromagnetic as well as surface charge characteristics of surface plasmon are strongly delimited to the metal/dielectric interface. An enhanced field is created in the vicinity of metal/dielectric interface in perpendicular direction due to its peculiar dual character. The strength of the enhanced field is evanescent that decrease exponentially with distance. The decay length of the field in a dielectric material (δ_d) is equal to about the half of the wavelength of light used, whereas in the metal (δ_m) it is obtained by the skin depth. When light is transformed into SPP mode, then it can travel on metal surface but attenuated continuously due to the losses originating from absorption in the metal. The propagation length defined by δ_{sp} and it depends on the type of metal.

The simplest configuration sustaining to PSP is the single interface between the dielectric (z>0) and metal (z<0) as shown in Figure 1.2. The dielectric should be non-absorbing with positive dielectric constant (ε_d). For the metal, real part of the dielectric function Re[$\varepsilon_m(\omega)$] should be less than zero. If the electric and magnetic component of incident light (transverse electromagnetic waves) have following equation

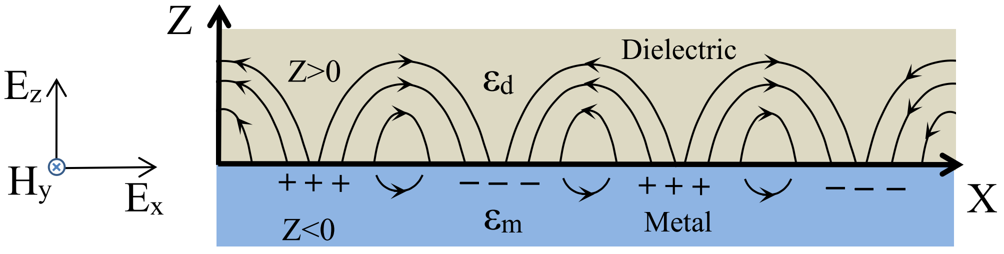

Figure 1.2 Schematic of geometry of metal/dielectric interface with coordinate system for the propagating surface plasmon generation [10].

$$E_y = 0, E_x, E_z \neq 0;\ H_x = H_z = 0, H_y \neq 0$$

$$H_{yd}(x,z,t) = H_{yd}\exp^{i(k_{xd}x+k_{zd}z-\omega t)}; H_{ym}(x,z,t) = H_{ym}\exp^{i(k_{xm}x-k_{zm}z-\omega t)}$$

$$E_{xd}(x,z,t) = E_{xd}\exp^{i(k_{xd}x+k_{zd}z-\omega t)}; E_{xm}(x,z,t) = E_{xm}\exp^{i(k_{xm}x+k_{zm}z-\omega t)}$$

$$E_{zd}(x,z,t) = E_{zd}\exp^{i(k_{xd}x+k_{zd}z-\omega t)}; E_{zm}(x,z,t) = E_{zm}\exp^{i(k_{xm}x+k_{zm}z-\omega t)}$$

From the Maxwell equation

$$\nabla \times H = \left(\frac{\varepsilon}{c}\right)\frac{\partial E}{dt}$$

From the boundary conditions at the interface (z=0) $E_{xm} = E_{xd}$; $H_{ym} = H_{yd}$; $\varepsilon_m E_{zm} = \varepsilon_d E_{zd}$; $k_{xm} = k_{xd} = k_x$ we can get the following equation

$$\frac{k_{zm}}{k_{zd}} = -\frac{\varepsilon_m}{\varepsilon_{zd}} \qquad \textbf{1.11}$$

From the wave equation $\nabla^2 H - \frac{\varepsilon}{c^2}\frac{\partial^2 D}{dt^2} = 0$; and from equation 1.11 we get

$$k_x = \frac{\omega}{c}\sqrt{\frac{\varepsilon_m \varepsilon_d}{\varepsilon_m + \varepsilon_d}} \;;\; k_{zd} = \frac{\omega}{c}\sqrt{\frac{\varepsilon_d^2}{\varepsilon_m + \varepsilon_d}} \;;\; k_{zm} = \frac{\omega}{c}\sqrt{\frac{\varepsilon_m^2}{\varepsilon_m + \varepsilon_d}} \qquad \textbf{1.12}$$

For Re (ε_m) < 0, $|\varepsilon_m| > |\varepsilon_d|$, k_x be real but both k_{zd} and k_{zm} will be imaginary. So, SPP travels along the x-axis at interface but attenuated along the z-axis in both metal and dielectric medium. From equation 1.12, for $\varepsilon_m = -\varepsilon_d$, k_x will be maximum. From equation 1.7

$$\varepsilon_m = 1 - \frac{\omega_p^2}{\omega^2} = -\varepsilon_d; \;\; \omega^2 = \frac{\omega_p^2}{1+\varepsilon_d} = \omega_{sp}^2$$

or

$$\omega_{sp} = \frac{\omega_p}{\sqrt{1+\varepsilon_d}} \qquad \textbf{1.13}$$

For vacuum (ε_d=1), the excitation frequency for propagating plasmon will be $\omega_{sp} = \frac{\omega_p}{\sqrt{2}}$, which is the maximum frequency for a particular metallic thin film. As ε_d of dielectric medium increases the ω_{sp} decreases. So, for any other dielectric medium ω_{sp} will be small in comparison to the vacuum. Propagation length of SPP at metal air-interface in x-direction can be obtained by

$$k_x = k_x^{'} + ik_x^{''} = \frac{\omega}{c}\sqrt{\frac{\varepsilon_m}{\varepsilon_m + 1}} \qquad \textbf{1.14}$$

where $E_x = E_0 \exp^{ik_x x} = E_0 e^{ik_x^{'} x} e^{-k_x^{''} x}$, in which first term $e^{ik_x^{'} x}$ is propagating term and second term $e^{-k_x^{''} x}$ is decay term in x-direction that finally decides the propagation length for SPP. Similar to the smooth metal/dielectric surface, SPP can be excited on the metallic grating structures. In the grating structures electromagnetic field enhancement occurred on the periodic surfaces. For both the cases (smooth metal/dielectric surface and metallic gratings) experiment has to be done in reflection geometry to excite the SPP. In reflection geometry, wavelength and angle matching is required to realize the SPP excitation. For a fixed wavelength (λ_{ext}), scanning of incident angle θ is performed with polarized light for SPP excitation. In the angle scanning, the specular reflection shows an extraordinary minima at particular incident angle which is characteristic of SPP excitation. In case of grating, amplitude (height) decide the position (λ_{spp}) and broadening (β_{spp}) of SPP minima for a fixed grating material and fixed grating period. For higher higher grating amplitude SPP minima position will appear at higher angle along with higher broadening. The Kretschmann and Otto geometry are well known to excite the SPP on smooth and corrugated metallic surfaces, more details on this topic can be found in the book published by Raether Heinz [15].

1.5.2 Localized surface plasmon

The localized surface plasmons (LSPs) are the non-propagating excitation of coherent charge oscillations of free electrons confined to the metallic nanostructures [13]. This mode originates typically by the scattering from sub-wavelength metal nanostructures in the presence of oscillatory electromagnetic field (light). To obtain the critical formulation for the excitation of localized surface plasmon resonance (LSPR), we have dealt with a single spherical metal nanoparticle of radius '*a*' interacting with x-propagating and z-polarized light of wavelength λ. The dielectric constant of the homogeneous metal sphere is ε_m, which is taken as constant that is independent of particle size, where as the dielectric constant of isotropic and non-absorbing surrounding medium is ε_d as shown in Figure 1.3. The electric field vector of the incident z-polarized light can be presented as

$$E = E_0\hat{z} \tag{1.15}$$

Where $\hat{z}$ is the unit vector along the z-axis. In quasi-static approximation ($a<<\lambda$) the phase of the harmonically oscillating field is practically constant over the whole particle volume. Such kind of problems can be treated as particle in the electrostatic field. The solution of the problem can be obtained using the Laplace equation for electric potential (For details of full derivation see references [10],[13], [16]) and

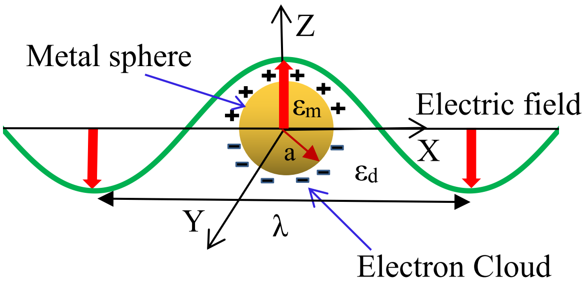

Figure 1.3 The schematic localized surface plasmon resonance excitation in a sphere of radius *r* surrounded by a dielectric medium via irradiated of x-propagating and z-polarized light.

finally the electric field inside (E_{in}) and outside (E_{out}) the metal sphere can be presented by the following equation

$$E_{in}(x,y,z) = \left[\frac{3\varepsilon_d}{\varepsilon_m + 2\varepsilon_d}\right]E_0\hat{z} \tag{1.16}$$

$$E_{out}(x,y,z) = E_0\hat{z} - \left[\frac{\varepsilon_m - \varepsilon_d}{\varepsilon_m + 2\varepsilon_d}\right] a^3 E_0 \left[\frac{\hat{z}}{r^3} - \frac{3z}{r^5}(x\hat{X} + y\hat{Y} + z\hat{z})\right] \qquad \mathbf{1.17}$$

In equation 1.17 first term is due to incident the electric field and second term appears is due to dipole moment of nanoparticle. The dipole moment of the metal nanoparticle *P is* obtained as

$$P = 4\pi\varepsilon_0\varepsilon_d a^3 \left[\frac{\varepsilon_m - \varepsilon_d}{\varepsilon_m + 2\varepsilon_d}\right] E_0 \qquad \mathbf{1.18}$$

From the relation $P = \varepsilon_0\varepsilon_d \alpha E$ we can obtained polarizability α as

$$\alpha = 4\pi a^3 \left[\frac{\varepsilon_m - \varepsilon_d}{\varepsilon_m + 2\varepsilon_d}\right] = 3V_0 \left[\frac{\varepsilon_m - \varepsilon_d}{\varepsilon_m + 2\varepsilon_d}\right] \qquad \mathbf{1.19}$$

Where $V_0 = 4/3\pi a^3$ is the particle volume. From both equations 1.16 and equation 1.17 it can be concluded that the field will be maximum inside as well as outside when $|\varepsilon_m(\omega)+2\varepsilon_d(\omega)|$ or $|\varepsilon_1(\omega)+2\varepsilon_d(\omega)|^2 + |\varepsilon_2(\omega)|^2$ is minimum, where ω is the frequency of light. The metal particle also shows maximum polarizability in this situation. If $\varepsilon_2(\omega)$ of the metal nanoparticle is weakly dependent on the frequency, and the absolute value is very small. Then $\varepsilon_1(\omega) = -2\varepsilon_d(\omega)$ should hold under the resonance condition. This condition is known as ***Fröhlich condition***. Earlier we have described that dielectric function of metal is dependent on the incident frequency. So, using the equation 1.16 we have obtained

$$\varepsilon_1(\omega) \approx 1 - \frac{\omega_p^2}{\omega_{\max}^2} = -2\varepsilon_d$$

$$\omega_{\max} = \frac{\omega_p}{\sqrt{1 + 2\varepsilon_d}} \qquad \mathbf{1.20}$$

Where ω_{max} is the frequency of resonance. The equation 1.20 renders the good approximation of resonance frequency of LSPR phenomena for metal particles embedded in medium. For vacuum (ε_d =1) the equation 1.20 become as

$$\omega_{\max} = \frac{\omega_p}{\sqrt{3}} \qquad \textbf{1.21}$$

Equation 1.21 tells that LSPR frequency is less than the bulk plasmon frequency for a particular material.

1.6 Extinction spectra

Using the Mie theory, the extinction cross-section C_{ext} ($C_{ext}=C_{abs}+C_{sca}$, C_{abs} is absorption cross-section and C_{sca} is scattering cross-section) of the homogeneous particles embedded in an isotropic medium is represented as $C_{ext} = \frac{2\pi}{k^2}\sum_{v}^{\infty}(2v+1)\mathrm{Re}(a_v + b_v)$ where a_v and b_v are the Mie coefficient expressed in terms of Ricatti-Bessel functions and propagation constant $k = \frac{2\pi}{\lambda}$.

The scattering and absorption cross-section of the metal nanoparticles are given as

$$C_{scat} = \frac{1}{6\pi}k^4|\alpha|^2 \text{ and } C_{abs} = k\,\mathrm{Im}g[\alpha]$$

The extinction cross-section will be

$$C_{ext} = C_{scat} + C_{abs} = \frac{1}{6\pi}k^4|\alpha|^2 + k\,\mathrm{Im}g[\alpha]$$

Using the equation 1.19

$$C_{ext} = \frac{8\pi}{3}k^4a^6\left|\frac{\varepsilon_m - \varepsilon_d}{\varepsilon_m + 2\varepsilon_d}\right|^2 + 4\pi ka^3\,\mathrm{Im}g\left[\frac{\varepsilon_m - \varepsilon_d}{\varepsilon_m + 2\varepsilon_d}\right] \qquad \textbf{1.22}$$

Both scattering and absorption enhances at $\varepsilon_1(\omega)= - 2\varepsilon_d(\omega)$. The proportionality of scattering and absorption with the wavelength and particle sizes can be represented as

$$C_{scat} \propto \frac{a^6}{\lambda^4}; \qquad C_{abs} \propto \frac{a^3}{\lambda}$$

So, for any tiny particles absorption efficiency dominates to the scattering efficiency. Therefore, in quasi-static regime $\lambda >> 2a$ (where a is the radius of nanoparticles) above expression of extinction cross-section of equation 1.22 can concluded as

$$C_{ext}(\omega) = 9\frac{\omega}{c}\varepsilon_d^{3/2}V_0 \frac{\varepsilon_2(\omega)}{[\varepsilon_1(\omega) + \chi\varepsilon_d(\omega)]^2 + \varepsilon_2(\omega)^2} \qquad \textbf{1.23}$$

The Mie theory is limed to the perfect spherical particles for which $\chi=2$, so, equation 1.23 can be written as

$$C_{ext}(\omega) = 9\frac{\omega}{c}\varepsilon_d^{3/2}V_0 \frac{\varepsilon_2(\omega)}{\left[\varepsilon_1(\omega) + 2\varepsilon_d(\omega)\right]^2 + \varepsilon_2(\omega)^2} \qquad \textbf{1.24}$$

Using $\lambda=2\pi c/\omega$, where λ is read out wavelength, the expression of extinction can be written as

$$C_{ext}(\lambda) = \frac{18\pi V_0\varepsilon_d^{3/2}}{\lambda} \frac{\varepsilon_2(\lambda)}{[\varepsilon_1(\lambda) + 2\varepsilon_d(\lambda)]^2 + \varepsilon_2(\lambda)^2} \qquad \textbf{1.25}$$

If N is the number of nanoparticles per unit volume, then extinction coefficient (k_{ext}) is defined as

$$k_{ext}(\lambda) = N \cdot C_{ext}(\lambda)$$

$$k_{ext}(\lambda) = \frac{18\pi N V_0\varepsilon_d^{3/2}}{\lambda} \frac{\varepsilon_2(\lambda)}{[\varepsilon_1(\lambda) + 2\varepsilon_d(\lambda)]^2 + \varepsilon_2(\lambda)^2} \qquad \textbf{1.26}$$

The extinction spectrum $A(\lambda)_{ext}$ (Absorbance in case of small particles) of a colloidal solution containing *N* spherical particles in an optical cell with a path length *L* is given by $A(\lambda)_{ext}=kL/ln10$. Putting $L=1$ and $V_0=(4\pi/3)a^3$, then extinction spectrum will be [17]

$$A(\lambda)_{ext}=\frac{24\pi^2 Na^3\varepsilon_d^{3/2}}{\lambda\ln(10)}\frac{\varepsilon_2(\lambda)}{[\varepsilon_1(\lambda)+\chi\varepsilon_d(\lambda)]^2+\varepsilon_2(\lambda)^2} \qquad \textbf{1.27}$$

where ln10 = 2.303 and χ=2 for spherical particles, then equation 1.27 becomes

$$A(\lambda)_{ext}=\frac{24\pi^2 Na^3\varepsilon_d^{3/2}}{2.303\cdot\lambda}\frac{\varepsilon_2(\lambda)}{[\varepsilon_1(\lambda)+2\varepsilon_d(\lambda)]^2+\varepsilon_2(\lambda)^2} \qquad \textbf{1.28}$$

It is to be noted that in the Mie theory the location of absorption band can be envisioned by *Fröhlich condition,* if $\varepsilon_2(\omega)$ is less dependent on the frequency (ω) of incident light as discussed previously. The bandwidth and intensity peak are also estimated by $\varepsilon_2(\omega)$. The Mie theory treatment is comparatively easy as well as adaptable and renders great insight into the physical phenomenon. But, the formulation of scattering cross-section is valid only for small size spherical metal nanoparticles (2a≤30 nm) in which only primary LSPR band is considered corresponding to the excitation of dipole mode only. For bigger metal particles, full derivation of Mie expression including higher order multiple absorption and scattering is required. It is only applicable for the non-interacting small spherical particles. In the derivation, it is assumed that the dielectric function of the spherical particle and surrounding medium is homogeneous and can be mentioned by the bulk dielectric function. From the extinction, the equation does not accomplish the particle size dependency on the LSPR peak position, while the experimental results show highly dependency on particle size [18]. Moreover, other complicated facts like the incorporation of the effect of inter-band electronic transitions on the optical absorption of metallic nanostructures also not considered in the formulation [19].

1.7 Extension of Mie theory

Particle shape dependency on the LSPR position is incorporated in the extended form of Mie theory. If metal nano-participles are not spherical, then scattering cross-section will be represented by the following equation using Gans Theory (Extension of Mie theory) for both oblate and prolate spheroidal nanoparticles [4], [20]–[22]

$$C_{ext} = 9\frac{\omega}{c}\varepsilon_d^{3/2}V_0\sum_j \frac{\varepsilon_2(\omega)/p_j^2}{[\varepsilon_1(\omega)+\frac{1-p_j}{p_j}\varepsilon_d(\omega)]^2+\varepsilon_2(\omega)^2} \qquad \mathbf{1.29}$$

or in terms of wavelength, equation 1.29 can be written as

$$C_{ext} = \frac{2\pi\varepsilon_d^{3/2}V_0}{3\lambda}\sum_j \frac{\varepsilon_2(\omega)/p_j^2}{[\varepsilon_1(\omega)+\frac{1-p_j}{p_j}\varepsilon_d(\omega)]^2+\varepsilon_2(\omega)^2} \qquad \mathbf{1.30}$$

Where *j* corresponds to the three dimensions of the particles and P_j (P_a, P_b, and P_c) is the added depolarization factor corresponding to three-axis x, y and z of spheroidal nanoparticle. If a, b and c are the geometrical dimension of spheroidal particle in x, y and z geometric axis, then for prolate (a>b=c) or oblate (a<b=c), the geometrical factors P_a, P_b, and P_c are define as

$$p_a = \frac{1-e^2}{e^2}\left[\frac{1}{2e}\ln\left(\frac{1+e}{1-e}\right)-1\right]\ ;\ p_b = p_c = \frac{1-p_a}{2}$$

where e is the eccentricity of the particle having aspect ratio R (ratio R=a/b) of the particle. The eccentricity of the particle is defined as

$$e = \sqrt{1-\left(\frac{b}{a}\right)^2} = \sqrt{1-\frac{1}{R^2}}$$

The anisotropy in the depolarization factor changes the $\varepsilon_1(\omega)$ and $\varepsilon_2(\omega)$ that results in varied LSPR frequency.

1.8 Tuning of LSPR peak position

The peak of LSPR frequency primarily depends on average particle size, the material of particle, surrounding medium, inter-particle spacing, particle number density. Influence of different parameters on the LSPR profile occur due to particle size, shape, material, material coverage area, particle number density substrate material, etc [18]. For non-spherical particles, more than one LSPR peaks are observed. In the case of metallic nano rods two distinct LSPR peaks appear corresponding to the longitudinal (along with the major axis) and the transverse (along with the minor axis) oscillation. The longitudinal and transverse oscillation corresponds to the absorption peaks at higher and lower wavelength position respectively. The difference between LSPR peak position increases with an increase in the aspect ratio of the nano rods. The more complex shape particles exhibit multi-pole plasmon resonance. Longitudinal plasmon resonance as a function of R is calibrated with the following equation

$$\lambda_{\max} = (53.71 \cdot R - 42.29) \cdot \varepsilon_{out} + 495.14 \qquad \textbf{1.31}$$

From equation 1.19, the LSPR frequency ω_{max} depend on the dielectric medium of the surrounding as per the following equation

$$\omega_{\max} = \frac{\omega_p}{\sqrt{1+2n_d^2}} \text{ ; where } \varepsilon_d = n_d^2$$

and replacing frequency with the wavelength via relation $\lambda = 2\pi c/\omega$, then LSPR wavelength λ_{max} can be written as [22]

$$\lambda_{\max} = \lambda_p \sqrt{1 + 2n_d^2} \approx \sqrt{2}\lambda_p n_d \qquad \textbf{1.32}$$

Where λ_p is the wavelength corresponding to the plasma frequency. Equation 1.32 shows that LSPR peak wavelength λ_{max} and refractive index show almost linear relation. If surrounding medium is vacuum (where $n_d = 1$) then equation 1.32 become as

$$\lambda_{\max} = \sqrt{3}\lambda_p$$

The LSPR peak position dependency on the volume fraction (F) using effective medium theory is given by [23]

$$\lambda_{\max} = \lambda_p \sqrt{1 + \left(\frac{2+F}{1-F}\right) n_d^2} \qquad \textbf{1.33}$$

The broadening in LSPR peak mainly depends on the distribution of particle size and particle shapes [24], [25].

1.9 Void plasmon

In previous section we have discussed the LSPR excitation in the isolated metal nanoparticles embedded in a dielectric media. To expand the understanding on LSPR excitation, the dielectric nanovoid in metallic surrounding also found suitable for such excitation. In the formulation of polarizability as shown in equation 1.19, the replacement of dielectric function of metal $\varepsilon_m(\omega)$ by the dielectric function of surrounding dielectric $\varepsilon_d(\omega)$ and vice versa is needed (Figure 1.4). The modified formulation of polarizability can be written as

$$\alpha = 4\pi a^{3}\left[\frac{\varepsilon_{d}-\varepsilon_{m}}{\varepsilon_{d}+2\varepsilon_{m}}\right] \qquad \textbf{1.34}$$

In this case similar to the isolated island the denominator $|2\varepsilon_m(\omega)+\varepsilon_d(\omega)|$ or $|2\varepsilon_1(\omega)+\varepsilon_d|^2+|2\varepsilon_2(\omega)|^2$ should be minimum for LSPR excitation in nanovoid. In this case $\varepsilon_1(\omega)=-\varepsilon_d / 2$ should hold under the *Fröhlich condition* for LSPR resonance [8].

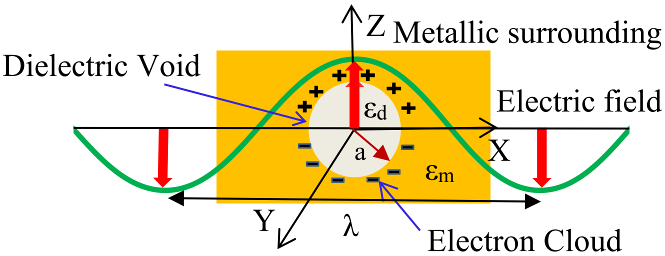

Figure 1.4 A schematic of localized surface plasmon resonance excitation in a dielectric nano-void exist in homogeneous metallic surrounding.

The silica particle coated with the Au is known as the core/shell particle. It is an excellent examples of three-dimensional void plasmon [8],[26]. The two-dimensional voids in the thin films also show the LSPR excitation similar to the three-dimensional nano-void and nanoparticles. Using equation 1.7 we can write as

$$\varepsilon_{1}(\omega) \approx 1-\frac{\omega_{p}^{2}}{\omega_{\max}^{2}} = -\frac{\varepsilon_{d}}{2}$$

$$\omega_{\max} = \omega_{p}\Big/\sqrt{\frac{2+\varepsilon_{d}}{2}}$$

For vacuum surrounding ($\varepsilon_{d}=1$), the above expression become as

$$\omega_{\max} = \sqrt{2}\left(\frac{\omega_{p}}{\sqrt{3}}\right) \qquad \textbf{1.35}$$

From equation 1.21 and equation 1.35 we can conclude that

$$(\omega_{\max})_{void} = \sqrt{2}(\omega_{\max})_{particle} \qquad \textbf{1.36}$$

Equation 1.36 shows that plasmon in void structure will generate at higher energy or lower wavelength in comparison to the nanoparticles of similar size.

1.10 Fabrication techniques for plasmonic structures

In the literature, various techniques are available for the fabrication of nanostructured thin films and periodic structures. As discussed earlier that nanostructured thin films obtained during the early stage of deposition of a continuous thin film or post-deposition annealing of the continuous thin film also results in self-assembled nanostructured thin films [27]. So, all the techniques which are commonly used for the continuous film deposition, can be directly implemented for the fabrication of nanostructured thin films. Thermal evaporation [24], electron beam evaporation, laser ablation [28] and sputtering (both DC and RF sputtering) [29] are the most renowned techniques for the thin film deposition [30]. In the present thesis we have used DC sputtering technique for the fabrication of nanostructured Au thin films. The sizes and shapes of the nanostructures are varied with the sputtering time and sputtering current. It is to be noted that system of interest for the current thesis is nanostructured (island and percolated) thin films. So, the comparison between different thin film deposition techniques regarding smoothness/roughness of surface and interface is out of scope from the present study. Moreover, as disused in section 1.2 that the periodic plasmonic structures have some specific advantages in compression to the random plasmonic nanostructures. Therefore, in the intervening years of evaluation of plasmonic field colossal attention has been devoted to the advancement of fabrication techniques. Among them, nanosphere lithography (NSL), soft nano-imprint lithography, combination of soft and nanosphere lithography, laser pulse interference technique, and electron beam lithography (EBL) are the most famous techniques, which are developed for the integration of periodic structures on the substrate.

In the NSL, drop-coating of mono-layer polystyrene balls is performed to make a self-organized hexagonal closed pack (HCP) mask on the substrate for the physical vapor thin film deposition. The polystyrene ball can later be washout using ultrasonicator in ethanol, which results in triangular metallic structures decorated on the substrate. The thickness of the fabricated thin film can control the height of the patterned triangular metallic elemental. The diameter of the polystyrene spheres controls the side dimensions of triangular and inter-particle spacing. The broad range of metals can be used for deposition to fabricate different metallic structures. However, this technique is limited to the triangular metallic elements in HCP pattern only. A large thickness of the deposited metal films also create a problem in the lift-off process during ultra-sonication. The slip dislocation and missing nanosphere type defects are also common in this lithography technique due to packing imperfections in the polystyrene nanosphere mask [31]. However, the structure produced by deposition of large thickness metal film over the mono-layer polystyrene nano-spheres without performing lift-off step can also be used to produce structures known as a film over nanosphere (FON), which are often used as SERS substrate.

The EBL is known for fabrication of periodic structures of desired sizes, shapes, patterns and inter-structural spacing. Typically, this process involves coating of electron beam sensitive resist (positive or negative) over the conducting film. The electron beam exposes the coated resist in pre-designed pattern. The exposed resist is developed in an appropriate developer depending upon the nature of the resist. After that, deposition of plasmonic metal is carried out on the developed structures followed by the lift-off process, which results in the desired pattern of plasmonic structures. The EBL technique is highly reproducible and vastly used for integrating the arbitrary model of needed nanoscale structures. However, the fabrication area in EBL is limited to 500 μm × 500 μm as well as exposure time also very large (1-4 hour depending upon the feature sizes). EBL is also a time consuming and costly technique. The present EBL technique (SEM assisted EBL) is capable to fabricate the large area (12.5 mm^2) nanoparticle grating structures in very short time (19 s). In the SEM assisted EBL, raster scan of the electron beam exposure is used to fabricate the periodic structure. The depth of the grating structure is varied by changing accelerating voltage (5keV to 30 keV) of electron beam exposure. The periodicity of the nanoparticle gratings can be change by varying the lines per frame at fixed magnification.

1.11 Recent trends, issues, and requirements in the field of plasmonics

Recent advances in the field of plasmonics are both in the basic and applied directions. In the basic direction, A Saedi studied the thermodynamics of deposition flux depended intrinsic stress in growth of plasmonic thin films to obtained a minimum stressed nanostructure system [32]. V Derkach et al worked on the effect of grain boundaries on the nanostructured morphology during solid-state dewetting [33]. K Min et al uses the silk protein as a adhesion layer rather than conventional dielectric material during growth of plasmonic nanostructures to control the morphologies on the base substrate [34]. M Arya et al carried out the observation and calculation of anisotropy in in-plane and out-of-plane plasmonic response of nano-island system [35]. In the applied direction, J Quan et al looked for the establishment of a suitable formulation between dewetting temperature of plasmonic thin film and the SERS intensity [36]. Similar type of plasmonic system is also center of attraction for the solar cell application [37]. The fabrication of porous nanostructure and hyperbolic chiral sculptured metal systems is also used to tune the nano scale morphology and their optical responses for preparation highly sensitive plasmonic sensors [38], [39]. Apart from the mono-metallic system the bimetallic (Ag-Au alloy) plasmonic nanostructured systems are also subject of current interest for the substrate in chemical sensors [40]. In such system, tuning of LSPR response in full UV-visible spectrum is possible by variation in elemental mixture which is exceedingly beneficial to achieve the higher SERS enhancement factor [40], [41]. L X Lu et al fabricated the pattern plasmonic structures using solid-state dewetting on the template substrate and studied the various parametric dependency in details [42]. Q C Tong reported the fast fabrication techniques for the periodic nanostructures of desired plasmonic response using direct laser writing [43]. For advanced applications, E B Urena et al have fabricated plasmonic waveguide-integrated nanowire laser for the future opto-electronic devices [44]. The fabrication process imposes lot of challenges and issues either in thin films or periodic structures based plasmonic architectures.

Most of the thin film deposition techniques used for growth of plasmonic systems (random or periodic) impose a constraint on the particle size and number density for higher deposition time due formation a continuous film which is unable to show any LSPR response [29]. As a consequence, the fabrication of nanostructured metallic thin film having larger size nanoparticles is essential to enlarge the wavelength tuning range of LSPR response [45]. Moreover, obtaining the highly circular particle for sharp LSPR response is also one of the crucial tasks. In this regard the transformation of continuous film into island films can be achieved via the solid-state dewetting process. So, the real-time investigation of dewetting process of the thin film is required using high-speed imaging with a sub-nanometer resolution for in-depth understandings of the process. Z. M. Qi et al. reported that plasmonic response of deposited ultra-thin films shows instability even at the room temperature against aging, which indicates that associated morphology and other physical parameters might be unstable at room temperature due to the existence of natural solid state-dewetting [46]–[48]. Therefore, as-deposited nanostructures are not suitable for the technological applications [49]. The proper quantification of phenomenon along with in-depth understating is a need for the practical use of the nanostructured thin films for short as well as long time. The LSPR peak position and its broadening are intimately correlated with the efficiency of the plasmonic devices specially for SERS enhancement [50]. The variation in the particle sizes, shapes, and inter-particle spacing in thin films change the number density of hot spots (higher intensity region), which results in alteration of SERS enhancement ratio [51], [52]. Apart from various nanostructured thin films, a direct method for large area fabrication of metallic periodic structures in a very short time is also required for plasmonic applications [53].

1.12 Motivation of the thesis

In view of above issues like as-deposited nanostructured thin films are not suitable for the technological applications due to instability in plasmonic response. A wide range of particle size is a needed for tunability of the plasmonic response, where narrow size distribution is the primary requirement to get a sharp LSPR profile. But most of the techniques are not able to produce large size discrete nanoparticles due to the formation of percolated or continuous films. For this purpose, we noted that, it is beneficial to explore well known Au nanostructured thin films. But, the study on the fabrication of nanostructured thin films and their solid state-dewetting process is limited to ex-situ analysis that do not provide enough information about the involved mechanism [54], [55]. Moreover, in-situ analysis of the dewetting process has not been examined in the adequate details [56], [57]. The Au nanostructured thin film shows instability in its plasmonic response on aging in ecological condition despite its chemical inert nature [47]. Except few reports, the uncertainty in the plasmonic response of as-deposited nanostructured thin films is mostly unexplored [46], [48]. Along with the intense on-going investigations on random plasmonic nanostructure, the research on the fabrication of periodic structures are prompted due to particular advantageous applications. Some of the underlying periodic structures are employed and are currently working well for nanophotonics as well as chemical and bio-sensors. A single element act as serving element in molecule-detection sensors and energy transport nanophotonics systems. The quest of finding a suitable fabrication techniques as well as a substrate to overcome the limitation of large area fabrication of plasmonic periodic structures in short time is very much required. The existing literature motivated us to fabricate and characterize the plasmonic properties of nanostructured thin films and periodic structures in detail for useful applications. The present work is taken up with the following objectives:

1. Investigation of growth mechanism and solid-state dewetting dynamics in nanostructured Au thin films using ex-situ and in-situ transmission electron microscopy.
2. Investigation of the instability in the LSPR response of the nanostructured Au thin films against aging at ambient temperature.

3. Selection of direct method for the fabrication of large area plasmonic nanoparticle periodic structures in short time for SERS applications.
4. Usefulness of plasmonic nanoparticle grating structures for tunability of optical diffraction efficiency.

1.13 Outline of the thesis

In this chapter (**Chapter-1**), historical evolution of the field along with some breakthroughs, basics of plasmonics, the current status of the research, issues, requirement, and motivation behind the present study have been discussed. **Chapter-2** deals with the sample preparation and characterization techniques e.g., sputtering, scanning electron microscopy (SEM), transmission electron microscopy (TEM), atomic force microscopy (AFM), X-ray reflectivity (XRR), X-ray diffraction (XRD), grazing incidence X-ray diffraction (GIXRD), energy dispersive spectroscopy (EDS), absorption spectroscopy, and Raman spectroscopy, which are employed for morphological, elemental, crystallographical and optical characterizations. In **Chapter-3,** exploitation of growth and dewetting mechanisms using in-situ and ex-situ TEM imaging techniques is described. The effect of process parameters on the evolution of morphological parameters during growth process has been analyzed using ex-situ TEM imaging techniques. The detailed study of dewetting dynamics during post-deposition annealing is performed by real-time monitoring of morphological transformations using in-situ TEM imaging. A clear-cut correlation between sputtering time, sputtering current, annealing temperature and annealing time with the film thickness, Feret diameter, circularity, number density and covered area fraction has been demonstrated. In **Chapter-4,** the strong evidence of large instability in the characteristics LSPR response (blue-shift in peak position) of nanostructured Au films against ambient aging has been discussed. The experimental identification of morphological reorganization and crystallization on ambient aging presents the testimony for the basic phenomenon behind the instability in LSPR response. The natural solid-state dewetting during room temperature aging is found as the reason behind the changes in nanostructured morphologies. For clear demonstration of the phenomenon, the information about the effect of process parameters (sputtering time and sputtering current) on the plasmonic response of Au thin film is provided. Monitoring of the absorbance of nanostructured thin films at various stage of aging is performed. A dynamical model for correlation between plasmonic response and natural solid-state dewetting is established. Finally these aged Au films are also subjected to SERS substrate. In **Chapter-5**, a direct method for fabrication of large area plasmonic nanoparticle grating structures (PNG) in very short time has been demonstrated using conventional SEM on silver halide (AgBr) based film. The application of fabricated PNG structures has been demonstrated as a preferable SERS substrate. The PNG grating provided an enhancement in the SERS intensity by two orders of magnitude in comparison to the sputtered deposited nanoparticle film. Additional three-time enhancement in the SERS signal with a reduction in the grating period is also achieved.The enhancement in SERS signal is due to generation of large number of hot spots in the integrated PNG structures. **Chapter-6**, deals with the variation in the depth and shape of the plasmonic nanoparticles grating structures with change in the accelerating voltage of exposing electron beam. This chapter also provides the tuning range of optical diffraction efficiency with change in accelerating voltages. In **Chapter-7**, a summary of the present thesis work is provided with future scope for possible extension of research on plasmonic nanostructured thin films and periodic structures.

References:

[1] M. Faraday, “The Bakerian lecture: Experimental relations of gold (and other metals) to light,” *Philos. Trans. R. Soc. London*, vol. 147, no. 0, pp. 145–181, 1857.

[2] J. C. M. Garnett, “Colours in metal glasses and in metallic films rapid response,” *Philos. Trans. R. Soc. A*, no. 203, pp. 385–420, 1904.

[3] C. Worsch, M. Kracker, W. Wisniewski, and C. Rüssel, “Optical properties of self assembled oriented island evolution of ultra-thin gold layers,” *Thin Solid Films*, vol. 520, pp. 4941–4946, 2012.

[4] G. Mie, “Contributions to the optics of turbid media, particularly of colloidalmetal solutions,” *Ann. Phys.*, vol. 25, no. 3, pp. 377–445, 1908.

[5] C. V. Raman and K. S. Krishnan, “Polarisation of scattered light-quanta,” *Nature*, vol. 122, no. 3066. pp. 169–169, 1928.

[6] D. L. Jeanmaire and R. P. Van Duyne, “Surface raman spectroelectrochemistry: Part I. Heterocyclic, aromatic, and aliphatic amines adsorbed on the anodized silver electrode,” *J. Electroanal. Chem.*, vol. 84, no. 1, pp. 1–20, 1977.

[7] T. W. Ebbesen *et al.*, “Extraordinary optical transmission through sub-wavelength hole arrays,” *Nature*, vol. 86, no. 6, pp. 1114–7, 1998.

[8] S. A. Maier, *Plasmonics: Fundamentals and applications*. New York: Springer, 2007.

[9] Mark L. Brongersma Pieter G. Kik, *Surface plasmon nanophotonics*. Netherlands: Springer, 2007.

[10] K. A. Willets and R. P. Van Duyne, “Localized surface plasmon resonance spectroscopy and sensing,” *Annu. Rev. Phys. Chem.*, vol. 58, no. 4:35, pp. 267–97, 2007.

[11] J. Zhang and L. Zhang, “Nanostructures for surface plasmons,” *Adv. Opt. Photonics*, vol. 4, pp. 157–321, 2012.

[12] C. Kittel, *Introduction to solid state physics*, 18th ed. New Delhi: Wiley India, 2014.

[13] U. Kreibig and M. Vollmer, *Optical properties of metal clusters*. Berlin: Springer, 1995.

[14] E. Hutter and J. H. Fendler, “Exploitation of localized surface plasmon resonance,” *Adv. Mater.*, vol. 16, no. 19, pp. 1685–1706, 2004.

[15] Heinz Raether, *Surface plasmons on smooth and rough surfaces and on gratings*. Verlag: Springer, 1986.

[16] J. D. Jackson, *Classical Electrodynamics*. New York: Wiley, 1999.

[17] E. Petryayeva and U. J. Krull, “Localized surface plasmon resonance:

Nanostructures, bioassays and biosensing-A review," *Anal. Chim. Acta*, vol. 706, pp. 8–24, 2011.

[18] K. L. Kelly, E. Coronado, L. L. Zhao, and G. C. Schatz, "The optical properties of metal nanoparticles: The influence of size, shape, and dielectric environment," *J. Phys. Chem. B*, vol. 107, no. 668–677, 2003.

[19] A. Pinchuk, G. Von Plessen, and U. Kreibig, "Influence of interband electronic transitions on the optical absorption in metallic nanoparticles," *J. Phys. D. Appl. Phys.*, vol. 37, pp. 3133–3139, 2004.

[20] S. Link and M. A. El-Sayed, "Spectral properties and relaxation dynamics of surface plasmon electronic oscillations in gold and silver nanodots and nanorods," *J. Phys. Chem. B*, vol. 103, pp. 8410–8426, 1999.

[21] S. Link and M. A. El-Sayed, "Simulation of the optical absorption spectra of gold nanorods as a function of their aspect ratio and the effect of the medium dielectric constant," *J. Phys. Chem. B*, vol. 109, no. 20, pp. 10531–10532, 2005.

[22] Y. Hong, Y. M. Huh, D. S. Yoon, and J. Yang, "Nanobiosensors based on localized surface plasmon resonance for biomarker detection," *J. Nanomater.*, vol. 759830, pp. 1–13, 2012.

[23] V. N. Rai, A. K. Srivastava, C. Mukherjee, and S. K. Deb, "Surface enhanced absorption and transmission from dye coated gold nanoparticles in thin films," *Appl. Opt.*, vol. 51, no. 14, pp. 2606–2615, 2012.

[24] D. Gaspar *et al.*, "Influence of the layer thickness in plasmonic gold nanoparticles produced by thermal evaporation," *Sci. Rep.*, vol. 3:1469, pp. 1–5, 2013.

[25] C. L. H. and R. P. Van Duyne, "Nanosphere lithography: A versatile nanofabrication tool for studies of size-dependent nanoparticle optics," *J. Phys. Chem. B*, vol. 105, no. 24, pp. 5599–5611, 2001.

[26] R. M. Cole, J. J. Baumberg, F. J. De Garcia Abajo, S. Mahajan, M. Abdelsalam, and P. N. Bartlett, "Understanding plasmons in nanoscale voids," *Nano Lett.*, vol. 7, no. 7, pp. 2094–2100, 2007.

[27] C. V. Thompson, "Solid-state dewetting of thin films," *Annu. Rev. Mater. Res.*, vol. 42, pp. 399–434, 2012.

[28] S. Verma *et al.*, "Surface plasmon resonances of Ag-Au alloy nanoparticle films grown by sequential pulsed laser deposition at different compositions and temperatures," *J. Appl. Phys.*, vol. 117, no. 133105, pp. 1–11, 2015.

[29] S. Horikoshi, N. Matsumoto, Y. Omata, and T. Kato, "Growth of Au nanoparticle films and the effect of nanoparticle shape on plasmon peak wavelength," *J. Appl. Phys.*, vol. 115, no. 193506, pp. 1–8, 2014.

[30] J E Mahan, *Physical Vapor Deposition of Thin films*. New York: John Wiley & Sons, 1999.

[31] T. R. Jensen, M. L. Duval, K. L. Kelly, A. A. Lazarides, G. C. Schatz, and R. P. Van Duyne, “Nanosphere lithography: effect of the external dielectric medium on the surface plasmon resonance spectrum of a periodic array of silver nanoparticles,” *J. Phys. Chem. B*, vol. 103, no. 45, pp. 9846–9853, 1999.

[32] A. Saedi and M. J. Rost, “Thermodynamics of deposition flux-dependent intrinsic film stress,” *Nat. Commun.*, vol. 7:10733, pp. 1–6, 2016.

[33] V. Derkach, A. Novick-Cohen, and E. Rabkin, “Grain boundaries effects on hole morphology and growth during solid state dewetting of thin films,” *Scr. Mater.*, vol. 134, pp. 115–118, 2017.

[34] K. Min, M. Umar, S. Ryu, S. Lee, and S. Kim, “Silk protein as a new optically transparent adhesion layer for an ultra-smooth sub- 10nm gold layer,” *Nanotechnology*, vol. 28, no. 115201, pp. 1–8, 2017.

[35] M. Arya, M. Ranjan, M. Bhatnagar, R. Nath, and A. Mitra, “In-plane and out-of-plane plasmons in random silver nanoisland films,” *Plasmonics*, 2017.

[36] J. Quan, J. Zhang, X. Qi, J. Li, N. Wang, and Y. Zhu, “A study on the correlation between the dewetting temperature of Ag film and SERS intensity,” *Sci. Rep.*, vol. 7:14771, pp. 1–12, 2017.

[37] Z. Duan, M. Li, T. Mwenya, Y. Li, and D. Song, “Morphology optimization of silver nanoparticles used to improve the light absorption in thin-film silicon solar cells,” *Plasmonics*, 2017.

[38] A. Kosinova *et al.*, “Tuning the nanoscale morphology and optical properties of porous gold nanoparticles by surface passivation and annealing,” *Acta Mater.*, vol. 127, pp. 108–116, 2017.

[39] F. Abbas, M. Faryad, and Y. Yb Bi Er, “A highly sensitive multiplasmonic sensor using hyperbolic chiral sculptured thin films Defec,” *J. Appl. Phys.*, vol. 122, no. 173104, pp. 1–7, 2017.

[40] S. Verma *et al.*, “Optical and surface enhanced Raman scattering responses of densely packed Ag-Au alloy nanoparticle films of varied composition and thickness,” *J. Alloys Compd.*, vol. 753, pp. 395–706, 2018.

[41] Y. Oh, J. Lee, and M. Lee, “Fabrication of Ag-Au bimetallic nanoparticles by laser-induced dewetting of bilayer films,” *Appl. Surf. Sci.*, vol. 434, pp. 1293–1299, 2018.

[42] L.-X. Lu, Y.-M. Wang, B. M. Srinivasan, M. Asbahi, J. K. W. Yang, and Y.-W. Zhang, “Nanostructure formation by controlled dewetting on patterned substrates: A combined theoretical, modeling and experimental study,” *Sci. Rep.*, vol. 6:32398, pp. 1–18, 2016.

[43] Q. Cong Tong, M. Hoang Luong, J. Remmel, M. DO Thanh, D. Thuy Trang Nguyen, and N. Diep Lai, “Rapid direct laser writing of desired plasmonic nanostructures,” *Opt. Lett.*, vol. 42, no. 12, pp. 2382–2385, 2018.

[44] E. Bermúdez-Ureña *et al.*, “Plasmonic waveguide-integrated nanowire laser,”

Nano Lett., vol. 17, pp. 747–754, 2017.

[45] L. Yan, Y. Yan, L. Xu, R. Ma, F. Jiang, and X. Xu, “Large range localized surface plasmon resonance of Ag nanoparticles films dependent of surface morphology,” *Appl. Surf. Sci.*, vol. 367, pp. 563–568, 2016.

[46] Z. M. Qi, S. Xia, and H. Zou, “Slow spontaneous transformation of the morphology of ultrathin gold films characterized by localized surface plasmon resonance spectroscopy,” *Nanotechnology*, vol. 20, no. 255702, pp. 1–5, 2009.

[47] C. Garozzo, A. Filetti, C. Bongiorno, A. La Magna, F. Simone, and R. A. Puglisi, “Room temperature evolution of gold nanodots deposited on silicon,” *Gold Bull.*, vol. 47, pp. 185–193, 2014.

[48] H. Hieber, “Aging properties of gold layers with different adhesion layers,” *Thin Solid Films*, vol. 37, pp. 335–343, 1976.

[49] T. Kawaguchi and S. Maruno, “Change in optical transmission spectra of Ag discontinuous films due to aging,” *Jpn. J. Appl. Phys*, vol. 35, no. 10, pp. 5485–5486, 1996.

[50] M. Kahraman, P. Daggumati, O. Kurtulus, E. Seker, and S. Wachsmann-Hogiu, “Fabrication and characterization of flexible and tunable plasmonic nanostructures,” *Sci. Rep.*, vol. 3:3396, pp. 1–9, 2013.

[51] P. Pavaskar, I. K. Hsu, J. Theiss, W. H. Hung, and S. B. Cronin, “A microscopic study of strongly plasmonic Au and Ag island thin films,” vol. 113, no. 34302, pp. 1–6, 2013.

[52] K. Grochowska, K. Siuzdak, J. Karczewski, M. Szkoda, and G. Śliwiński, “Properties of thermally dewetted thin Au films on ITO-coated glass for biosensing applications,” *Plasmonics*, vol. 12, no. 6, pp. 1939–1946, 2017.

[53] Y. Lee, K. Koh, H. Na, K. Kim, J. J. Kang, and J. Kim, “Lithography-free fabrication of large area subwavelength antireflection structures using thermally dewetted Pt/Pd alloy etch mask,” *Nanoscale Res. Lett.*, vol. 4, pp. 364–370, 2009.

[54] I. Beszeda, I. A. Szabó, and E. G. Gontier-Moya, “Morphological evolution of thin gold films studied by Auger electron spectroscopy in beading conditions,” *Appl. Phys. A*, vol. 78, pp. 1079–1084, 2004.

[55] A. Reznickova, Z. Novotna, N. S. Kasalkova, and V. Svorcik, “Gold nanoparticles deposited on glass: Physicochemical characterization and cytocompatibility,” *Nanoscale Res. Lett.*, vol. 8:252, pp. 1–8, 2013.

[56] C. M. Müller and R. Spolenak, “Microstructure evolution during dewetting in thin Au films,” *Acta Mater.*, vol. 58, pp. 6035–6045, 2010.

[57] F. Niekiel, P. Schweizer, S. M. Kraschewski, B. Butz, and E. Spiecker, “The process of solid-state dewetting of Au thin films studied by in situ scanning transmission electron microscopy,” *Acta Mater.*, vol. 90, pp. 118–132, 2015.

Chapter 2

Experimental Techniques

2.1 Introduction

This chapter presents, the fabrication and characterization techniques of nano-structured silver (Ag) and gold (Au) thin films as well as plasmonic nano-particle grating (PNG) structures. The deposition of Ag and Au thin films on different substrates is carried out using sputtering technique. The fabrication of PNG structures is carried out using conventional scanning electron microscope (SEM). An understanding of the basic principle of SEM enhances its usage as the PNG fabrication tool. For morphological characterization light microscope (LM), SEM, field emission electron microscope (FESEM), atomic force microscope (AFM), conventional transmission electron microscope (TEM) and x-ray reflectivity (XRR) techniques are used rigorously. TEM has been extensively used for in-situ imaging of Au thin films for post-deposition annealing studies. The elemental and crystallographic information of Au thin films, silver halide (AgBr) based film, and PNG structures are obtained by energy dispersive spectroscopy (EDS), x-ray diffraction (XRD), grazing incidence x-ray diffraction (GIXRD) and selected area electron diffraction (SAED) techniques. The optical absorption of both Au thin films and PNG structures are recorded by UV-Vis spectro-photometer. The potential application of fabricated PNG structures is successfully demonstrated using surface-enhanced Raman spectroscopy (SERS) as well as diffraction efficiency measurements.

2.2 Fabrication of plasmonic thin films and grating structures

2.2.1 Substrates for thin film deposition

The float glass and formvar coated copper (Cu) grid (FCF300-Cu Electron Microscopy Sciences) are used as substrates for deposition of nanostructured Au thin films. The glass substrate are thoroughly cleaned before Au film deposition, while the formvar films are used as received from the merchant. The cleaning of glass is carried out in the ultrasonic bath for about 20 min each in soap solution, deionized water and acetone in sequence. Care has been taken so that neither of the surfaces of the substrate come in touch with the beaker surface during the ultrasonic process. The substrates remain in vertical standing position on one of its cross-section surface at the bottom of the beaker. This precaution avoids the unwanted scratches on the substrates. Finally, substrates are baked at 180 °C for half an hour. The dimensions of float glass was about 25 mm × 25 mm × 1.3 mm (length × width × thickness). The formvar film was supported by ~3.05 mm diameter Cu grid, and the dimensions of a single square mesh of Cu was 58 µm × 58 µm. The formvar film is transparent to the electron beam and is frequently used for morphological imaging of nano-structured films deposited upon it.

2.2.2 Sputtering system

The deposition of nanostructured Au thin films is performed by Peltier cooled direct current (DC) magnetron sputter coater (EMITECH 575 X). It is a compact table-top dedicated thin film coating unit which is generally used to coat the metallic or carbon thin film for SEM or TEM samples. In the sputtering process when high energy particles strike the targets, then material atoms are ejected by momentum transfer phenomenon and plasma of target material is formed that is deposits as a thin film on the substrate.

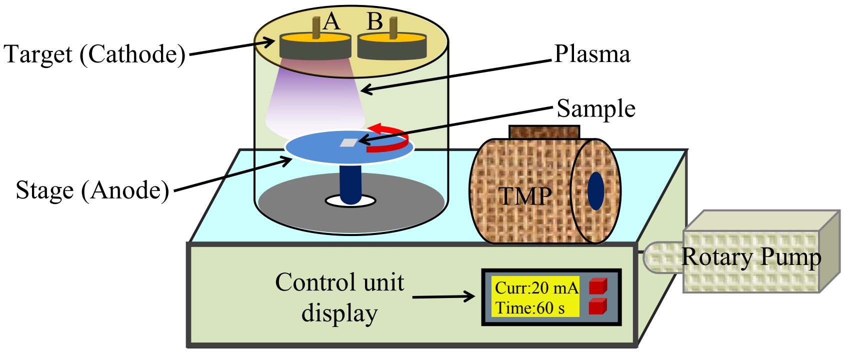

Figure 2.1 Schematic of sputter coater system showing glass chamber constituting two target holder and one rotating stage, turbo molecular pump, rotary pump, and control unit display.

Figure 2.1 shows the schematic of DC magnetron sputtering setup. The two target holders, A and B, and one sample stage are enclosed in a glass chamber. The diameter of each target holder is ~5.7 cm and that of the stage is ~10 cm. During deposition, sample stage rotates with 6 cycles per minute (fixed). The distance between target holder and sample stage is ~3.5 cm (fixed). The high purity Au target (99.99 % pure) (Quorum TECHNOLOGIES) of 57 mm diameter × 2 mm thickness is used for film deposition. The potential applied to the target holder (cathode), and the sample stage (anode) is ~3 keV (fixed). The glass chamber is directly connected to the turbo molecular pump (TMP), backed by a rotary pump. The TMP is used to create a high vacuum in the chamber to minimize the impurities. Before each deposition, base vacuum in the chamber was achieved up to $\sim 3\times10^{-4}$ mbar. After that, Ar gas is purged to initiate the sputtering process, which leads to a reduction in vacuum level to $\sim 1\times10^{-2}$ mbar. The deposition is carried out on float glass samples and formvar films

(TEM grids) simultaneously. The temperature of the substrate was room temperature. The sputtering current and sputtering time are the two variable parameters, which are used to deposit different thickness nanostructured Au films. Two sets of thin films having different thicknesses have been prepared at different deposition rates. The depositions are carried out for 5, 10, 15, 20, 30, 45, and 60 s at 10 mA current in set-A and 10, 15, 20, 30, 40, 45, 50, 60, 80, and 120 s at 20 mA current in set-B. Four Ag nanoparticle films are also grown on the bare PET substrate by sputtering the Ag target for 60, 120, 180, and 240 s at 50 mA current. For each film, deposition is done in subsequent way except 60 s sample. In subsequent method, sputtering process is stopped after every 1 min deposition time for ~5 min exposure of ambient environment by breaking the vacuum of the chamber.

2.2.3 Conventional scanning electron microscope (SEM)

The fabrication and imaging of PNG structures are performed by tungsten filament based conventional SEM (Philips XL 30 CP). This system provides morphological imaging along with elemental spectra, and mapping. The Philips XL 30 CP SEM offers magnification in the range of 20× to 100000× and spatial resolution up to 3.5 nm at 30 keV for morphological imaging in SE mode. The spatial resolution of elemental mapping for the material is less compared to morphological imaging. The specimen stage has a movement of ~50 mm in the X, Y and Z directions with a tilt of -15° to +70° and 360 ° rotation.

SEM consists of a high energy accelerated electron beam falling on the sample surface in a raster fashion. When a focused high energy beam of electrons scans the specimen the striking primary electrons (PE) loose a significant amount of kinetic energy due to various elastic and inelastic scattering with specimen atoms [1]. This leads to the formation of a distinct teardrop-shaped volume that is the electron beam-specimen interaction volume. This intersection of PE electrons results in the generation of secondary electrons (SE), back-scattered electrons (BSE), Auger electrons (AE), characteristic x-rays, cathode-luminescence (CL), Bremsstrahlung, plasmon scattering and heat. In the morphological imaging, which is the primary imaging mode in SEM, detector picks up the SE's during the raster scanning of PE's. The signal is subsequently amplified and converted into an electrical signal that modulates the intensity on the display and this modulation of intensity leads to the image formation approximately simultaneously. Elemental analysis is carried out either by energy dispersive (EDS) or wavelength dispersive spectroscopy (WDS) technique. It provides elemental spectra and elemental mapping along with elemental quantification using characteristic x-rays of the specimen due to interaction with electron beam. The phase contrast in a multi-phase materials, and their mutual textural relationships can be analysed using back-scattered electrons (BSE) of the sample. There are few other imaging modes also possible such as CL signal with a sub-micron resolution to detect the optical and electronic properties as well as chemical composition of materials.

Figure 2.2 shows the schematic of the SEM. An electron gun, vacuum column, chamber, detector and the visual display unit are the main components of the SEM. The electron gun consists of a hairpin tungsten (W) filament, Wehnelt cup, and high kV potential anode. The thermionic emission of electron from filament is focused into a spot using Wehnelt cup by applying a negative potential to the aperture where as high kV potential anode accelerates it further. In the column, electromagnetic condenser lens (L_1 and L_2) and objective lens (L_3) is used to focus the electron beam at the substrate. The deflection coils are used for scanning the focused electron beam on

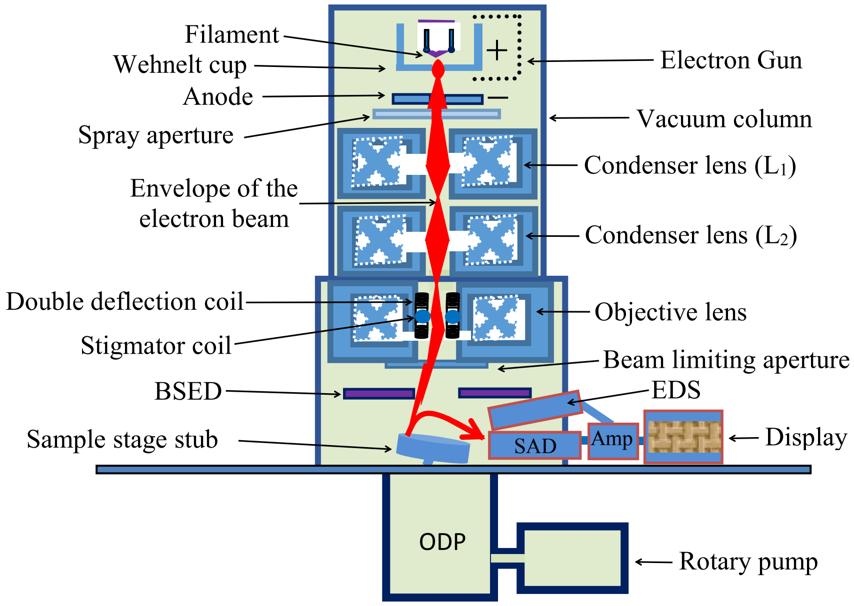

Figure 2.2 Schematic of conventional scanning electron microscope (SEM) instrument, showing the electron gun, electron column, specimen chamber, SED Detector, EDS detector, BSED detector, vacuum pumps and visual display screen.

the specimen surface. The specimen chamber is connected to the vacuum (oil diffusion pump and rotary pump) and detection units. Finally, the detection unit is connected to the visual display screen. The typical path of the electrons is shown by red color in the Figure 2.2. For proper cooling of the magnetic lenses, a cooling unit (Chiller) is also equipped with SEM. Moreover, for appropriate imaging, the system is on a vibration free isolation table.

The magnification (M) of the SEM is defined as the ratio of area of display screen (A_2) to that scanned upon the specimen (A_1). It can be written as

$$M = A_2 / A_1$$

Here the size of the display screen remains fixed and hence magnification depends entirely upon area scanned on the sample. Lower the scanning area of the specimen higher will be the magnification.The scanning area on the substrate can be varied from 4 mm by 4 mm for lower magnifications to lesser than 200 nm by 200 nm for highest magnifications.

The spatial resolution of SEM for morphological imaging mainly depends on the spot size of the focused electron beam as well as on the electron beam specimen interaction volume. The dependence of spot size on the machine part is on source size (tungsten pin), the strength of converging lenses, alignment optics of the electron beam and wavelength of the electron at a particular energy. The electron beam specimen interaction volume depends on the energy of the primary electron as well as on the specimen material. To fabricate the PNG structures same conventional SEM is used. In the modified EBL technique, raster scanning of the electron beam (484 lines per frame) is used to exposed the electron beam sensitive AgBr film at 20× magnification to produce the 10 μm period nanoparticle grating structures. As described above, the magnification decides the exposure area on the substrate which is about 12.5 mm^2 at 20× magnification. The lowest magnification (20×) gives the highest fabrication area. The grating period can be reduces as 5 μm, 3.4 μm, and 2.5 μm by increasing the number of lines per frame as 968, 1452, and 1936 at the same magnification (20×) respectively. The exposure time required to 10 μm, 5 μm, 3.4 μm, and 2.5 μm period grating was as 19 s, 38 s, 57 s, and 76 s. The depth of the grating structures is controlled by variation in accelerating voltages of electron beam exposure. In this technique eighteen gratings of same and different period can be fabricated in a single process. For that purpose a aluminum substrate holder having size of 40 mm by 40 mm is designed, which offers a 40 mm by 20 mm exposure area for the fabrication of the grating structures. The detailed discussion on the fabrication of PNG structure can be find in the chapter-5.

The FESEM (Carl Zeiss-Auriga) is used for high-resolution imaging of the cross-section of the unprocessed AgBr based microscopic film and the Ag grains embedded in the fabricated PNG structures. The FESEM also used to acquire high-resolution images of nanostructured Ag films deposited on the bare PET substrate and nanostructured Au films grown on glass and Si substrates. The working principle of FESEM is similar to the SEM except the electron gun and motorized specimen stage.

2.3 Light microscope (LM)

The initial characterization of all the fabricated nanoparticle grating structures is carried out using the light microscopes (LM) (Leica DMC 2900) in transmission as well as reflection mode. In the present studies, the transmission mode is used for the imaging as the base material PET is transparent to the light. This system provides 5× to 2000× magnification. The maximum view area on the specimen of the system is ~5 mm in diameter.

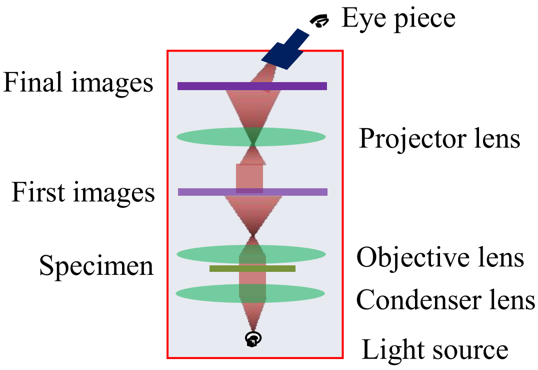

Figure 2.3 Schematic of light microscope (LM) instrument, showing the light source, condenser lens, specimen, objective lens, projector lens and attached eyepiece.

Figure 2.3 shows the typical schematic of the LM instrument. The light source, a condenser lens, an objective lens, projector lens, and eyepiece are the main components of the standard LM. The specimen is kept on the transparent glass slide, which is attached to the stage which can move in x, y, and z-direction.

2.4 Conventional transmission electron microscope

The morphological imaging and electron diffraction pattern of as-grown nano-structured poly-crystalline Au thin films deposited on formvar film is carried out by tungsten filament based conventional transmission electron microscope (TEM) (Philips CM 200) as shown in Figure 2.4. The bright field (BF), dark field (DF), high resolution TEM (HRTEM) and selected area diffraction (SAED) modes are available. The magnification ranges from 20× to 1000000× to yield a 2.4 Å point resolution and 1.4 Å line resolution in BF imaging mode. The maximum specimen tilt angle of specimen holder is −40° to +40° polar angle and −20° to +20° azimuthal angle for various type of specimen holders. A microheater (Philips) attached with single tilt specimen holder can be used for in-situ annealing up to 1000° C with a constant

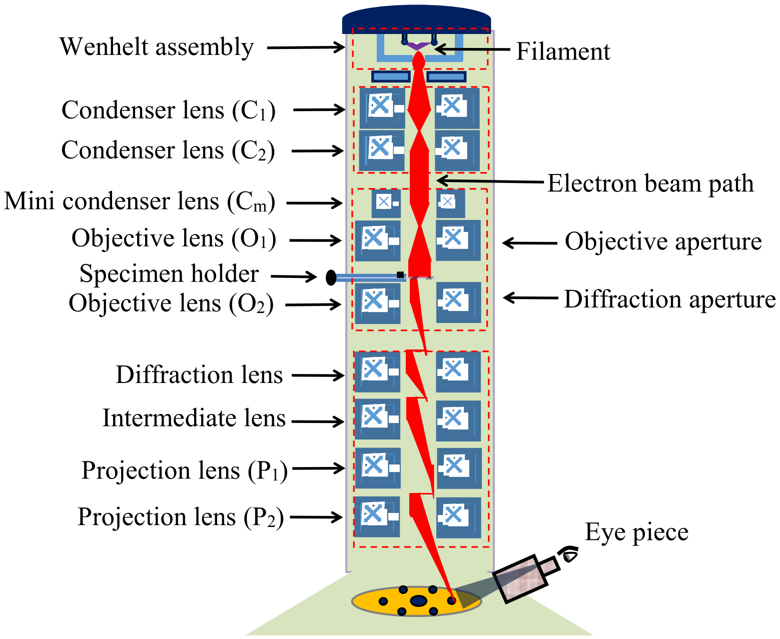

Figure 2.4 Schematic of conventional transmission electron microscope (TEM) instrument, showing the electron gun, electron column, condenser and objective lens assembly, diffraction lens, intermediate and projector lens assembly, fluorescent visual screen and attached eyepiece.

heating ramp of 100° C min^{-1}. The fundamental principle of TEM is similar to the LM. In TEM, the collimated mono-energetic electron beam passes through the thin specimen and then the transmitted and scattered electrons carry the information about the sample. These electrons are further used to produces an image on a charged-coupled device (CCD) (Gatan Ultra scan 1000) using various electromagnetic lenses. The scattering, diffraction and phase contrast are used to form image. If images are created using the intensity variation of transmitted beam, then it is called bright field imaging, and if the only scattered electrons are used, then it is called dark field imaging. At the same time, diffracted electrons are used to form diffraction patterns as well as high resolution imaging.

Figure 2.4 shows the typical schematic of TEM. The electron gun, condenser lenses, a mini condenser lens, objective lenses, diffraction lenses, intermediate lenses, projector lenses, a fluorescent screen, CCD camera, and eyepiece are the main components of TEM. Similar to the SEM, W/ LaB_6 based filament is used for thermionic emission of electrons in TEM. The first crossover (virtual beam spot size) of accelerated electrons is in between the high keV anode and Wehnelt cup as shown in the travel path of the electron beam in the column (red color envelope). This virtual spot is formed at the front focal plane of condenser lens assembly (C_1 and C_2), which finally produces a parallel beam of electrons. The construction of condenser lenses is such that there is a better control on the illumination with a control on parameters like the variation in spot size and illumination intensity. Mainly, C_1 lens is used to vary the beam spot size, and C_2 lens is used for the focus/defocus purpose. The electron beam can be focused at the front focal plane of the objective lens assembly using another mini condenser lens placed after the C_2 lens. Depending upon the application, the combination of the mini condenser lens and objective lens assembly can be used for either focused or parallel illumination on the specimen. This also leads to a flexibility of switching between spot and conventional mode. The objective lens assembly is responsible for producing the first intermediate image of the sample. The image resolution and contrast are also associated with the objective lens assembly. The intermediate image formed at the image plane or the so called selected area plane is further magnified by projector lens assembly (P_1 and P_2) and is finally seen on the fluorescent screen. The fluorescent screen is placed at the bottom of the TEM, on which images of the specimen are directly visible. This can be further magnified optically using a combination of small fluorescent screen and a 10× eyepiece. The electron diffraction pattern formed at the back focal plane of the objective lens assembly can also be imaged at the same fluorescent screen and is discussed in the following section in detail. The frame size of 25 mm × 35 mm having a 1024 × 1024 pixel screen in the CCD for capturing the images. The integration time can vary from 1 to 30 s however in the present case it was 2 s. Moreover, high voltage power supply, vacuum pumps, compressor and chillier, etc. are required. Analysis of the TEM images and the electron diffraction patterns was performed using ImageJ freeware. Images were made binary by adjusting the lower and the upper-level color threshold to calculate the particle size, circularity (sphericity), number density, covered area fraction (CAF) and the inter-particle spacing.

The total magnification of TEM is defined as the product of the magnifications of objective and projector lens assembly. The magnification of objective lens can be changed by varying the strength using current flowing in the objective lens. However, variation in the current of objective electromagnetic lenses is avoided because it can lead to a temperature variation in the sample. Therefore in the TEM, the objective plane, image plane and viewing screen are kept fixed and parallel beam produced by the objective and condenser lens assembly illuminates the sample. After that a portion of first intermediate image formed at image plane is selected using selected area aperture. Further higher magnification is achieved using intermediate and projector imaging lens assembly. In this case image plane of the objective lens assembly is the object plane for the intermediate and projector imaging lens assembly. Intermediate and projector imaging lens assembly can have the back focal plane of the objective lens assembly as its object, by reducing the current in intermediate lenses. Thus magnified diffraction pattern can also be simultaneously imaged at the viewing screen.

In the electron diffraction, a regular pattern of spots, concentric rings and diffused distribution around the central spot are formed for crystalline, polycrystalline and non-crystalline specimens respectively. Here, the distances between the regular spots or diameters of the concentric rings are directly related to the d spacing of the crystalline or polycrystalline sample respectively. Figure 2.5 shows the typical diffraction pattern of a crystalline specimen. The L, R, d, and λ are the camera length, distance from central spot or radius, lattice spacing and wavelength associated with

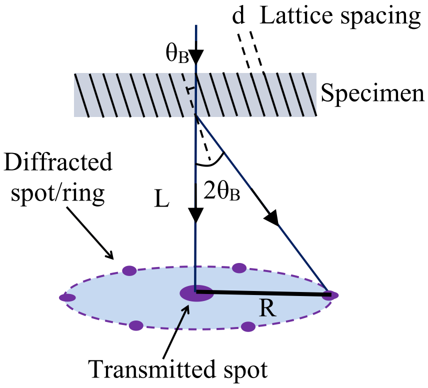

$R = L \tan 2\theta_B$
$2d\sin\theta_B = \lambda$
$Rd = L\lambda$
L and λ are fixed

Figure 2.5 Schematic of electron Bragg diffraction pattern from a specimen on visual screen and relation between camera length (L), diffracted spot or ring radius (R), specimen lattice spacing (d) and incident electron wavelength (λ) for conventional transmission electron microscope (C) instrument.

the electron beam of TEM respectively. The equation Rd= Lλ, holds for Bragg diffraction condition. Similar to XRD a concentric ring shape pattern will be formed in the case of electron diffraction from a poly-crystalline Au thin film. Here L and λ are constant for a given machine for a given accelerating voltage and hence for different d spacing different distances / radii of spot / ring of the crystalline//non-crystalline specimen will appear. The diffraction pattern from CCD is measured using a nm^{-1} unit scale bar in which inverse of R is equal to the d spacing of specimen. The R can be calculated from the diffraction pattern using different spots that exist in crystalline or poly-crystalline diffraction pattern. For a cubic system using $d = \frac{a}{\sqrt{h^2 + k^2 + l^2}}$ lattice parameter 'a' can be easily obtained for a particular (h,k,l) plane of Au thin film.

2.5 Atomic force microscope (AFM)

The LM had a large field of view but the resolution is diffraction limited to ~200 nm. For better resolution, SEM and FESEM are used that are also limited to 2-dimensional morphological imaging [2]. Additionally, electron microscopy requires sample in vacuum and an additional conducting coating of metal/carbon on the insulating specimens to overcome the charging effect as described in prior sections. TEM is used for specific transmission geometry applications. Hence, to obtain 3-dimensional images of nanostructured Au thin films and PNG structures in environmental conditions, AFM (Agilent technology 5420) is used. This technique provides ~5-10 nm lateral and ~0.1 nm spatial vertical resolution. The scanning area for Agilent technology 5420 setups ranges from 100 nm × 100 nm to 90 μm × 90 μm. The vertical dimension (height) of ~8 μm in the specimen morphology can also be imaged.

The line scan profile can also be obtained from the recorded images to quantify and to better represent the features present in the specimen. This same system also enables to do many other types of microscopic analysis like magnetic force microscopy (MFM), Kelvin force microscopy (KFM), electric force microscopy (EFM), and piezo force microscopy (PFM).

It is a tip probe technique, generally called scanning probe microscopy (SPM), in which a sharp tip scans the substrate in either contact or non-contact mode [2]. The Van der Waals force between the specimen and the tip guide the tip movement which is finally used to constructed a 3-dimensional image of the specimen. Figure 2.6 shows a schematic of typical AFM system. The laser, photo-diode detector, piezo-controlled x-y scanner, cantilever connected with z-piezo, sharp tip mounted with the free end of the cantilever and sample stage are main components of the AFM system. The probe tip (Si_3N_4 or Si) scans the substrate line by line (raster scan) controlled by the x-y scanner. The z-piezo system also controls the z movement of cantilever tip. During scanning, a laser light beam falls on the top surface of the cantilever and reflects towards a position sensitive photodiode detector. The various available modes of the AFM technique are mainly categorized into two types

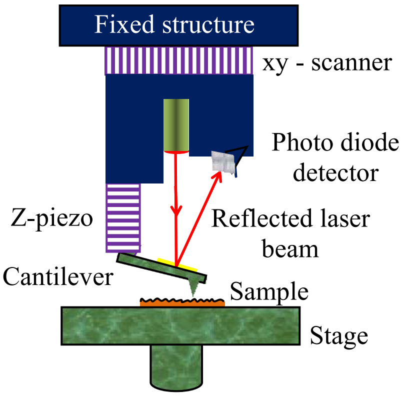

Figure 2.6 Schematic of AFM instrument showing laser, laser diode detector, piezo-controlled x-y scanner, probe tip attached to cantilever specimen, z-piezo, and sample stage.

depending upon the basis of recording cantilever deflection. In first, static deflection of the AFM cantilever is recorded and in the second dynamic deflection of the tip is recorded. Both contact and oscillating modes are the frequently used modes of the AFM technique. In contact scanning mode deformation in cantilever is adjusted by the detector and feedback electronics implementing the variation in the vertical direction with the z-piezo attached with the cantilever. The z-piezo feedback is recorded at each point of x-y coordinate, which is finally used to build up a map of 3-dimensional morphology. In dynamic mode, cantilever oscillates with a particular frequency and amplitude, under the constant force between tip and substrate. On the basis of amplitude and phase of oscillation of the cantilever during scanning, the modes are named as tapping and non-contact mode. The variation in amplitude and phase of the oscillating cantilever is finally used to build morphological images of the specimen.The resolution of AFM microscopy mainly depends on the scanning tip size (radius of curvature). The tip of 2-10 nm radius of curvature is commercially available.

2.6 X-ray reflectivity (XRR)

Physical properties such as average film thickness, material density, surface or interface roughness of as-grown and aged Au thin films can be determined by hard x-ray reflectivity (XRR) technique. This technique is employed on laboratory based x-ray source (BRUKER D8 system). The wavelength used for the measurement was 1.541 Å (Cu-K_{α}, 8.047 keV). The XRR is regarded as a non-contact and non-destructive technique with sub-nanometer resolution for characterization of all types of thin films and multilayers effectively up to about 1000 nm thickness. When a monochromatic x-ray wave falls on an ideal flat surface at a grazing incident (θ_i) then

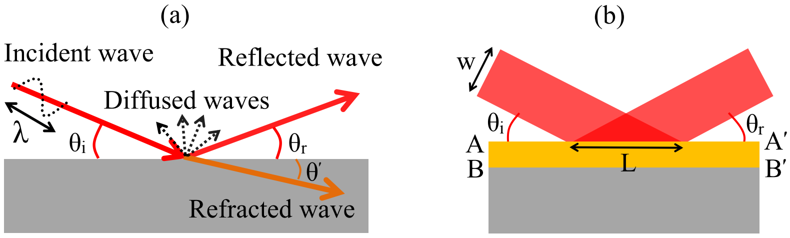

Figure 2.7 (a) Representative schematic of specular reflection, diffused reflection and the refracted wave on the ideal flat surface material surface, (b) schematic of footprint length (L) spread over the film surface for a ‘w’ width x-ray beam.

specular reflection, diffused reflection, and refraction occur as shown in the Figure 2.7 (a) [3]. The refractive index of all the materials for x-rays is less than one. Therefore total external reflection occurs for an incident angle less than the critical angle (θ_c). In the case of a thin film deposited on the ideal flat surface, interference will occur between specularly reflected wave received from the top surface of the thin film (AA′) and interface (BB′) (Figure. 2.7(b)). Due to the interference of the specularly reflected waves, oscillation appears in the reflectivity pattern. These oscillations are called Kiessig fringes. The width of Kiessig oscillations, the amplitude of oscillation, and the decay rate of reflected intensity pattern depend upon the film thickness, electron density contrast between the substrate and the deposited film along with roughness of the top surface and the interface respectively. The XRR technique is highly sensitive to film parameters and therefore a well collimated and low divergence x-ray beam along with precise instrumental alignment are needed before the measurement. It is essential that the sample size should be larger than the footprint (marked in Figure 2.7 (b)) of the beam. For a typical slit width ‘w’ and a grazing incident angle, ‘θ’ footprint (L) of x-ray beam on the sample can be calculated from the a following formulation

$$L = \frac{W}{\sin\theta_i} \qquad \textbf{2.1}$$

The lateral width of the slit should also be less than the sample size. In the present study metal slits having 50 and 100 μm vertical width and 10 mm lateral width is used. The projection length for 0.2° grazing incidence angle is calculated as ~14.3 mm for 50 μm slit width. As described in section 2.1 that sample surface area for glass is more than the 20 mm by 20 mm. Moreover, no significant variation is observed in the normalized reflectivity pattern measured with both 50 and 100 μm slit width. The reflectivity data is acquired with respect to 2θ for all the samples. But normalized spectra of both as-deposited and aged (4 months) is plotted individually and compared in the momentum unit (q_z), rather than in 2θ unit for all the samples. The momentum (q_z) is defined as

$$q_z = \frac{4\pi\sin\theta}{\lambda} \qquad \textbf{2.2}$$

The analysis of the reflectivity data is done by fitting with Parratt recursive formalism (Parrot 32 model 1.6) and thickness, roughness, critical angle and electron density profile have been obtained for all the Au thin films. The critical angle (θ_c) is calculated by the following relation

$$\theta_c = \sqrt{2\delta} \qquad \textbf{2.3}$$

where δ is the real part of the complex refractive index of the material $n=1-\delta + i\beta$. In the fitting, some typical values of the thickness, roughness and the electron density are introduced initially in the model of an independent layer of Au thin film and finally allow the software to converge to more accurate values in the iterative processes for minimum χ value.

2.7 X-ray diffraction (XRD)

The XRD is a well-established non-destructive tool to study the various types of single crystal, poly-crystals, and amorphous materials. Crystalline information of fabricated Ag nano-particle gratings, AgBr based film, and sputter grown Au thin films are determined by XRD and grazing incidence x-ray diffraction (GIXRD). These measurements were performed at beam lines BL-11 and BL-12 (Extreme condition XRD and Angle Dispersive XRD) at the Indus-2 synchrotron radiation source, India. The XRD pattern is used to calculate the average Ag grain size present in the fabricated PNG structures. The GIXRD is used to probe the re-crystallization process that has occurred in sputter grown Au thin films in due course of aging.

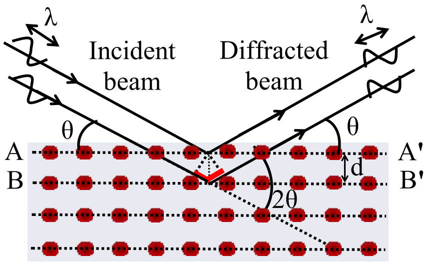

Figure 2.8 Schematic of Bragg diffraction from a typical d spacing lattice plane of the crystal.

Figure 2.8 shows a typical schematic of the XRD phenomenon. When an x-ray beam (monochromatic and parallel) of wavelength λ is incident on a crystal at an angle θ is reflected from all the adjacent planes at angle 2θ (from the incident direction). If the reflected x-ray waves received from adjacent plans are in phase or out of phase, then constructive or destructive interference occurs respectively and this phenomenon is called Bragg's diffraction [4]. If data is recorded as a function of diffracted intensity with angle 2θ then for a polycrystalline sample, a series of peaks will appear at different angles in the spectra corresponding to a specific d spacing of the crystal planes. For constructive interference, path difference can be given by the following equation [5]

$$2d\sin\theta = n\lambda \qquad \textbf{2.4}$$

where d is the spacing between adjacent planes and n is an integer. Equation 2.4 is known as Bragg’s equation. Equation 2.4 shows that Bragg peaks at lower 2θ corresponds to higher d spacing, and Bragg peaks at higher angle 2θ will appear corresponding to lower d spacing crystal planes. In the case of single crystal, sharp spots will appear in the diffraction pattern corresponding to each diffracting plane for a given wavelength λ. For polycrystalline samples, concentric rings will appear corresponding to specific plane spacing d. As mentioned above so far, the Bragg's equations assumes that crystals are perfect and infinite. Moreover, the incident beam is perfectly parallel and monochromatic, but real experimental conditions are very much different, which leads to broadening in the XRD peaks. These are non-mono-chromaticity of the source, imperfect focusing, finite crystal size, strain, stacking fault and other defects. The average grain size (L) is determined by Scherrer formula for polycrystalline samples as

$$L = \frac{0.96\lambda}{\beta\cos\theta_B} \qquad \textbf{2.5}$$

where β and θ_B are the full width at half maxima (FWHM) of peak at Bragg's angle respectively.

The XRD spectra from the Ag nano-particle gratings are obtained by scratching the particles from the PET substrate and sandwiched between the polyamide sheets (kapton sheets). A 5 mm holed double-sided tape is used for holding the sandwiched structure (Figure 5.13 of chapter-5). Such arrangement helps in avoiding the interruption in the XRD spectra coming from the base material PET. The XRD spectra of Ag nano-particle gratings with PET is also recorded, but due to the large thickness of PET, some of the peaks of Ag do not appear and it is also complicated to analyze the XRD spectra. The polyamide sheet is considered as transparent for the 0.8282 Å (~16keV) x-rays. In this type of sample, Ag nano-particles are embedded in the gelatin matrix with a random orientation. The diffraction pattern was obtained in transmission mode using images plate area detector (MAR 345). The wavelength and the sample to detector distance were accurately calibrated using LaB_6 NIST standard. The XRD spectra of AgBr film is also recorded at 0.6689 Å (18 keV) in transmission using image plate area detector. For Au films, grown on the glass substrate, the GIXRD mode is used due to lower thickness of Au thin films as well as to overcome the effect of higher glass thicknesses. In the GIXRD mode, the interaction volume of x-rays with Au thin film increases. The recorded spectra were used to investigate the variation in the full width at half maxima (FWHM) of polycrystalline nano-structured Au thin films. The measurement for the as-deposited and aged Au thin film was performed at different x-ray energies (~15 keV and 15.5 keV). Therefore, to neglect the effect of energy difference in the peak positions of the GIXRD spectra, the recorded data is plotted in the momentum unit (q_z), similar to the XRR. The wavelength used for GIXRD measurements were accurately determined by using XRD peaks of crystalline Si NIST standards, in the same experimental setup.

2.8 Transmission and absorption UV-Vis spectroscopy

The absorbance spectra of Au thin films and PNG structures were recorded in transmission mode on UV-Vis spectrophotometer (VARIAN-CARY CONC. 50) and Jasco V-670 UV-VIS- NIR spectrophotometer in the range from 300 to 1000 nm with ~2 nm resolution with a clean glass or PET as a reference sample. The transmission is measured from the ratio of transmitted (I) and incident (I_0) intensity. The transmittance (%T) (measured quantity) is defined as [6]

$$\%T = \left(\frac{I}{I_0}\right) \times 100 \qquad \textbf{2.6}$$

The absorbance (A) is the derived from transmittance and defined as

$$A = \log_{10}\left(\frac{100}{\%T}\right) = \log_{10} 10^2 - \log_{10}(\%T) = 2 - \log_{10}(\%T) \qquad \textbf{2.7}$$

2.9 Surface-enhanced Raman spectroscopy (SERS)

The Ag nano-structured thin films grown by sputtering and PNG structures fabricated by the SEM are used as a SERS substrate. The Raman spectra for Rodamine6G (R6G) drop coated on Ag thin films and PNG structure is recorded by the Raman spectrometer (Andor Shamrock SR-303i) equipped with the CW multimode diode laser (CL-2000, CrystaLaser). The operating wavelength (λ_{Ext}) was 785 nm with a maximum output power of 100 mW. The laser power reaching on the sample was ~20 mW within the focal spot of ~100 µm. The Raman spectra were acquired for a duration of 1 s, in the wave number ranging from 500 to 1800 cm^{-1} having the resolution of 5 cm^{-1}. During measurement, the intensity of scattered light verses energy difference is recorded in the unit of cm^{-1}. The instrumental details are given in reference 7. The measured raw Raman spectra of the samples were background subtracted using the range-independent background subtraction algorithm [7], processed using a conventional methodology [8] , and normalized with respect to its mean intensity over a spectral range of 500 cm^{-1} to 1800 cm^{-1}. The nanostructured Au thin films deposited on the glass also used as a SERS substrate for drop coated R6G dye. For these samples, Raman spectroscopy is performed at 514.5 nm excitation wavelength (Ar^+ laser) using Acton 2500i monochromator with CCD detector (WiTec) in back scattering geometry. The data is acquired for 60 s in the wave number ranging from 500 cm^{-1} to 1800 cm^{-1}.

2.10 Diffraction efficiency (DE) measurement set-up

The DE measurements of the fabricated gratings were carried out in the wavelength range from 350-800 nm on a custom-made experimental setup as shown in Figure 2.9 [9]. The experimental setup consists of a quartz tungsten halogen lamp (100 W) coupled with a 1/3 m monochromator, collimating lens, two apertures and a Si detector. A beam steering device consisting of mirrors M_1 and M_2 was modified for holding the grating samples in a horizontal position (parallel to the ground) between the mirrors. An opening (A_1) with a circular hole (3 mm diameter) in the center of the metal sheet was mechanically attached to the mounting rod of the beam steering device. A light beam emerging from the monochromator slit is collimated by a lens L_1. It further passes through a filter used to block the second order intensity coming out

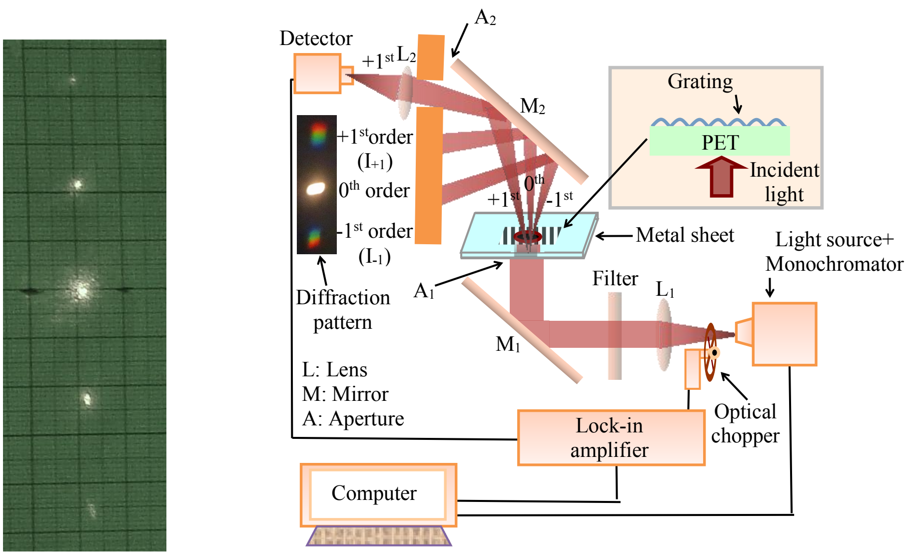

Figure 2.9 Schematic diagram of the experimental setup for the measurement of diffraction efficiency and the photograph of multiple order diffraction pattern obtained using a laser light.

from the monochromator. Mirror (M_1) reflects the light towards the aperture A_1, where the grating sample is placed in the horizontal position on the top of the hole A_1. The size of the light beam reduces to 3 mm after passing through the opening A_1, where as normally it falls on the 4 mm diameter area of the grating substrate. The orientation of the grating sample was kept such that the normal incident light first passes through the air-PET interface then transmits towards PET-grating interface to form a diffraction pattern towards grating-air interface side as seen in the inset of Figure. 2.9. All the diffracted orders of light (0^{th} order, $+1^{st}$ order (I_{+1}) and -1^{st} order (I_{-1}) etc.) are reflected with the help of mirror (M_2) on the second aperture (A_2). The aperture A_2 selects only first order (I_{+1}) of the diffracted light, which is finally focused onto a Silicon photo-diode using the lens (L_2). Furthermore, a phase sensitive detection scheme was implemented with the help of SRS 830 Lock-in amplifier and a mechanical chopper for signal processing, which ensured a high signal-to-noise ratio. In this scheme, all the lenses are made of quartz, which is transparent in the wavelength range of interest. Nevertheless, the absorption of all the optical components other than the grating under this study is considered by acquiring an intensity correction scan. For this scan, the plasmonic grating is replaced by a PET substrate in Figure. 2.9. The obtained signal under this configuration (un-diffracted beam of 3 mm diameter) is taken as incident/incoming intensity (I_0). The first order DE of the plasmonic grating is estimated by recording a scan with the actual grating in place as shown in Figure. 2.9. The magnitude of $+1^{st}$ order signal (I_{+1}) is divided by incoming intensity (I_0) to estimate the values of DE for the plasmonic grating in 350 to 800 nm range.

References:

[1] P. J. Goodhew, J. Humphreys, and R. Beanland, *Electron microscopy and analysis*, 3rd ed. London and New York: Taylor & Francis, 2000.

[2] K. S. Birdi, *Scanning probe microscopes: Applications in science and technology*. Boca Raton: CR Press, Taylor & Francis Group, 2003.

[3] L. G. Parratt, “Surface studies of solids by total reflection of x-rays,” *Phys. Rev.*, 1954.

[4] N. W. Ashcroft and N. D. Mermin, *Solid State Physics*. 2011.

[5] B. D. Cullity, *Elements of x-ray difraction*. Massachusetts: Company, Addison-Wesley Publishing, 1956.

[6] M. Fox, *Optical properties of solids*. Oxford University Press, 2001.

[7] H. Krishna, S. K. Majumder, and P. K. Gupta, “Range-independent background subtraction algorithm for recovery of Raman spectra of biological tissue,” *J. Raman Spectrosc.*, vol. 43, pp. 1884–1894, 2012.

[8] H. Krishna, S. K. Majumder, P. Chaturvedi, M. Sidramesh, and P. K. Gupta, “In vivo Raman spectroscopy for detection of oral neoplasia: A pilot clinical study,” *J. Biophotonics*, vol. 7, pp. 690–702, 2014.

[9] Sudheer *et al.*, “Fabrication of large area plasmonic nanoparticle grating structure on silver halide based transmission electron microscope film and its application as a surface enhanced Raman spectroscopy substrate,” *J. Appl. Phys.*, vol. 118, no. 64303, pp. 1–9, 2015.

Chapter 3

Growth and characterization of sputtered grown ultra-thin gold films

3.1 Introduction

The polycrystalline metallic films are of huge interest due to their extensive involvement in the field of catalysis [1], [2], magnetic memory [3], solar cell [4] and optical response based chemical, biological and gas sensors [5], [6]. The ultra-thin metal films of different morphologies (island, percolated and continuous) are frequently used to improve the sensitivity of surface-enhanced Raman spectroscopy (SERS) [7], [8] as well as for standardization of the color of a physical object in transmission and reflection mode [9]. The efficiency of catalysis and sensor are elevated by island or percolated films in comparison to continuous thin film because of high surface to volume ratio of nanostructures as well as due to the excitation of localized surface plasmon resonance (LSPR) [10]. Among different metals, gold (Au) is used to fabricate such ultra-thin films for most of the applications for long-term applicability because of its minimal tarnishing potentiality. Thermal annealing-induced morphological transformation of ultra-thin polycrystalline Au films is being used to construct an optical response based irreversible temperature sensors [11], [12].

The optical response of Au films is strongly erogenous to its real space parameters (RSP's) like the sizes, shapes, number density of the nanoparticles and the covered area fractions (CAF) in the films along with its surrounding and the substrate material [13], [14]. The average values, as well as the statistical distributions of all the RSP's of the films are crucial, which ultimately determine the optical response of Au thin films [15]. The fine calibration of optical response essentially demands the precisely controlled growth technique along with sub-nanometer scale morphological characterization [16], [17]. Variety of physical deposition techniques are used for the fabrication of nanostructured Au thin films as described in chapter 1. Among these, sputtering is widely employed for controlled morphological growth of the metals thin film [18]. But, similar to other techniques, sputtering also imposes a constraint on the size and number density of the particles because of the formation of a semicontinuous or continuous film for longer deposition time that upshot in a broad or no LSPR response. The evaluation of such semicontinuous or continuous thin films into random island films is achievable by post-deposition thermal annealing [19], [20]. However, the study of the growth mechanism of thin metal films and its morphological evolution during post-deposition annealing is important to produce the nanoparticles of apposite sizes and shapes from different thickness films for efficient LSPR and sensor applications. Usually x-ray diffraction [21], electrical probing [22], auger electron spectroscopy [23] and transmission electron microscopy (TEM) [12] are used to characterize the embroiled processes during the post-deposition annealing of the thin metal films. Most of the above techniques provide limited understanding about the growth mechanism, morphological reorganization, and crystallization kinetics during the post-deposition annealing of thin films because of geometrical modeling based appraisal of RSP's from the large series of measurement data. The

TEM has been found as a simple, efficient and accurate method for such type of investigations in real-time because of ultra-fast recording and sub-nanometer resolution imaging. The formvar film is found economical and optically transparent substrate for metal film deposition during such experiments, which can be instantly used for in-situ TEM study. Many experiments have been performed to study the morphological growth mechanism of Au thin films as a result of thermal dewetting at high temperature but for a short time annealing [12], [24]. However, the study of in-situ annealing of films for a longer time using a TEM technique is required for an better understanding of the thermal dewetting mechanism. In this chapter, growth and dewetting behavior of nanostructured Au thin films deposited on formvar film substrate have been demonstrated using TEM. The deposition of Au thin films is carried out by a sputtering technique, as described in chapter-2. Two sets of Au thin films samples of different thickness are prepared on formvar and glass substrates. In set-A, deposition is carried out at 10 mA sputtering current for 5, 10, 15, 20, 30, 45 and 60 s time. In set-B, the deposition is carried out at 20 mA sputtering current for 10, 15, 20, 30, 40, 45, 50, 60, 80, 120 s time. In this chapter, Au thin films deposited on formvar film of both set-A and set-B are used to study the growth and dewetting behaviour. In chapter-4, Au thin films deposited on glass (both set-A and set-B) will be used to study the aging effect on its optical, morphological and crystallographic properties in environmental ambiance. The morphology of prepared Au thin films is imaged using TEM at room temperature to study the growth. For dewetting process, in-situ imaging of the Au thin films (set-A) during post-deposition annealing was accomplish in a single tilt heating holder (PHILIPS) from 150°C to 500°C with a constant heating ramp of ~100°C min^{-1}. Isothermal annealing at 150°C is carried out for an island type (20 s sample) and just percolated (30 s sample) ultra-thin films.

Isothermal annealing at 250°C followed by subsequent high temperature (350°C, 500°C) is applied to percolated ultra-thin films. The annealing time ranges from 5 min to 6 hours, which was definite at the start of the heating cycle. The electron diffraction patterns of the film were also recorded during the annealing process. The particle size, circularity (sphericity), number density, CAF and the inter-particle spacing are calculated using ImageJ software as delineated in chapter-2. For set-A, the x-ray reflectivity (XRR) measurements were performed on an Au film deposited on the glass substrate (deposited simultaneously with TEM grid) for 60 s only to ascertain the thickness and roughness. The thickness and roughness of 60 s sample are obtained as ~8.4 nm and ~1.3 nm by fitting the experimental XRR data using Parratt recursive formalism [25]. However, the determination of thickness for 5 s to 45 s samples by XRR technique is arduous due to the absence of Kiessing oscillations in the spectra as a consequence of high roughness. Therefore, calculation of average mass-thickness for 5 s to 45 s deposited samples is done by scaling with deposition time [26]. In order to determine the thickness of Au thin films of set-B, x-ray reflectivity is performed on all Au thin films deposited on glass (deposited simultaneously with TEM grid) and calculation of thickness is obtained by carrying out individual fitting of each recorded XRR data of set-B.

3.2 Morphological characterization of as-deposited Au film (set-A)

The average mass-thicknesses of as-deposited films of set-A have been obtained as 0.7, 1.4, 2.8, 4.2, 6.3, and 8.4 nm corresponding to 5, 10, 20, 30, 45, and 60 s sputtering time respectively. Figures 3.1(a)-3.1(f) show the planar view of TEM images (recorded at room temperature) of as-deposited ultra-thin Au films of 0.7, 1.4, 2.8, 4.2, 6.3, and 8.4 nm thickness (set-A). Different morphologies are observed in

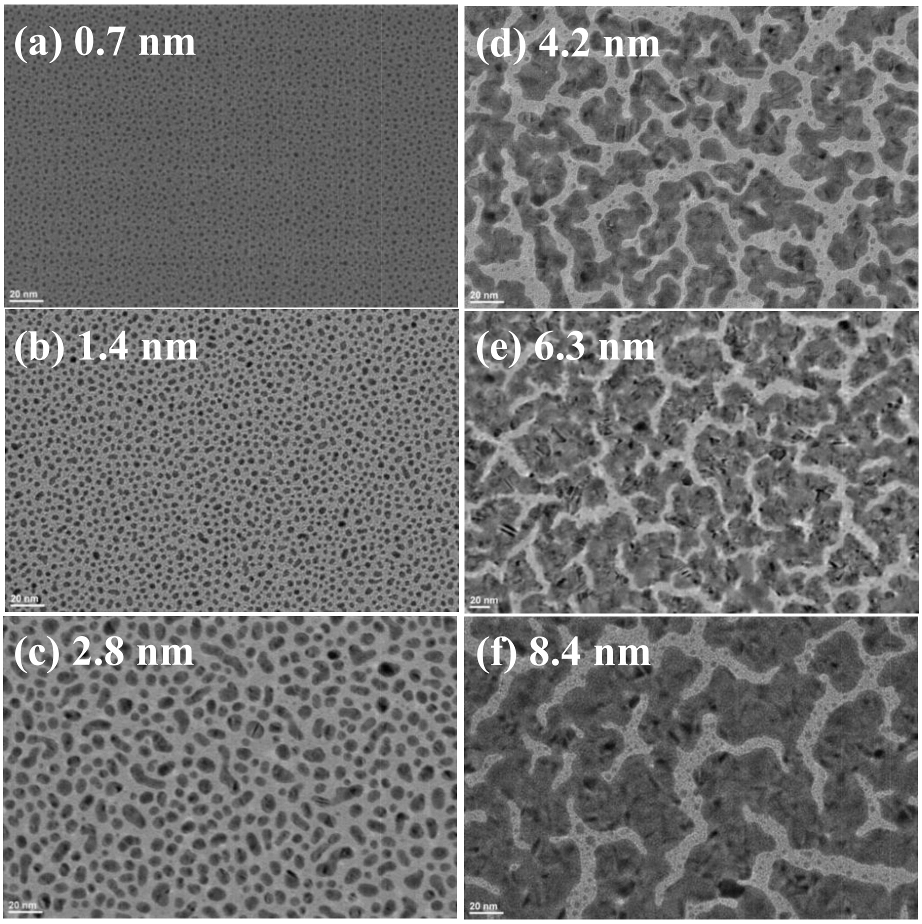

Figure 3.1 TEM images of Au thin films of (a) 0.7 nm, (b) 1.4 nm, (c) 2.8 nm, (d) 4.2 nm, (e) 6.3 nm and (f) 8.4 nm thickness (set-A).

the TEM images for different film thicknesses. It has been observed that for 0.7 nm and 1.4 nm thicknesses, films are having discrete Au nanoparticles of nearly circular (spherical) shapes, whereas for 2.8 nm film thickness, the nanoparticles are in elongated shapes. In the case of 4.2 nm and 8.4 nm thickness semicontinuous films are formed. The quantitative statistical analysis of the images is performed in order to find the average values of various RSP's of the films such as particle size (d), standard deviation in size (σ), circularity (c), number density (n), CAF (percentage filling factor of the Au film F%) and inter-particle gap (g), which is given in Table-3.1. The size (Feret diameter) and circularity of the particles are defined as $d=P/\pi$,

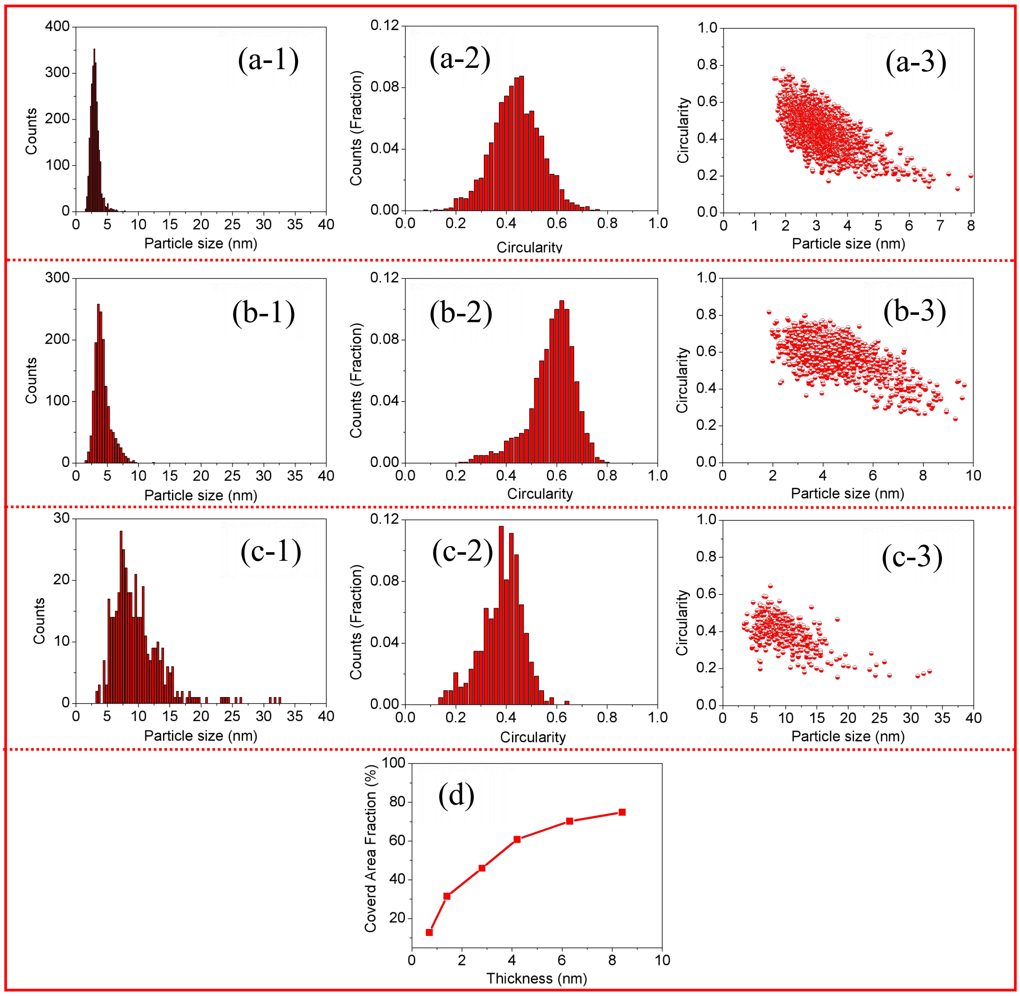

Figure 3.2 Particle size distribution (histograms), circularity distribution and variation in circularity with particle size for (a-1)-(a-3) 0.7 nm, (b-1)-(b-3) 1.4 nm and (c-1)-(c-3) 2.8 nm thickness Au films (set-A). (d) The plot of covered area fraction v/s film thickness of as-grown Au thin films (set-A). All the plots are obtained from Figure 3.1 using ImageJ software.

and c=4πA/(P)^2 respectively. Here P and A are the perimeter and area of the particles, whereas other parameters have their usual meaning. Detailed analysis of RSP's is presented in Figure 3.2, which shows the behaviour of growth as well as a correlation in their statistical distribution. The film of 0.7 nm thickness (Figure 3.1(a)) has uniformly distributed island-like structures (nanoparticles) having ~3.1 nm ±0.7 nm average particle size with the average circularity of 0.45 and the particle number density of 5.7×10^4 particle/μm^2 (Table-3.1). Figure 3.2(a-1) shows a narrower and symmetric distribution of particle size centered at ~3.1 nm for the film having 0.7 nm thickness. Figure 3.2(a-3) shows that circularity of the particles goes down with an increase in the particle size. However, majority of the particles are having high circularity. As the thickness of the films increases from 0.7 nm to 1.4 nm, each arriving atom takes part in the growth of individual islands that results in an enlargement of the particle size and circularity up to ~4.5 nm ±1.3 nm and 0.59 respectively (Figure 3.1(b), Figures 3.2(b-1)-3.2(b-2), Table-3.1). At the same time, the number density reduces to ~3.4×10^4 particle/μm^2. The histogram shows that particle size distribution remains narrower (Figure 3.2(b-1)) along with little asymmetric nature towards higher particle sizes. Here, similar to the above case circularity decreases with a further increase in the particle size (Figure 3.2(b-3)). Such type of Au nanoparticles (sizes <5 nm) are critical to catalyzing the various oxidation and reduction reactions as well as for diameter-controlled growth of single-walled carbon nanotubes [27]–[31]. When the Au film thickness increases from 1.4

TABLE 3.1: Variation in average particle size (d), standard deviation in particle size (σ), circularity (c), number density (n), covered area fraction (F%) and inter-particle gap (g) for as-deposited and annealed Au films of different mass-thicknesses.

Film thickness t (nm)	Average particle size d (nm)	Standard deviation σ (±nm)	Average circularity c	Particle number density n (μm^{-2})	Covered area fraction F%	Inter-particle gap g (nm)
0.7 (As-deposited)	3.1	0.7	0.45	5.7×10^4	17.5	1-3
1.4 (As-deposited)	4.5	1.3	0.59	3.4×10^4	30.3	1.5-4
2.8 (As-deposited)	10	4.1	0.39	9.1×10^3	44.2	0.7-6.5
2.8 (Annealed)(Obtain from Figure 3.3(a-5))	8.7	2	0.77	7.7×10^3	32.7	0.5-8.4
4.2 (Annealed)(Obtain from Figure 3.3(b-5))	17.1	6.9	0.55	2.9×10^3	34	1.3-16

nm to 2.8 nm, the average particle size increases proportionally from 4.5 nm to 10 nm and the standard deviation in particle size also increases significantly. Such drastic changes in the standard deviation of particle size are due to the formation of dumb-bell like or elongated nanoparticles with aspect ratio varies from ~1.6-3.5 (Figure 3.1(c)). The formation of larger aggregates are due to the partial coalescence of some of the nearest neighbour particles. The partial coalescence stage of the growth has also been observed with drastic decrement in the circularity (Figure 3.2(c-2)) as well as in the number density of the particles to 0.39 and 9.1×10^3 particle/μm^2 respectively (Table-3.1). In this case, the particle size distribution becomes broad and significantly asymmetric around average particle size, where some of the elongated nanoparticles are found having sizes ~25 nm and ~32 nm (Figure 3.2(c-1)). It is important to note that during the initial growth process most of the nanoparticles have circular (spherical) shape, which got elongated as the film thickness increases. However, sphericity of the nanoparticles first increases and then start deteriorating with increase in the film thickness (Figures 3.2(a-2), 3.2(b-2), and 3.2(c-2), Table-3.1). Moreover, each of the island film shows similar decreasing nature in circularity with an increase in the particle size, which indicates that at different growth stage larger size particles hold relatively higher asymmetry in shape (Figures 3.2(a-3), 3.2(b-3), and 3.2(c-3)). In the present growth process, the film thickness of 2.8 nm is found to be the optimum for which largest discrete nanoparticles are formed with a negligible percolation. In this case, the ratio of average nanoparticle size and inter-particle spacing is also found to be maximum (Table-3.1), which is an excellent situation for inter-particle near-field coupling in discrete nanoparticles through spatial confinement of electrons and photons for sub-wavelength waveguide and focusing applications [32].

The percolation in the films is started from the thickness of ~4.2 nm, where ginger like shapes (cross-linked network) are formed with lateral growth of nanostructures as shown in Figure 3.1(d). This indicates that the threshold value for the island-to-percolation transition of growth lies at ~4 nm of thickness. However, in the case of thickness ≥4.2 nm, other parameters of the films like particle size, circularity, and the number density are difficult to define because of irregular and partially connected morphology of the nanostructures. These partially connected films are useful for creation of plasmonic hot spots (areas of the enhanced electric field in the film), which are frequently used in SERS for higher enhancement factor in the scattering to detect Raman active chemical species having either lower concentration or lower amount [33]. Further increase in the film thickness from 4.2 nm to 6.3 nm, a complex structure having crack-like voids (semicontinuous film) is formed in the film having ~3-15 nm lateral voids width (Figure 3.1(e)). Some of these voids are filled in the case of 8.4 nm thickness due to a higher degree of percolation (grain coarsening) in the film as a result of an increase in the CAF (Figure 3.1(f)). Such structured films of different thicknesses (6.3 nm and 8.4 nm) having crack-like voids have been used by F. Niekiel et al [12] as an irreversible temperature sensor. Here, it has been observed that among the variety of RSP's, only the material CAF can be defined for all the films, which can correlate the morphological transformation and transition thresholds of various stages of growth from island-like structure to a continuous film. The CAF of the films increases monotonically with an increase in the thickness towards the saturation point (100% material coverage) (Figure 3.2(d)). Initially, the CAF of the films increases very fast, which corresponds to lateral growth of the nanostructures and becomes slow for higher thickness indicating a vertical growth in the nanostructures, which finally provides either semicontinuous or continuous films.

Similar increment in the CAF has been found in the case of growth of Au thin film on the Si, SiO_2 and quartz substrate [34].

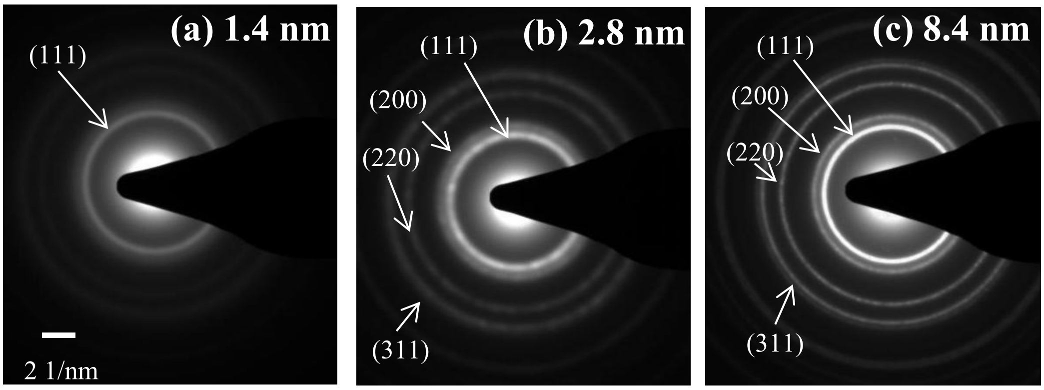

Figure 3.3 Electron diffraction pattern of as-deposited Au thin film of different thickness (a) 1.4 nm, (b) 2.8 nm, and (c) 8.4 nm (set-A).

The Figures 3.3(a)-3.3(c) show the electron diffraction pattern of as-deposited Au thin films of different thickness (set-A). The 1.4 nm thickness Au film shows a diffuse ring around the central spot in the electron diffraction pattern. This ring is index as (111) plane of face-centered cubic (fcc) crystal structure of Au. Since (111) plane has highest intensity as compared to other plane. That is why other rings corresponding to lower d spacing planes are not visible. In the case of 2.8 nm thick film, other rings seems to be present apart from (111) ring. Theses rings are index as (200), (220) and (311) planes of fcc crystal structure of Au. This indicates that number of available plane for (200), (220) and (311) have increased as thickness increases. All these rings in the diffraction pattern become relatively sharper for 8.4 nm thick film due to enlargement in the grain size. The diffraction pattern of 8.4 nm thick film indicates that it is equivalent to powder diffraction pattern (Figure 3(c)). The concentric rings indicate that as-deposited thin film has a completely random orientation of finer grains (uniformly distributed) having non-textured polycrystalline nature. The average lattice constants obtained from diameters of the diffraction ring corresponding to (111), (200), (220), and (311) planes of fcc crystal is calculated as 0.414 nm, which matches with JCPDF file no 04-0784 (standard a= 0.408 nm).

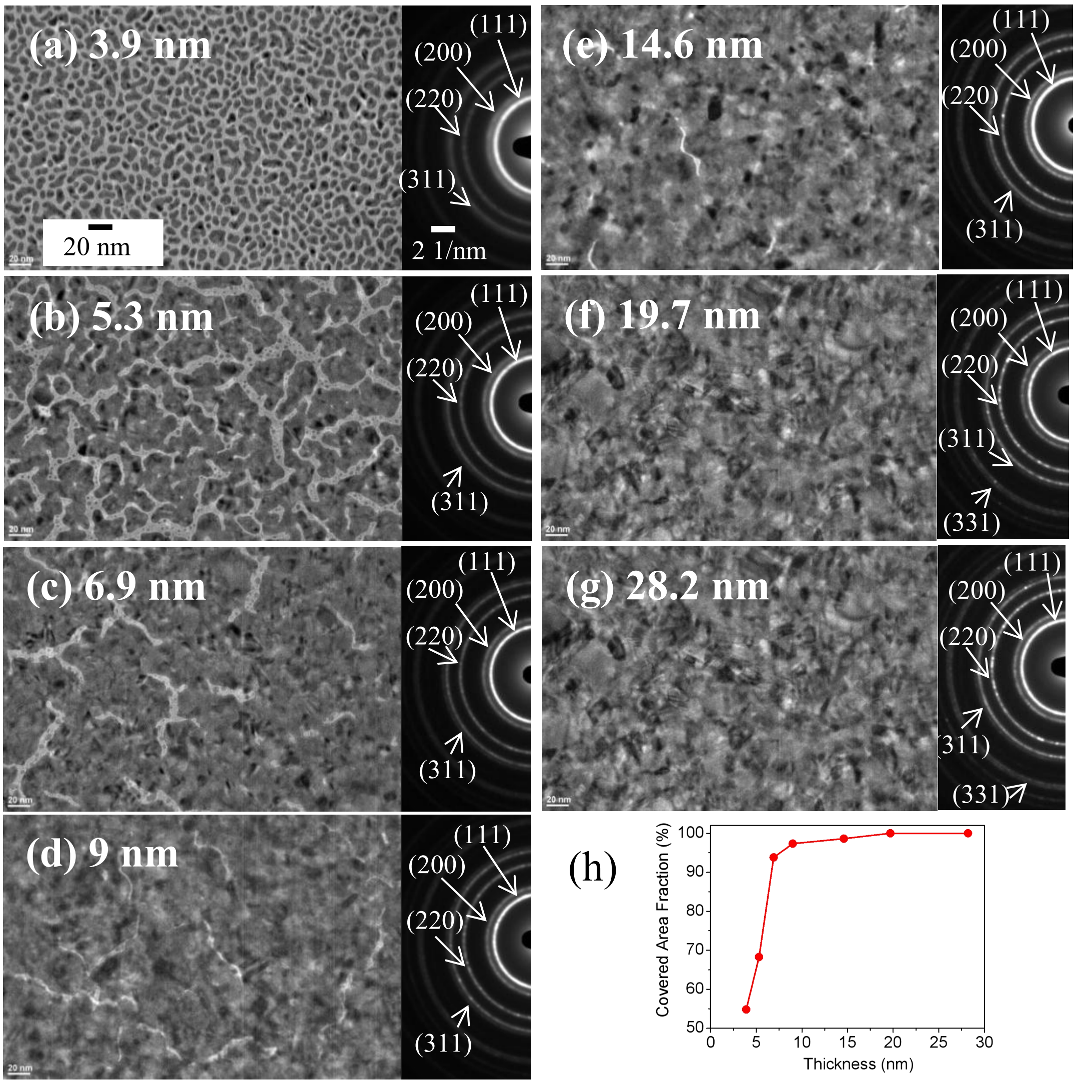

Figure 3.4 TEM image and electron diffraction pattern of as-deposited different thickness of Au thin films (a) 3.9 nm, (b) 5.3 nm, (c) 6.9 nm, (d) 9 nm, (e) 14.6 nm, (f) 19.7 nm, (g) 28.2 nm. (h) Variation in covered area fraction with Au film thickness (set-B).

3.3 Morphological characterization of as-deposited Au film (set-B)

In the previous section, the growth of Au thin film is studied for lower deposition rate (10 mA) and for limited thickness range (≤ 8.4 nm). To expand the analysis of growth process, Au thin films (set-B) is also grown at higher deposition rate and for larger thickness range. The deposition is carried out at 20 mA for 10, 20, 30, 40, 60, 80 and 120 s. The thickness have been calculated as 3.9, 5.3, 6.9, 9, 14.6, 19.7 and 28.2 nm for 10, 20, 30, 40, 60, 80 and 120 s deposition time respectively. Figure 3.4 represent the plan view TEM images and electron diffraction of as-deposited Au thin film grown at higher deposition rate (set-B). Analogous to set-A, the various stages of growth are observed in TEM images of set-B. The 3.9 nm thick Au film has discrete but elongated shape nanoparticles. The 5.3 nm thick film has ginger shape Au nano-structures. In the case of 6.9 nm to 14.6 nm film thickness range, some trenches appears in the percolated structure of Au films. The number as well as size of the trenches reduces as thickness of the Au film increases. The Au thin film becomes fully continuous for 19.7 nm thickness. Similar to set-A average values and distribution of RSP's of as-deposited Au thin films are also calculated for set-B.

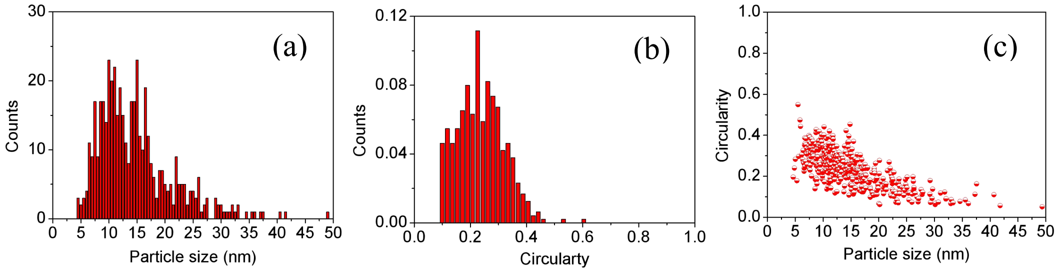

Figure 3.5 Particle distribution, circularity distribution, variation in circularity with particle size for 3.9 nm thickness film of set-B. All the plots are obtained from Figure 3.4 (a) using ImageJ software.

Figures 3.5(a)-3.5(c) presents the statistical distribution in RSP's for 3.9 nm thickness Au film. The particle size and circularity are found as 14.3 nm ±10.5 nm and 0.24 respectively. The number density was obtained as ~5.9×10^3 μm^{-2}. Here, it is important to emphasize that for 3.9 nm thickness film particle size is maximum and circularity is minimum among all samples of both set-A and set-B. Moreover, the particle size and circularity distribution is also broadest (Figures 3.5(a)-3.5(b)). Figure 3.5(c) shows that the circularity reduces with particle size. This behavior is very much similar to all other Au thin films of set-A which are grown at lower deposition rate. In set-B, the calculation of RSP's are also restricted for 3.9 nm thick film due to percolation in the film. However, CAF is still can be obtained for all the films. The Figure 3.4(h) depicts the variation in CAF with Au film thickness. The CAF for 3.9 nm thick film is found as ~54.8 %. The CAF increases with thickness of Au film. It is observed that for 3.9 nm to 6.9 nm thickness range CAF increases rapidly, while for 9 nm to 19.7 nm thickness range variation in CAF abruptly become very slow up to saturation point (100 % CAF). However, CAF of Au thin film for set-A increases in a systematic way (Figure 3.2 (d)).

The electron diffraction pattern of as-deposited Au thin films of set-B also recorded using TEM. The 3.9 nm thick as-deposited Au film shows four concentric rings in electron diffraction pattern, which are equivalent to powder electron diffraction pattern (Figure 3.4(a)). The diffused (111) and (200) and faint (220) and (311) intensity of concentric rings consistently become sharper as thickness increased to 14.6 nm but diffraction pattern still shows polycrystalline ring. For 19.7 and 28.2 nm thick film (fully continuous), a new concentric ring corresponding to lower d spacing plane (331) is also visible in the electron diffraction pattern. The polycrystalline ring become sharper as the film thickness increased. This is due to the enlargement in the grains. All the above observations are in agreement with the earlier reported results of Volmer-Weber type growth, where atoms aggregate and start nucleating to form purely discrete island film during the early stage of the deposition [21]. The island coalesces in the case of longer deposition time resulting in the formation of the continuous film via semicontinuous intermediate states [35]. This indicates that one can optimize the deposition parameters to obtain a better film to be used as a sensor for different applications.

3.4 Morphological characterization of annealed Au film

An in-situ monitoring of changes in the morphology of Au films during the post-deposition annealing is carried out in TEM. Figure 3.6 shows the plan view of TEM images of as-deposited and annealed Au thin films (set-A). Images are recorded at 150°C for 0, 10, 60, 120, and 300 min of annealing time for 2.8 nm and 4.2 nm thick Au film and are shown in Figures 3.6(a-1)-3.6(a-5) and Figures 3.6(b-1)-3.6(b-5) respectively. For the films with 6.3 nm and 8.4 nm thicknesses, images are recorded at 250°C for 0, 5, 30 and 180 min of annealing time. Further, images of subsequent annealing of the same film at 350°C for 5 and 90 min as well as at 500°C for 5 and 300 min are shown in Figures 3.6(c-1)-3.6(c-8) and Figures 3.6(d-1)-3.6(d-8) respectively. The longer duration annealing was done because no significant morphological changes has been observed for shorter time. The film with 2.8 nm thickness indicates that the pre-existing elongated nanoparticles dissociate into smaller nanoparticles having nearly circular (spherical) shape via morphological transformation within 10 min of annealing. The average particle size reduces to ~8.7 nm ±2 nm (Figure 3.6(a-5)) as compared to the as-deposited sample which was 10 nm ±4.1 nm (Figure 3.6(a-1) and Figure 3.1(c)). It resembles that elongated structures having 3 to 4 individual particles weakly connected in the chain are either very much unstable that dissociate into smaller particles or shrinkage of elongated structures into smaller particles. This results in the reduction of average particle size during annealing. Average circularity is also improved to 0.77, whereas the number density slightly decreased to ~7.7×10^3 particle/μm^2 (Table-3.1). Here, it is expected that the number density of the nanoparticles should increase after its detachment from the elongated particles into an individual circular (spherical) particles. It might be due to the expense of some of the nearest smaller particles converting into the bigger

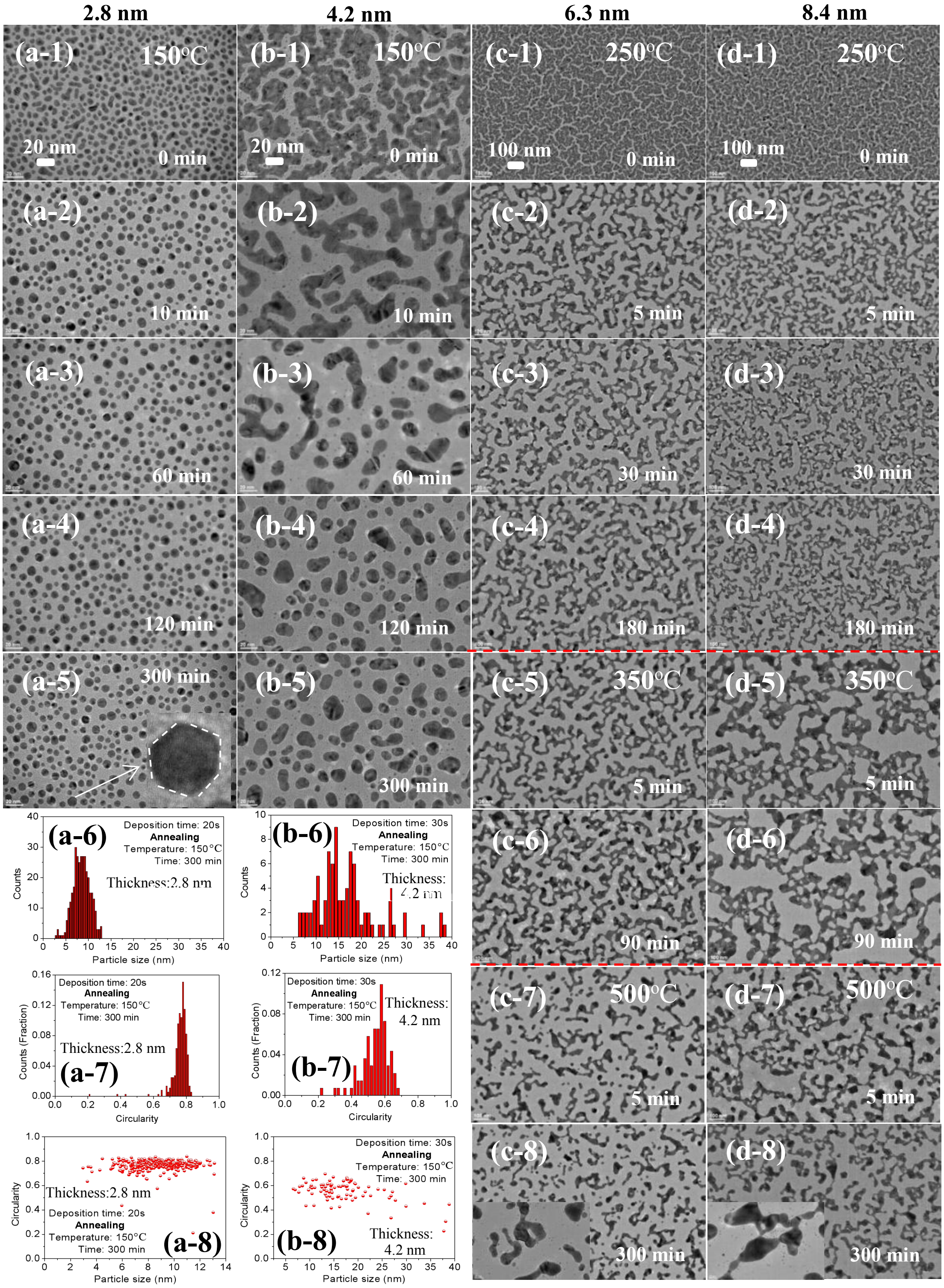

Figure 3.6 In-situ TEM images of Au thin films during post-deposition annealing for thickness of (a-1)-(a-5) 2.8 nm, (b-1)-(b-5) 4.2 nm, (c-1)-(c-8) 6.3 nm, and (d-1)-(d-8) 8.4 nm. Particle size distribution, circularity distribution and variation in circularity with particle size for (a-6)-(a-8) 2.8 nm and (b-6)-(b-8) 4.2 nm thickness Au films (obtained from Figure 3.6(a-5) and Figure 3.6(b-5)).

particles via surface diffusion process [36]. These results suggest that it is a competition between the dissociation and coalescence in a single process through energy minimization mechanism. It is the case where highly circular nanoparticles are formed, which is the most desirable condition for excitation of narrower full width at half maxima (FWHM) of LSPR for surface-enhanced spectroscopy as well as for sensors [13]. However, a further increase in the annealing time (300 min) makes no significant change in any of the parameters of the nanoparticles. Very close observation depicts that some of the Au nanoparticles are having hexagonal shape that is the consequence of surface energy minimization related to thermodynamic factors (Inset of Figure 3.3(a-5)). The size distribution of the Au nanoparticles in the annealed film becomes narrower and symmetric around average particle size (Figure 3.3(a-6) obtained from Figure 3.3(a-5)), while in the as-deposited film, size distribution was broad and highly asymmetric (Figure 3.2(c-1)). Moreover, the whole distribution pattern of circularity also shifts towards higher value (c_{ave} ~0.77) with a narrow distribution under the effect of annealing (Figure 3.6(a-7)). Figure 3.6(a-8) shows the variation in circularity with the size of Au nanoparticles (obtained from Figure 3.6(a-5)). The circularity is found almost constant for all the particle sizes, while it was decreasing for larger particle sizes in all the as-grown samples. This indicates that annealing of the films is beneficial for getting the large number of spherical nanoparticles that provides a comparatively sharp LSPR peak [37] [38] [39].

In the case of 4.2 nm film thickness, shrinking and smoothening occurs in the film morphology during the early stage of annealing (≤10 min) resulting in the crocodile-like structures (Figures 3.6(b-1)-3.6(b-2)). After that, detachment of crocodile-like structures has started via morphological transformations (depercolation). At 60 min of annealing, some spherical nanoparticles along with other complex structures are formed by depercolation process (Figure 3.6(b-3)). These complex nanoparticles are transformed into separate spherical and asymmetric dumb-bell like shapes as annealing proceeds to 120 min, where depercolation process seems to be completed (Figure 3.6(b-4)). This condition appears to be the threshold for percolation to island transition state for this particular case. Further annealing up to 180 min makes the nanoparticles shape more spherical by energy minimization principle. This region of annealing can be defined as circularity improvement region (image not shown). Annealing beyond 180 min makes very slow changes in the morphology so that sizes and shapes of the particles remain almost constant up to 300 min. The average particle size, number density, and average circularity (obtained from Figure 3.6(b-5)) are 17.1 nm ±6.9 nm, 2.9×10^3 particle/μm^2 and 0.55 respectively (Table-3.1). Here, the distribution of particle size is broad and asymmetric that extends up to ~38 nm, while the circularity distribution is almost symmetric around its average value. The particle circularity with its size remains nearly constant (~0.55) up to 25 nm, but for larger particle size (~38 nm) it decreases to 0.2. In this case, the particles having small size (~2 nm) are also formed that are excluded from the calculation of average particle size, standard deviation, circularity and number density.

Figure 3.6(c-1) shows the crack-like voids in the percolated structure (semicontinuous film) with ~70 % CAF in the film of 6.3 nm thickness. Figure 3.6(c-2) indicates that the depercolation rate is higher at an early stage of the annealing process (250°C, 5 min annealing time), where CAF reduces very fast up to ~39 %. Finally, this depercolation rate is found saturated after ~30 min of annealing (Figures 3.6(c-3)-3.6(c-4)). A subsequent annealing at 350°C temperature is performed for 90 min to break this saturation condition of depercolation. It is found a very less efficient way of accelerating the depercolation process (Figures 3.6(c-5)-3.6(c-6)).

However, further increase in the annealing temperature up to 500°C for 5 min indicates that most of the cross-linking are broken to form a very complex chain structures (Figure 3.6(c-7)). Here, breaking of cross-links is monitored up to 300 min at 500°C, which provides a significantly reduced length of chain structure (Figure 3.6(c-8) and its inset). These results are found in agreement with the earlier reported results for the continuous films, solid-state dewetting start with an incubation time, which is necessary to nucleate the voids [11],[40],[41] while dewetting in the semicontinuous films start directly with the growth of pre-existing crack-like voids [12]. These pre-existing voids grow laterally during the annealing process.

Figures 3.6(d-1)-3.6(d-4) indicates that in the case of 8.4 nm thick film most of the morphological self-organization is completed within 5 min with a reduction of CAF from ~75% to ~43%, and saturates for the annealing time >5 min similar to the 6.3 nm thick film. However, the complex structures have more number of long network linkages of thinner width in comparison to 6.3 nm thick films during similar temperature and annealing time. Thinning and the number of network linkages depends on the degree of percolation present in the as-deposited film. In this case also the annealing temperature is increased subsequently to 350°C for 90 min to break this dewetting saturation. During this process, the coalescence of thinner branches occurs resulting in the reduction of some network linkages along with an enhancement in the open area that reduces the CAF up to 40%. Annealing at 350°C for 90 min is not sufficient for breaking the network linkages. Further, the annealing temperature is increased to 500°C. After 5 min, some of the networks break, whereas rest of the networks produces islands at the cost of the network linkages (Figure 3.6(d-7)). However, 300 min annealing makes small increment in the number of isolated islands along with a significant reduction in the number of cross-linking branches as well as its length (Figure 3.6(d-8)). But still cross-linking seems to be present in the Au network film, while in the case of 6.3 nm thickness film (Inset Figure 3.6(c-8)) most of the cross-linking in the network were broken. Cross-linking networks can be seen in higher magnification images (inset of Figure 3.6(d-8)) that shows two types of (large and small sizes) elliptical shaped blocks. It indicates that the degree of initial percolation profoundly influence the morphology of the annealed films, while the path of the dewetting appears almost similar. These results show that the temporal morphological evolution obtained by annealing the 8.4 nm thick film is very much similar to 6.3 nm thick film. It seems that continuous films of different thicknesses and percolated films of varying degree of percolation follow similar morphologies after annealing at different temperature and time combination. The observed results of 6.3 nm and 8.4 nm thick films are found in agreement with the results reported earlier, where Au films were deposited on the SiN_4 thin film supported by TEM grid, [12] but the annealing temperature and the time scale were different.

Change in the CAF with annealing time for 2.8, 4.2, 6.3 and 8.4 nm thick films annealed at 150˚C and 250˚C is shown in Figure 3.7 (obtained from Figure 3.6). Figure 3.7(a) indicates that the CAF decreases faster in the case of 2.8 nm thick film

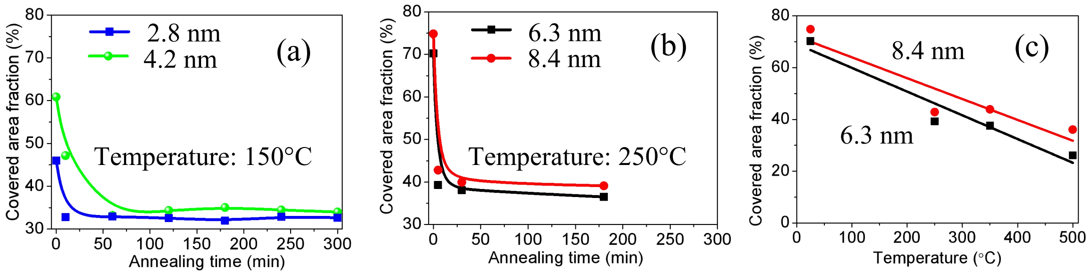

Figure 3.7 Variation in the covered area with annealing time (a) 2.8 and 4.2 nm thickness, (b) 6.3 nm and 8.4 nm thickness Au thin films, (c) variation in the covered area with the temperature for 6.3 nm and 8.4 nm thickness Au thin films (5 min annealed). All the plots are obtained from Figure 3.6 using ImageJ software.

in comparison to the 4.2 nm thick film. No variation was noted in either of the films after ~60 min of annealing. This also indicates that the CAF decreasing rate is substantially large at the initial stage of the thermal dewetting process, which becomes infinitesimally small for a longer time of annealing. Similarly, the CAF decreases very fast in the case of 6.3 nm and 8.4 nm thick films when annealed at 250˚C (Figure 3.7(b)). This variation saturates after 30 minutes of annealing. The change in the CAF with temperature is plotted for 6.3 nm and 8.4 nm thick films. The CAF of the annealed films have been obtained after 5 min annealing at each temperature (from room temperature to 500˚C, obtained from Figure 3.6). It is noted that CAF decreases linearly with an increase in annealing temperature. These results indicate that during isothermal annealing the variation in a covered area is dependent on the film thickness, annealing temperature and on the annealing time. Formvar-coated TEM grid for Au films deposition is found comparatively more straightforward technique to study the dynamics of thermal dewetting during in-situ annealing. The annealing results of 2.8 nm and 4.2 nm thickness Au films deposited on the formvar film substrate provide almost spherical particles at the end of the long time annealing. Such samples have important applications for surface-enhanced spectroscopy and sensors. This technique may also be applicable for the size-dependent plasmonic study of Au nanostructure films along with optical response and CAF based irreversible temperature sensor [42], [43].

The crystal orientation during dewetting of Au grains (crystallization) are also monitored during the annealing process by recording in-situ electron diffraction pattern for the 8.4 nm thick film. As discussed earlier the as-grown sample shows four continuous diffraction rings in electron diffraction pattern, which is equivalent to the powder diffraction pattern (Figure 3.8(a)). The diffraction rings indicate that as-

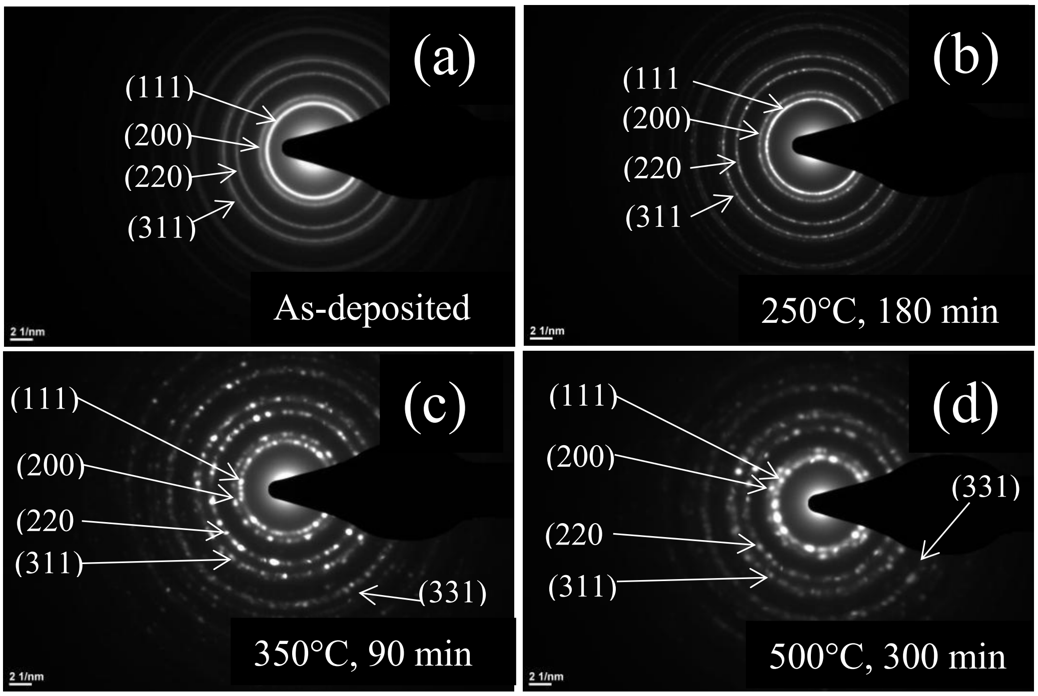

Figure 3.8 Variation in the electron diffraction pattern of Au thin film (8.4 nm thickness) with annealing time (a) as-deposited, (b) 250°C, 180 min, (c) 350°C, 90 min (d) 500°C, 300 min.

deposited thin film has a completely random orientation of finer grains (uniformly distributed) having non-textured polycrystalline nature. After annealing at 250°C for 180 min, the diffraction pattern shows sharpening in the rings due to an increase in the crystallite size (Figure 3.8(b)). The nature of diffraction pattern is still almost like a powder diffraction pattern. It means that each grain has a random orientation with respect to the incident electron beam. Subsequent annealing at 350°C for 90 min produces discrete spots in all four diffraction rings along with generations of a new fifth diffraction ring corresponding to (331) plane (Figure 3.8(c)). The presence of some other bright spots outside of the 5th ring corresponds to the emergence of other lower d spacing planes, which is due to the crystallization process along with enlargement in the grain size and reduction in the random orientation of each plane. Normally, the crystallization and enlargement of grain size are required for the minimization of surface energy and the strain in the thin films during the dewetting process. Further, an increase in the temperature and annealing time results in an enhancement in the brightness of the spot present in the diffraction pattern rings indicating an improvement in the degree of crystallization due to enlargement in the grain size (Figure 3.8(d)). A similar experiment was performed earlier to study the continuous Au thin films deposited on the glass, mica, and silicon. The electron diffraction patterns obtained from the Au thin films deposited on glass and mica substrates have offered a textured growth, whereas Au thin films deposited on Si substrate offered a non-textured growth. However, all the Au films showed the grain size enlargement during the annealing process [44].

3.5 Conclusions

A detailed statistical analysis of the growth of ultra-thin gold (Au) films of 0.7 nm to 28.2 nm thickness deposited by sputtering on formvar film has been carried out to understand the growth mechanism. Various stages of growth (island, partial coalesce, percolation and continuous) are identified in terms of real space parameters (RSP’s) like particle size, circularity, number density and the covered area fraction (CAF) using TEM, which full fills the demand of controlled morphological growth of Au thin films. For the films grown at lower deposition rate, the partial coalesce stage and island to percolation transition threshold are found for ~3 nm and ~4 nm thick film respectively. The films with thickness <3 nm have mainly nanoparticles of spherical shapes, whereas the sizes and shapes of Au nanoparticles change with an increase in the film thickness. The Au films grown at higher deposition rate always shows elongated shape indicating higher degree of coalesce at initial stage of the growth. The higher deposition rate also abruptly increases filling rate of materiel coverage area on the substrate. Annealing of the island film at 150˚C temperature shows an increase in the average circularity (sphericity) of the particles with an excellent thermal stability. The just percolated film shows transition threshold for percolation to island state after ~120 min annealing that results in discrete spherical nanoparticles along with some dumb-bell, tri-bell (triangular) and more complex geometries. The percolated Au film annealed at 250˚C temperature up to 180 min shows that the solid-state dewetting saturates within 5 min, whereas subsequent high-temperature annealing (from 350˚C to 500˚C) accelerates the dewetting and provides complicated but discrete chain-like structures. The highly percolated Au thin film also shows similar dewetting dynamics resulting in very complicated nanostructures having cross-link and branched network geometries. The above results indicate that similar spherical size nanoparticles of Au can be obtained by using thermal dewetting process, which can be used as a plasmonic sensor for enhancing the sensitivity of surface-enhanced spectroscopy. The electron diffraction of as-deposited Au thin films explain the formation of crystal planes as well as increment in number and size of the grains during growth. An in-situ electron diffraction study of the highly percolated film shows an improvement in the crystalline nature of the film along with an enlargement in the grain size during the annealing process. Finally, these results provide a better understanding of getting Au nano-structured films via growth and dewetting process on the formvar film for different applications.

References:

[1] Z. J. Jiang, C. Y. Liu, and L. W. Sun, “Catalytic properties of silver nanoparticles supported on silica spheres,” *J. Phys. Chem. B*, vol. 109, pp. 1730–1735, 2005.

[2] L. Mcewan, M. Julius, S. Roberts, and J. C. Q. Fletcher, “A review of the use of gold catalysts in selective hydrogenation reactions,” *Gold Bull.*, vol. 43, no.

4, pp. 298–306, 2010.

[3] V. Torrisi, F. Ruffino, A. Licciardello, M. G. Grimaldi, and G. Marletta, "Memory effects in annealed hybrid gold nanoparticles/block copolymer bilayers," *Nanoscale Res. Lett.*, vol. 6:167, pp. 1–8, 2011.

[4] Y. Akimov *et al.*, "Enhancement of optical absorption in thin-film solar cells through the excitation of higher-order nanoparticle plasmon modes," *Opt. Express*, vol. 17, no. 12, pp. 10195–10205, 2009.

[5] S. Szunerits, M. R. Das, and R. Boukherroub, "Short- and long-range sensing on gold nanostructures, deposited on glass, coated with silicon oxide films of different thicknesses," *J. Phys. Chem. C*, vol. 112, no. 22, pp. 8239–8243, 2008.

[6] E. Galopin *et al.*, "Short- and long-range sensing using plasmonic nanostrucures: Experimental and theoretical studies," *J. Phys. Chem. C*, vol. 113, no. 36, pp. 15921–15927, 2009.

[7] A. Merlen, V. Gadenne, J. Romann, V. Chevallier, L. Patrone, and J. C. Valmalette, "Surface enhanced Raman spectroscopy of organic molecules deposited on gold sputtered substrates," *Nanotechnology*, vol. 20, no. 215705, pp. 1–7, 2009.

[8] G. Q. Liu *et al.*, "Surface-enhanced Raman scattering effect of gold nanoparticle arrays: The influence of annealing temperature, excitation power and array thickness," *Optik*, vol. 124, pp. 5124– 5126, 2013.

[9] C. Worsch, M. Kracker, W. Wisniewski, and C. Rüssel, "Optical properties of self assembled oriented island evolution of ultra-thin gold layers," *Thin Solid Films*, vol. 520, pp. 4941–4946, 2012.

[10] X. Liu *et al.*, "Tunable dipole surface plasmon resonances of silver nanoparticles by cladding dielectric layers," *Sci. Rep.*, vol. 5:12555, pp. 1–7, 2015.

[11] C. Manuela Muller and R. Spolenak, "Dewetting of Au and AuPt alloy films: A dewetting zone model," *J. Appl. Phys.*, vol. 113, no. 94301, pp. 1–13, 2013.

[12] F. Niekiel, P. Schweizer, S. M. Kraschewski, B. Butz, and E. Spiecker, "The process of solid-state dewetting of Au thin films studied by in situ scanning transmission electron microscopy," *Acta Mater.*, vol. 90, pp. 118–132, 2015.

[13] A. Herz *et al.*, "Solid-state dewetting of single- and bilayer Au-W thin films: Unraveling the role of individual layer thickness, stacking sequence and oxidation on morphology evolution," *AIP Adv.*, vol. 6, no. 35109, pp. 1–10, 2016.

[14] K. Grochowska, K. Siuzdak, J. Karczewski, M. Szkoda, and G. Śliwiński, "Properties of thermally dewetted thin Au films on ITO-coated glass for biosensing applications," *Plasmonics*, vol. 12, no. 6, pp. 1939–1946, 2017.

[15] U. Kreibig and M. Vollmer, *Optical properties of metal clusters*. Berlin:

Springer, 1995.

[16] I. Stabrawa *et al.*, “Investigation of gold nanolayer properties using X-ray reflectometry and spectroscopic ellipsometry methods,” in *Acta Physica Polonica A*, 2016, vol. 129, no. 2, pp. 233–236.

[17] O. Guselnikova *et al.*, “Surface modification of Au and Ag plasmonic thin films via diazonium chemistry: Evaluation of structure and properties,” *Colloids Surfaces A Physicochem. Eng. Asp.*, vol. 516, pp. 274–285, 2017.

[18] T. D. Phuc, M. Yoshino, A. Yamanaka, and T. Yamamoto, “Effects of morphology of nanodots on localized surface plasmon resonance property,” *Int. J. Autom. Technol.*, vol. 8, no. 1, pp. 74–82, 2014.

[19] T. Karakouz, A. B. Tesler, T. Sannomiya, Y. Feldman, A. Vaskevich, and I. Rubinstein, “Mechanism of morphology transformation during annealing of nanostructured gold films on glass,” *Phys. Chem. Chem. Phys.*, vol. 15, no. 4656, pp. 4656–4665, 2013.

[20] A. B. Tesler, B. M. Maoz, Y. Feldman, A. Vaskevich, and I. Rubinstein, “Solid-state thermal dewetting of just-percolated gold films evaporated on glass: Development of the morphology and optical properties,” *J. Phys. Chem. C*, vol. 117, p. 11337−11346, 2013.

[21] M. Schwartzkopf *et al.*, “Real-time monitoring of morphology and optical properties during sputter deposition for tailoring metal-polymer interfaces,” *ACS Appl. Mater. Interfaces*, vol. 7, pp. 13547–13556, 2015.

[22] R. Saxena, M. J. Frederick, G. Ramanath, W. N. Gill, and J. L. Plawsky, “Kinetics of voiding and agglomeration of copper nanolayers on silica,” *Phys. Rev. B*, vol. 72, no. 115425, pp. 1–7, 2005.

[23] I. Beszeda, I. A. Szabó, and E. G. Gontier-Moya, “Morphological evolution of thin gold films studied by Auger electron spectroscopy in beading conditions,” *Appl. Phys. A*, vol. 78, pp. 1079–1084, 2004.

[24] H. Sun, M. Yu, X. Sun, G. Wang, and J. Lian, “Ultrathin gold island films for time-dependent temperature sensing,” *J. Nanoparticle Res.*, vol. 16:2273, pp. 1–8, 2014.

[25] L. G. Parratt and C. F. Hempstead, “Anomalous dispersion and scattering of X-rays,” *Phys. Rev.*, vol. 94, no. 6, pp. 1593–1600, 1954.

[26] S. Verma, B. Tirumala Rao, S. Rai, V. Ganesan, and L. M. Kukreja, “Influence of process parameters on surface plasmon resonance characteristics of densely packed gold nanoparticle films grown by pulsed laser deposition,” *Appl. Surf. Sci.*, vol. 258, pp. 4898–4905, 2012.

[27] M. Haruta, T. Kobayashi, H. Sano, and N. Yamada, “Novel gold catalysts for the oxidation of carbon monoxide at a temperature far below 0 °C,” *Chem. Lett.*, pp. 405–408, 1987.

[28] M. Valden, X. Lai, and D. W. Goodman, “Onset of catalytic activity of gold

clusters on titania with the appearance of nonmetallic properties," *Science* , vol. 281, pp. 1647–1650, 1998.

[29] M. Haruta and M. Daté, "Advances in the catalysis of Au nanoparticles," *Appl. Catal. A Gen.*, vol. 222, no. 1–2, pp. 427–437, 2001.

[30] T. F. Jaramillo, S. H. Baeck, B. R. Cuenya, and E. W. Mcfarland, "Catalytic activity of supported Au nanoparticles deposited from block copolymer micelles," *J. Am. Chem. Soc.*, vol. 125, pp. 7148–7149, 2003.

[31] S. H. Lee, E. H. Kwak, and G. H. Jeong, "Dewetting behavior of electron-beam-deposited Au thin films on various substrates: graphenes, quartz, and SiO2 wafers," *Appl. Phys. A Mater. Sci. Process.*, vol. 118, pp. 389–396, 2015.

[32] P. Pavaskar *et al.*, "Plasmonic hot spots: nanogap enhancement vs. focusing effects from surrounding nanoparticles," *Opt. Express*, vol. 20, no. 13, pp. 14656–14662, 2012.

[33] P. Pavaskar, I. K. Hsu, J. Theiss, W. H. Hung, and S. B. Cronin, "A microscopic study of strongly plasmonic Au and Ag island thin films," vol. 113, no. 34302, pp. 1–6, 2013.

[34] Y. Li, L. Xu, X. Li, X. Shen, and A. Wang, "Effect of aging time of ZnO sol on the structural and optical properties of ZnO thin films prepared by sol-gel method," *Appl. Surf. Sci.*, vol. 256, pp. 4543–4547, 2010.

[35] K. D. Leaver and B. N. Chapman, *Thin Films*. London, UK: Wykeham Publication, 1971.

[36] M. Y. Li, Q. Zhang, P. Pandey, M. Sui, E. S. Kim, and J. Lee, "From the Au nano-clusters to the nanoparticles on 4H-SiC (0001)," *Sci. Rep.*, vol. 5:13964, pp. 1–13, 2015.

[37] M. Kawasaki and M. Hori, "Laser-induced conversion of noble metal-island films to dense monolayers of spherical nanoparticles," *J. Phys. Chem. B*, vol. 107, pp. 6760–6765, 2003.

[38] I. Doron Mor, Z. Barkay, N. Filip Granit, A. Vaskevich, and I. Rubinstein, "Ultrathin gold island films on silanized glass. morphology and optical properties," *Chem. Mater.*, vol. 16, pp. 3476–3483, 2004.

[39] T. Karakouz, D. Holder, M. Goomanovsky, A. Vaskevich, and I. Rubinstein, "Morphology and refractive index sensitivity of gold island films," *Chem. Mater.*, vol. 21, pp. 5875–5885, 2009.

[40] J. Y. Kwon, T. S. Yoon, K. B. Kim, and S. H. Min, "Comparison of the agglomeration behavior of Au and Cu films sputter deposited on silicon dioxide," *J. Appl. Phys.*, vol. 93, no. 6, pp. 3270–3278, 2003.

[41] C. V. Thompson, "Solid-state dewetting of thin films," *Annu. Rev. Mater. Res.*, vol. 42, pp. 399–434, 2012.

[42] H. Sun, M. Yu, X. Sun, G. Wang, and J. Lian, "Effective temperature sensing by irreversible morphology evolution of ultrathin gold island films," *J. Phys.*

Chem. C, vol. 117, pp. 3366–3373, 2013.

[43] H. Sun, M. Yu, G. Wang, X. Sun, and J. Lian, “Temperature-dependent morphology evolution and surface plasmon absorption of ultrathin gold island films,” *J. Phys. Chem. C*, vol. 116, pp. 9000–9008, 2012.

[44] Y. Golan, L. Margulis, and I. Rubinstein, “Vacuum-deposited gold films I. Factors affecting the film morphology,” *Surf. Sci.*, vol. 264, pp. 312–326, 1992.

Chapter 4

Study of aging effect on the ultra-thin gold films

4.1 Introduction

Plasmonic nanostructured thin films are proved to be highly useful structures in various advanced applications like ultra-sensitive surface-enhanced Raman spectroscopy (SERS) [1], [2], transmission surface plasmon resonance (T-SPR) spectroscopy [3], and photovoltaic solar cell [4]. SERS has established a benchmark in the detection of Raman active molecules at ppm level. Even reports on the detection of a single molecule are also available in the literature [5]. The fast response of plasmonics-based T-SPR spectroscopy for accurate refractive index measurement makes it a versatile scheme for sensing chemical, biological and gas ambiance up to sub-monolayer level [6]. In solar cells, plasmonic thin films play a vital role in the development of highly efficient methodology for improving the light harvesting capability [7], [8]. Localized surface plasmon resonance (LSPR), the generation of coherent oscillations of free electron plasma in the metal nanostructures in the presence of light, is the fundamental phenomenon behind each of the above mentioned applications as described in chapter 1. Extensive theoretical and experimental studies on plasmonic nanostructures are compiled to explore the parametric dependence for optical excitation of LSPR. Moreover, the established comprehensive understanding of the LSPR excitation is very much useful for fundamental, and engineering proposes [9], [10]. In the plasmonic thin films, the optimization of its morphological (size, shapes, number density, inter-particle spacing, and covered area fraction) [11] and material (pure metallic, alloy and bimetallic) [12] parameters along with dielectric cladding layer thicknesses (effective dielectric constant) [13] are required for tuning the optical response of metal nanostructures. This ultimately decides the performance of any of the particular plasmonic devices and sensors. However, the stability of optical response of plasmonic nanostructured thin films against aging (ambient conditions) is essential for its short as well as long-term applicability in each plasmonic devices [14]–[16]. The aging of metallic thin films in environmental ambiance is a phenomenon that reduces its efficiency and durability for most of the practical applications mainly due to oxidizing nature of metals [17]. On the other hand, this detrimental aging effect offers a new innovative prospect to enhance the plasmonic response of nanostructured gold (Au) thin films deposited on transparent substrates. Mainly, it reduces the broadening of pre-existing LSPR peak of Au island films and induces a new LSPR peak in the region of a flat optical response of percolated and continuous Au thin films [18], [19]. However, the proper explanation of underlying physical mechanisms involved in the process is obscure. In this chapter, the Au thin films deposited on glass substrate are used to study aging effect on the plasmonic response, morphological and crystallographic properties in ambient condition. As described in chapter 2, the Au thin films are deposited on formvar film and glass substrates by sputtering techniques in similar growth conditions. Two sets of Au thin film samples of different thickness at different deposition rates are prepared. In set-A, deposition is carried out at 10 mA sputtering current for 5, 10, 15, 20, 30, 45 and 60 s time. In set-

B the deposition is carried out at 20 mA sputtering current for 10, 15, 20, 30, 40, 45, 50, 60, 80, 120 s time. The Au thin films deposited on formvar film are used to study the growth and dewetting behaviour using TEM as described in previous chapter (chapter 3). The absorbance of the Au thin films deposited on glass substrate is recorded at various stages of the aging to study variation in plasmonic response. The morphological variation in as-deposited and aged (four months) Au thin films deposited on glass substrate is recorded using XRR, AFM and GIXRD techniques. Finally, aged (four months) Au thin films are also subjected to SERS applications.

4.2 Plasmonic response of as-deposited Au thin films

EDS characterization is performed for elemental characterization of cleaned float glass and Au thin film deposited on float glass using 30 keV electron beam in SEM (Figures 4.1(a)-4.1(b)). The EDS spectra of glass substrate show different peaks corresponding to characteristic x-rays of various elemental constituents (O, Na, Mg, Al, Si, K, and Ca) present in the float glass (Figure 4.1(a)). The large intensities corresponding to elements O and Si indicates the presence of major percentage of theses elements. The atomic % of the elements in the bare substrate are found as 69.4% O, 13.7% Si, 12.2% Na, 3% Mg, 1% Al, 0.1% K, and 0.6% Ca. Figure 4.1(b) represents that different characteristic x-rays (L_α=11.4 keV, L_β=9.7 keV and M_α=2.2 keV) of Au appear with the characteristic x-ray peaks corresponding to constituent elements of bare glass. The inset in the Figure 4.1(b) display the enlarged picture of high energy peaks of Au present in the EDS spectra.

The growth of Au thin films on the glass by the sputtering technique is referred as the Volmer-Weber type, in which islands are formed at the early stage of deposition. These islands become large enough to coalesce each other at a later time of deposition due to their proximity [20], [21] which results in a continuous film via the different degree of percolation stages [22]. In chapter 3, all the stages of Au thin film are observed using TEM, in which Au thin films are deposited on formvar film in similar growth condition. It is well known that the Au island films show peaks in the absorbance spectra due to collective resonant oscillation of conduction band electrons in metal known as localized surface plasmon resonance (LSPR). This characteristic LSPR peak leads to a redshift with increment in the size of the islands due to reduction in the strength of the dipole oscillators [23]. The percolated structure shows

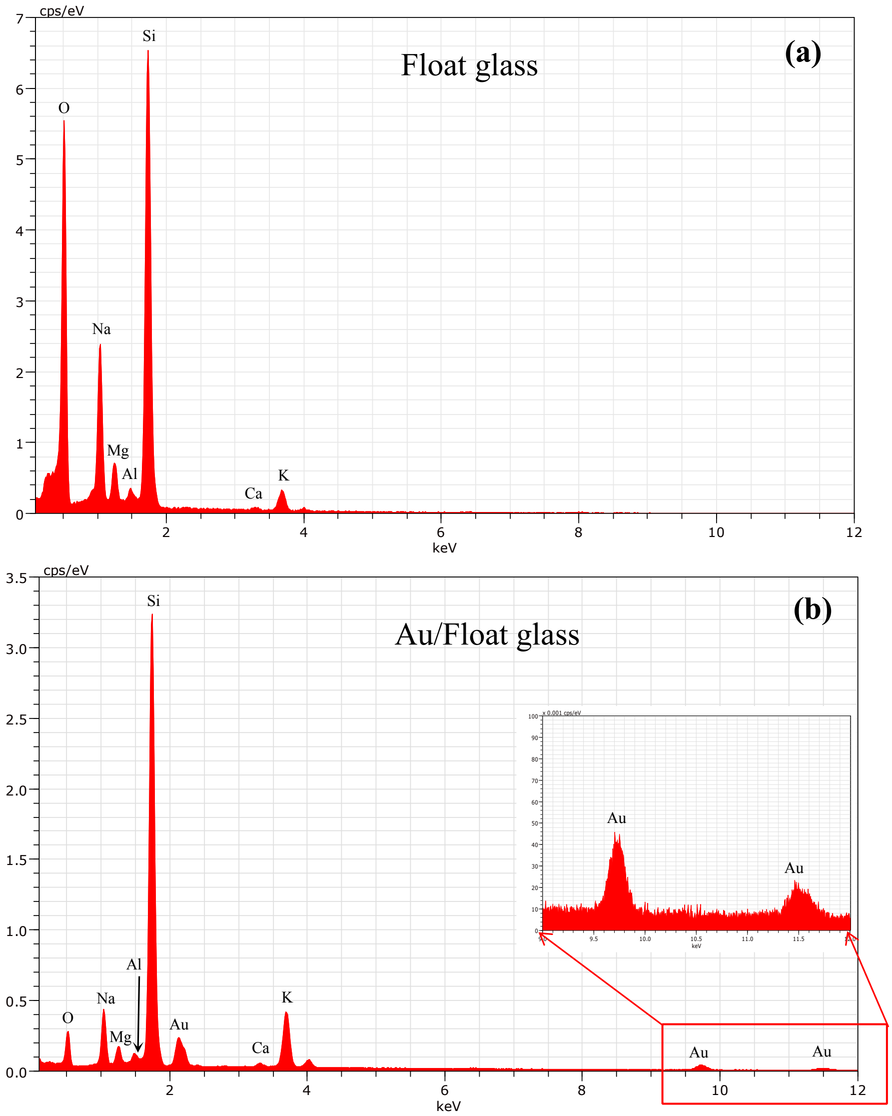

Figure 4.1 EDS spectra of (a) float glass, (b) Au/glass substrates. The insets show the enlarge spectra between 9 to 12 keV energy range.

decrease in the absorbance peak and finally the peak disappear for the continuous film [24]. The optical absorbance spectra of the Au films deposited on glass with thickness varying from 0.7 nm to 8.4 nm are shown in Figure 4.2 (set-A). The Au thin film of 0.7 nm thickness shows a LSPR peak in the absorbance spectra at ~536 nm with a broadening of ~68 nm (Curve-(i)). The LSPR peak position shifts in a consistent manner towards higher wavelength side (red shift) to ~612 nm with the increase in thickness of the film to 2.8 nm as shown by the solid black arrow line (Curve-(i) to Curve-(iv)). The peak shape also concurrently broadened to ~157 nm (due to variation in particle sizes and shapes as shown in TEM images of Figure 3.1 of Chapter 3) [25]. These observations are in accordance with the previously reported results in the literature [26], [27]. However, significant change in the absorbance spectra has been observed for the 4.2 nm thick Au film (Curve-(v)). In this case, LSPR peak position shift to ~756 nm and broadened along with a significant increment in the absorbance at higher wavelength side (dash-doted violet arrow line). The optical behavior of these films is in agreement with the typical optical response of just percolated or densely packed complex shaped nanostructured

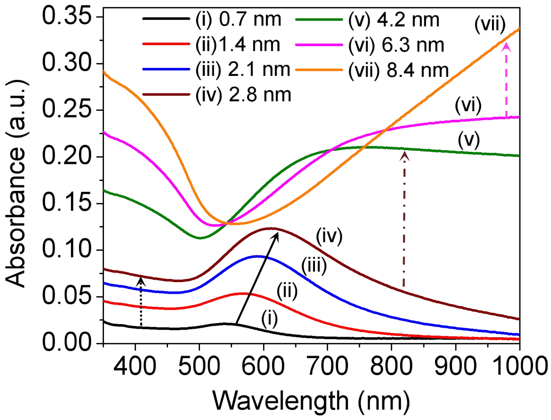

Figure 4.2 Absorption spectra of as-grown Au thin films of different thickness deposited on glass substrate by a sputtering technique at 10 mA sputtering current (set-A).

Au films [24]. In the case of 6.3 nm thickness film, absorbance spectra undergo a sudden drop between 543 nm to 708 nm range in comparison to the absorption spectra of 4.2 nm thick film (Curve-(vi)). However, the absorbance spectra for wavelength >708 nm follow the usual increasing trend. The reduction in the plasmonic response (543 nm to 708 nm) leads to the decrement of absorbance spectra which is the direct depiction of enhancement in the degree of percolation (increment in material coverage fraction via wetting process) of Au thin film on the glass substrate [24]. Further, increase in the thickness of Au thin film to 8.4 nm, reduction in the absorbance become more prominent with an extended wavelength range (543 nm to 790 nm) compare to 6.3 nm thick film (Curve-(vii)). Also, increased absorbance for the wavelength >790 nm (pink dashed arrow line) finally makes the absorbance profile as a nearly straight line (inclined) between 543 nm to 1000 nm wavelength range having minima at 543 nm wavelength. Such kind of monotonically increasing absorbance is the appropriate signature of almost continuous films [28]. It is to be noted that absorbance between 350 nm to 500 nm wavelength range is almost constant for 0.7 nm thick film. In this wavelength range, absorbance corresponds to the inter-band transitions of bound electrons (5d band to conduction band) [29]. The constant level of absorbance in wavelength range <500 nm proportionally increases with the mass-thicknesses of the films as shown by the dotted black arrow line. In the case of 4.2 nm thick film, inter-band absorption level abruptly changes along with the generation of wavelength dependent profile in wavelength range <500 nm. The pattern shows that dominance of inter-band absorption increases as wavelength reduces. Similar behavior of absorbance profiles with a higher absorbance level appeared for >4.2 nm thick films. The absorbance below 350 nm wavelength for all the films corresponds to the fundamental absorption edge of the base material (float glass).

4.3 Plasmonic response of aged Au thin films

In order to see the variation in the plasmonic response of Au thin films with aging, all the films of set-A are aged for a long-time (18 months) in environmental ambiance. Absorbance spectra are plotted in pair (as-deposited and aged) for each of the individual mass-thickness. Figure 4.3 shows the comparison of the absorbance spectra of as-deposited and aged Au films of 1.4, 2.1, 2.8, 4.2, 6.3, and 8.4 nm thicknesses. Figures 4.3(a)-4.3(c) show that the LSPR peak for 1.4 nm to 2.8 nm thick films (island films) are blue shifted along with narrowing in the full width at half maxima (FWHM) of peak after aging. Figures 4.3(d)-4.3(e) depict typical absorbance spectra (broad LSPR profile) for 4.2 nm and 6.3 nm thick as-deposited

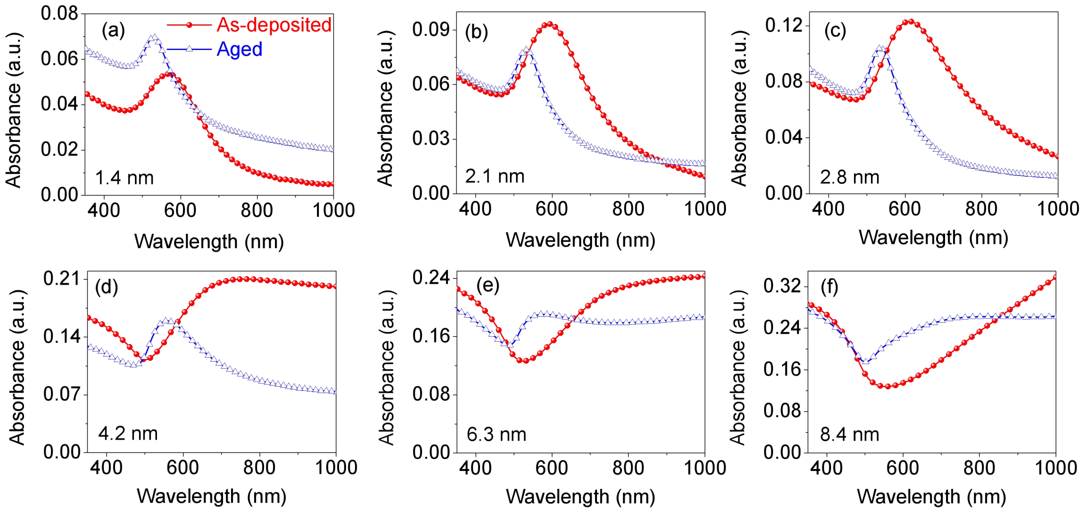

Figure 4.3 A comparison of absorbance spectra of as-deposited and aged Au thin films. The red (sphere) and blue (tingle) curve show the absorbance spectra of as-deposited and aged Au thin films of different thickness (a) 1.4 nm, (b) 2.1 nm, (c) 2.8 nm, (d) 4.2 nm, (e) 6.3 nm, and (d) 8.4 nm. The Au film thickness is determined only for 60 s sample using XRR technique deposition and scaled with time for all the lower thicknesses films.

Au films (just percolated and highly percolated) transformed into a distinct LSPR peak on aging [19]. The peak position of transformed LSPR profiles lies in the visible wavelength range depending upon the mass-thicknesses as well as the degree of percolation. Figure 4.3(f) shows that typical linearly increasing absorbance spectra of a continuous thin film also transformed into a broader profile after aging. The transformation in the optical response of 4.2 nm to 8.4 nm thick Au films are the consequence of the significant reduction of absorbance in both UV and NIR wavelength range (edge regions) as well as enhancement of absorbance in the visible wavelength range (mid part) of the spectrum (Figures 4.3(d)-4.3(f)) [18], [19]. The reduction and enhancement in the absorbance are the consequence of different mass-thickness as well as various morphology present in as-deposited Au films. The reduction in the absorbance in visible and NIR wavelength range is due to the modified response of free electrons whereas the decrease in the absorbance near UV wavelength range is due to the altered response of inter-band transitions of bound electrons.

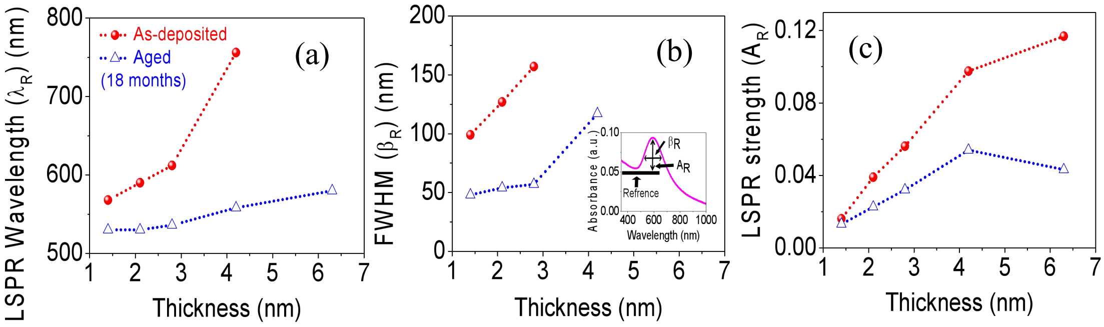

Figure 4.4 Variation in (a) localized surface plasmon resonance (LSPR) peak position, (b) full width at half maxima (FWHM), and (c) LSPR strength with mass-thickness for as-deposited (solid black line) and aged (dotted red line) Au thin films. Solid black and doted red lines are drawn as a guide to eyes for as-deposited and aged samples respectively.

All the results (Figures 4.3(a)-4.3(f)) show evidence of morphological reorganization (dewetting or depercolation) of the Au nanostructures present in the as-deposited films similar to annealing process [30], [31]. The LSPR peak position (λ_R), peak shape broadening (β_R) and relative absorbance or LSPR strength (A_R) for all the as-deposited and the aged films along with their difference ($\Delta\lambda_R$, $\Delta\beta_R$ and ΔA_R) are summarized in Table 4.1. The quantitative comparison of λ_R, β_R and A_R of as-deposited and aged Au thin films (obtained from Figures 4.3(a)-4.3(e)) are also shown in Figures 4.4(a)-4.4(c). The λ_R, β_R and A_R of LSPR peaks are determined using the methodology described earlier [28], [32], [33], in which reference point is taken near the edge of inter-band transition to avoid the change in absorbance due to different mass-thickness of the film (inset Figure 4.4(b)). However, in some of the cases, LSPR peak position and FWHM are difficult to define. The variation in LSPR peak position and broadening with mass-thickness are similar for as-deposited and aged Au thin films except with a lower slope for aged Au thin film (Figures 4.4(a)-4.4(b), Table 4.1). The values of peak position and FWHM are always found lower in the case of an aged thin film in comparison to the fresh one. It is to be noted that for 1.4 nm to 2.8 nm thick aged island films both λ_R and β_R values are very close, while

TABLE 4.1 Localized surface plasmon resonance (LSPR) peak position, full width at half maxima (FWHM) and LSPR strength for as-deposited and aged Au thin films of different thicknesses fabricated on glass substrate by a sputtering technique (set-A).

Thickness (As-grown) (nm)	LSPR peak position (λ_R)			LSPR peak FWHM (β_R)			LSPR strength (A_R)		
	As-grown λ_{R1} (nm)	Aged λ_{R2} (nm)	$\Delta\lambda_R = \lambda_{R2}-\lambda_{R1}$ (nm)	As-grown β_{R1} (nm)	Aged β_{R2} (nm)	$\Delta\beta_R = \beta_{R1}-\beta_{R2}$ (nm)	As-grown A_{R1}	Aged A_{R2}	$\Delta A_R = A_{R1}-A_{R2}$
1.4	568	530	38	98.9	47.9	51	0.016	0.013	0.003
2.1	590	530	60	127	54	73	0.039	0.026	0.016
2.8	612	536	76	157	57	100	0.056	0.032	0.024
4.2		558			117		0.098	0.054	0.044
6.3		580					0.117	0.043	0.074

the as-deposited films show a significant variation in both the parameters with thickness. All the above results indicate that almost similar sizes of the Au nanoparticles are formed in 1.4 nm to 2.8 nm thick film after evolution through aging. Even the sizes of the particles present in the aged Au film are smaller in comparison to the as-deposited film. This means that the lateral dimension of particles (island width) are shrinking and vertical dimensions (island height) are increasing for all the films (Schematic is drawn in section 4.5). Finally, it leads to the increment in the sphericity of the nanoparticles in these films, which might be the reason for the modification in the optical response. It is pertinent to address that particle-particle interaction, and participle-substrate interactions might be less prominent in the aged Au films compared to as-deposited films because of increased inter-particles distance [34] and reduced participle-substrate contacting area via aging-assisted morphological evolution (depercolation). In case of 1.4 mm thickness, absorbance of aged Au thin film is large in comparison to as-deposited Au film while for other thickness films aged film has lower absorbance. It may be due to the modified response of inter-band transitions. To extract the LSPR excitation part, background part (due inter-band absorption) has been subtracted from the absorbance spectra as shown in the inset of Figure 4.4 (b). The LSPR strength (A_R) shows the systematic variations for both as-deposited and aged Au thin film samples. The strength of LSPR peaks (A_R) of both as-deposited and aged films increases monotonically with an increase in film thickness but with a different slope (Figure 4.4(c) and Table 4.1). The consistent increase in the LSPR strength observed in aged Au thin films (1.4 nm to 2.8 nm) simply means that number density of Au particles is increasing with film thickness while particle size remains almost constant [33].

Furthermore, the just percolated structures present in the 4.2 nm thick Au film fully converted into isolated islands after aging and other effects as described above (particle-particle and particle-substrate interactions) also reduces significantly (Figure 4.3(d) and Figure 4.4). Moreover, in the case of 6.3 nm thick Au film, highly percolated structures transformed into complex-shaped structures after aging (Figure 4.3(e) and Figure 4.4). The transformation of optical response of 8.4 nm thick Au film is due to the conversion of continuous film into a highly percolated film having large size patches or voids (Figure 4.3(f)) [30]. All the above optical transformations are strongly correlated with our study carried out in chapter 3. In which growth and dewetting behavior of Au thin films are performed by ex-situ and in-situ respectively by monitoring morphological evaluation using transmission electron microscopy.

4.4 Dynamics of aging effect: An empirical modeling

All the analysis in the previous section is performed for long-term aging (18 months) as well as for limited thickness range (≤8.4 nm). In order to see the dynamical behavior of the phenomenon, the time-evolved variations in optical response of the Au thin films are also examined at various stages of aging (up to 120 days) and for a broader range of thicknesses (set-B). In set-B, samples include all types of Au thin

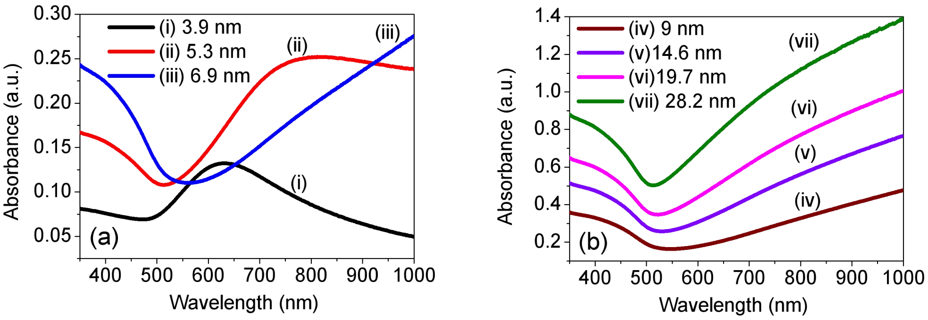

Figure 4.5 Absorption spectra of as-deposited Au thin films of different thickness deposited on glass substrate by a sputtering technique at 20 mA sputtering current (set-B).

films like a separated island, percolated and continuous films as descried in chapter 3. Figures 4.5(a)-4.5(b) show the absorbance spectra of Au thin films having 3.9, 5.3, 6.9, 9.0, 14.6, 19.7, and 28.2 nm thickness corresponding to 10, 20, 30, 40, 60, 80 and 120 s deposition time at 20 mA sputtering current (set-B). The absorbance spectra of Au thin film indicates that all the stage (island, percolated and continuous film) of Au thin film in set-B appears faster compared to set-A because of large deposition rate (20 mA). These result is consistent with the our previous observation carried out in chapter 3, in which CAF of as-deposited Au thin film grown at higher deposition rate increases faster.

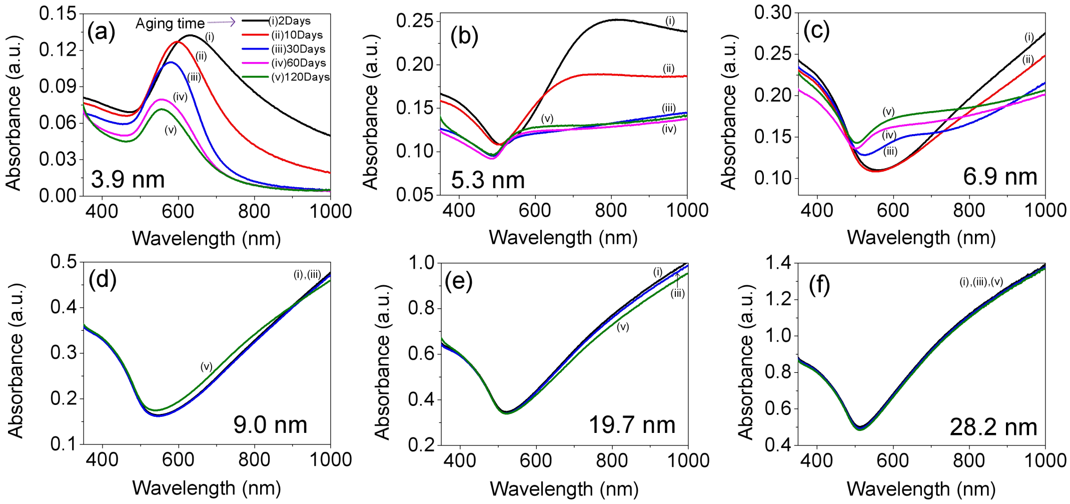

Figure 4.6 Variation in absorbance spectra with aging time for sputtered grown Au thin films of different thickness (a) 3.9 nm, (b) 5.3 nm, (c) 6.9 nm, (d) 9 nm, (e) 19.7 nm, and (f) 28.2 nm. The thickness is obtained by individual fitting of XRR spectra of as-deposited films.

Figures 4.6(a)-4.6(f) show the absorbance spectra of Au thin films having 3.9, 5.3, 6.9, 9.0, 19.7, and 28.2 nm thickness at different aging stages. All the Au thin films of set-B show aging-assisted progressions in the absorbance spectra similar to the observations recorded for Au thin films of set-A (Figures 4.3(a)-4.3(f)). The Au film of 3.9 nm thickness shows a systematic blue shift in LSPR peak position along with a reduction in the peak broadening and its strength (Figure 4.6(a)). The detailed quantitative analysis for empirical modeling for variation in plasmonic response of 3.9 nm thickness film is performed later. At an early stage of aging (2 days) 5.3 nm thick Au film shows broad maxima at ~800 nm wavelength in the absorbance spectra, which is also a pertinent signature of the percolated structure as discussed earlier (Curve-(i) in Figure 4.6(b)). During aging, it shows a systematic reduction in the absorbance spectra for wavelength higher than 600 nm up to 30 days so that absorbance profile become nearly linear to the wavelength axis (Curve-(ii) and (iii) in Figure 4.6(b)). After 30 days, spectra remains unchanged except little enhancement in the absorbance near 600 nm wavelength (Curve-(iv) and (v) in Figure 4.6(b)). Similar types of changes in the absorbance spectra are reported for percolated Au thin films during annealing process [30], [35]. This rapid variation in absorbance at initial stage seems to be dominated via dewetting whereas later gradual changes are promoted by crystallization.

The 6.9 nm thick Au film shows linearly increasing absorbance profile having minima at ~540 nm wavelength at an early stage of aging (Curve-(i) in Figure 4.6(c)). The absence of broad maxima at a higher wavelength in the absorption profile is due to the typical optical response of almost continuous Au thin film. Tesler et al. stated that there is a finite probability of having some voids at metal-air interface whereas metal-glass interface seems to be practically continuous in such kind of optical response [30]. Aging of 6.9 nm thickness Au film shows that changes in absorbance spectra occur in two steps. The initial 10 days of aging, accomplished a moderate reduction in the absorption spectra for higher than ~650 nm (Curve-(ii) in Figure 4(c)). At 30 days of aging it shows drastic enhancement in the absorbance (appearing of a new band) between ~500-700 nm range along with a consistent reduction in absorbance in IR wavelength range (Curve-(iii) in Figure 4.6(c)). This enhancement in the absorbance in the visible wavelength range successively increases even up to 120 days of aging time (Curve-(iv) and Curve (v) in Figure 4.6 (c)). Teslar et al. observe a similar emergence of new bands due to the formation of holes in the films during annealing (creation of the uncovered area on the substrate) [30], [35]. In which a gradual increment in the absorbance (LSPR) and peak width is promoted by the enlargement of hole size or by the increase in the number density of holes on the Au thin film during annealing [30], [35].

Both of the above signatures of variation in the absorbance also arise in the 9.0 nm thick Au film but only at 120 days of aging time (Curve-(v) in Figure 4.6(d)). As the thickness of the Au film increased to 19.7 nm, a little reduction in the absorbance at wavelength ≥600 nm is observed after 30 days of aging (Curve-(iii) in Figure 4.6(e)). This reduction becomes prominent after 120 days of aging without any sign of a new band in the visible range (Curve-(iii) in Figure 4.6(e)). The silver (Ag) thin films of ~20-30 nm thickness have demonstrated a similar reduction in the optical response during aging process [18]. The Au film of 28.2 nm thickness shows no considerable variation in the whole wavelength range even after 120 days of aging (Curve-(i), (iii) and (v) in Figure 4.6(f)). All the above observations show that higher thickness films impose relatively more resistance to the morphological transformation. The films of >28.2 nm thickness can prevent the disruption, which does not show any substantial changes in the morphology during room temperature aging. Finally, it can be concluded that aging and annealing are conjugative processes to each other in which ambient or annealing temperature and the aging or annealing time are the conjugative parameters.

To quantify the mechanism, the values of λ_R, β_R and A_R of LSPR peak with aging time is obtained for 3.9 nm thick film using the similar methodology as described in previous section. Figure 4.7(a) shows the experimental data and best-fitted curve for λ_R. The variation in λ_R is fitted with single-exponential decay function to establish a dynamic model of aging. The value of $\lambda_R(t)$ at aging time t is defined as

$$\lambda_R(t) = \lambda_{R0} + \lambda_{R1} \exp(-t/\tau), \qquad \textbf{4.1}$$

where parameters λ_{R0}, λ_{R1}, and τ are the offset, amplitude and time constant respectively. The best-fitted values of λ_{R0}, λ_{R1}, and τ are summarized in Table 4.2. It to be noted that the time constant for equation 4.1 is found as ~19.3 days, which shows that the island films are very much unstable even at the room temperature. The product of λ_{R1} and τ is defined as an aging constant which also has a physical significance. Larger the aging constant more is the stability of the film. Similar exponential decay shift in LSPR peak position is also observed by P Jain et al. during the study of inter-particle gap dependent plasmon coupling. However, decay constant is defined in terms of an inter-particle gap [34]. Here, it can be easily co-related that during aging inter-particle gap is increasing due to aging assist-dewetting. The experimentally obtained data of β_R and A_R for 3.9 nm thick Au film are also plotted in

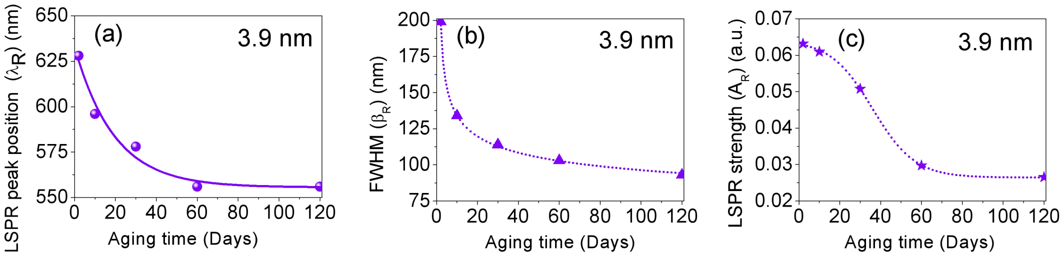

Figure 4.7 Variation in (a) peak position, (b) full width at half maxima (FWHM), and (c) strength of plasmonic response of 3.9 nm thickness Au film with aging time. (solid line corresponds to fitted data and dotted lines are guided for eyes) (set-B).

Figures 4.7(b)-4.7(c) to describe the aging effect (the continuous line is guide for the eyes).

TABLE 4.2: The best-fitted function and its parametric values for variation in localized surface plasmon resonance (LSPR) peak position with aging time (set-B).

Function	Parameter	Value (unit)	Standard error (unit)	Adj. R-Square
Single exponential decay function	λ_{R0}	555.6 nm	5.6 nm	0.953
	λ_{R1}	77.5 nm	8.6 nm	
	τ	19.34 Days	6.02 Days	

It is imperative to note that at an early stage of aging (<20 days), the value of the β_R (Figure 4.7(b)) decreases more steeply as compared to λ_R (Figure 4.7(a)). It indicates that changes in particle shapes are more sensitive than the particle sizes for aging. In the early stage of aging, the strength of LSPR reduces slowly, after that the variation attains its maximum followed by a further slow modification. Moreover, it can be seen that at 120 days of aging time, the variation in λ_R and A_R seems to be saturated while β_R still shows a noticeable decrement. Similar to Figure 4.6(a), H Sun et al. showed the blue shift in LSPR peak position with a reduction in its FWHM and strength on annealing at a constant temperature, as a result of drastic morphological self-organization [31], [36], [37].

The visual inspection of aging effect is also performed by capturing the photographic image of Au thin film samples. Figures 4.8(a)-4.8(b) display the color photographic images of as-deposited and aged (120 days) Au thin films of different thicknesses (set-B). Some of the samples shown in the photographs are not included in the present study. The color of 3.9 nm thick as-deposited film is light blue which is the typical color of coalescing island Au films (Figure 4.8(a)) [36], [38]. This light blue

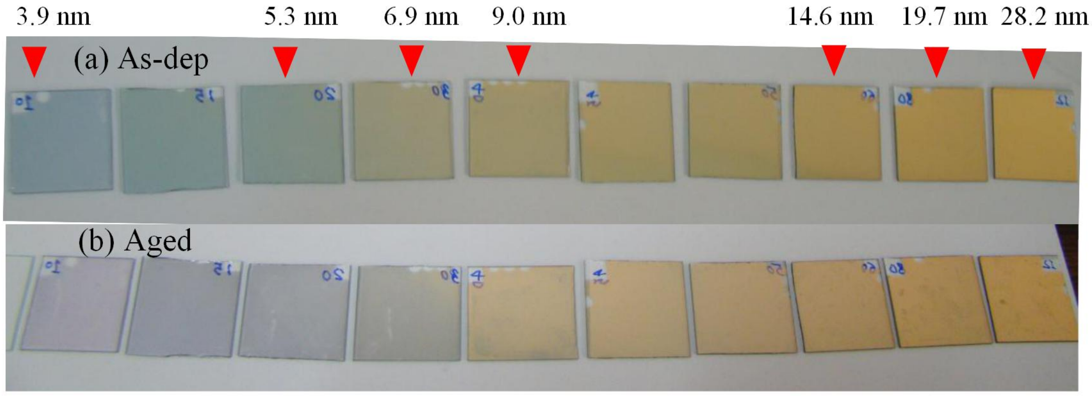

Figure 4.8 Photographic image showing color variation in (a) as-deposited and (b) aged (120 days) Au thin films of different thickness grown on a glass substrate (set-B).

color becomes cyan color along with slight mixing of golden color as the thickness of the Au film increased up to 5.3 nm. At the stage of 6.9 nm thickness golden color intensity increased incomparably. The color of Au thin film becomes almost golden for 9.0 nm thickness film, which is the signature of continuous Au film. The intensity of golden color increases very slowly as the thickness of the Au film further increases. After aging, the color of all the films having thickness <9.0 nm affected significantly. The light blue color of 3.9 nm thick as-deposited Au film becomes purple after aging (Figure 4.8(b)). The cyan color (5.3 nm thick film) become blues purple after aging. In the case of 6.9 nm thick film, golden color become blues golden after aging. However, it is difficult to see the color variation in the films having thickness ≥9.0 nm with naked eyes, while in the absorbance spectra significant changes are observed. It is reported earlier that as-deposited Au thin films of different thicknesses show considerable color variation because of the existence of varying morphology for different film thickness. All the color for different Au films thickness also changes due to annealing assist variation in the morphology [36]. The present experiment of aging shows similar variation as in annealing process.

4.5 Schematic of morphological evaluation in nanostructured Au films on ambient aging

The variation in plasmonic response of Au thin film deposited on glass substrate can be explain by evolution occurred in the morphology on ambient aging. It is well known that Au films are rarely oxidize in ambient environment and optical responses of nanostructured Au films are highly sensitive to variation in its morphology. Figure 4.9 shows the schematic of morphological evolution in island, percolated and continuous films with aging time. The densely packed platelet shaped islands transformed into dome shape islands. This reshaping leads to increment of vertical height and decrement into lateral diameter ($h_2 > h_1$ and $d_2 < d_1$). Moreover, inter-island separation increases and contact area (interface area) between island and substrate reduces ($g_2 > g_1$ and $A_2 < A_1$). The reduction in lateral size and increment into inter-particle spacing leads to the blue shift in LSPR peak position as described in section

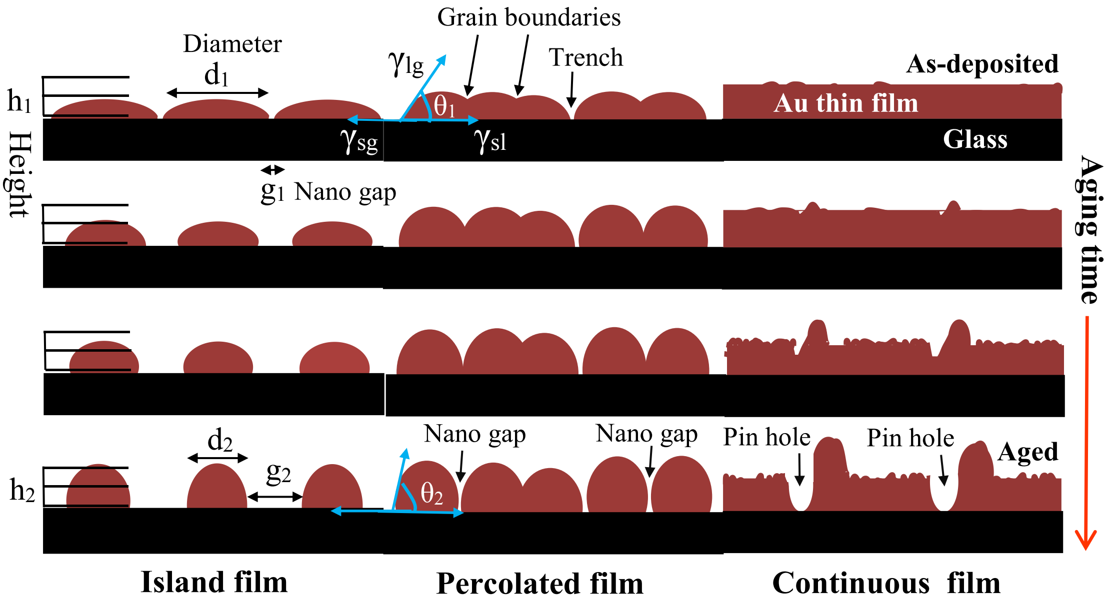

Figure 4.9 Schematic of morphological evolution in island, percolated and continuous Au thin films with aging time.

4.4. The reduction in interface area also support the blue shift in LSPR peak position . The aging assisted reshaping enhances the sphericity of the islands which leads to reduction in FWHM of LSPR peak. In the percolated Au film, closely attached grains separates from grain boundaries and form dumbbell shape, ginger shape and more complicated geometries in Au thin film morphology. The large variation in particle sizes and shapes occurred in the Au thin film after aging results in a broad LSPR response. The continuous Au film also transformed into a holed and hummock type film after aging. The formation of pin holes in the continuous Au thin film leads to the excitation of new absorption band in the visible wavelength range. These pin holes can also support the collective oscillation of free electron and shows dipole and higher order pole charge distribution depending upon the hole size and shape. The increased number density as well as size of pin holes increases the absorbance with aging time. Some other facts like average thickness and roughness increment of the thin film due to accumulation of hummocks near the pin holes along with the enhancement in the porosity and the reduction in average mass density of the film also occurred. All the morphological transformation are the consequences of minimization of total energy. The detailed information about the associated energies with the Au thin films are given later in section 4.6.

4.6 Morphological characterization as-deposited and aged Au films

The optical response of ultra-thin Au films is dependent on its physical parameters as explained by the model given in previous section. In order to verify the model of morphological evaluation and quantify the variation in the thickness, roughness and the average density of the Au film on aging, x-ray reflectivity (XRR) is performed.

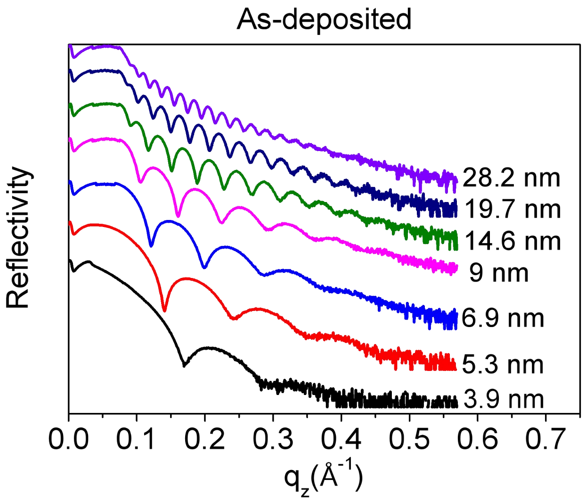

Figure 4.10 Experimental XRR pattern (reflected counts as a function of normal component of the x-ray wave vector, q_z) of as-deposited Au thin films of different thickness deposited on glass substrate at 20 mA sputtering current (set-B).

Figure 4.10 represents the variation in experimentally recorded XRR spectra of as-deposited Au thin films of different thickness which is corresponding to different deposition time at 20 mA sputtering current (set-B). XRR spectra are presented in pair for quantification of variation in physical parameters. The measured XRR data of as-deposited and aged Au films is fitted with Parratt recursive formalism [39]. The measured and fitted XRR spectra of 3.9, 5.3, 6.9 and 9.0 nm thickness as-deposited and aged (120 days) Au thin films are shown in Figures 4.11(a)-4.11(d) respectively [40]. The XRR spectra of 3.9 nm thick as-deposited Au film represents well defined Keissing oscillations which damped completely along with a drastic reduction in critical angle (θ_c) on aging (Figure 4.11(a)). The Keissing oscillations are also damped in the case of 5.3 nm thick Au film similar to 3.9 nm thick Au film but the oscillations do not fully disappears. It shows the presence of some extremely weak oscillations in the XRR spectra after aging (Figure 4.11(b)). The damping in Keissing oscillations and shifting of critical angle also occur in 6.9 nm thickness Au

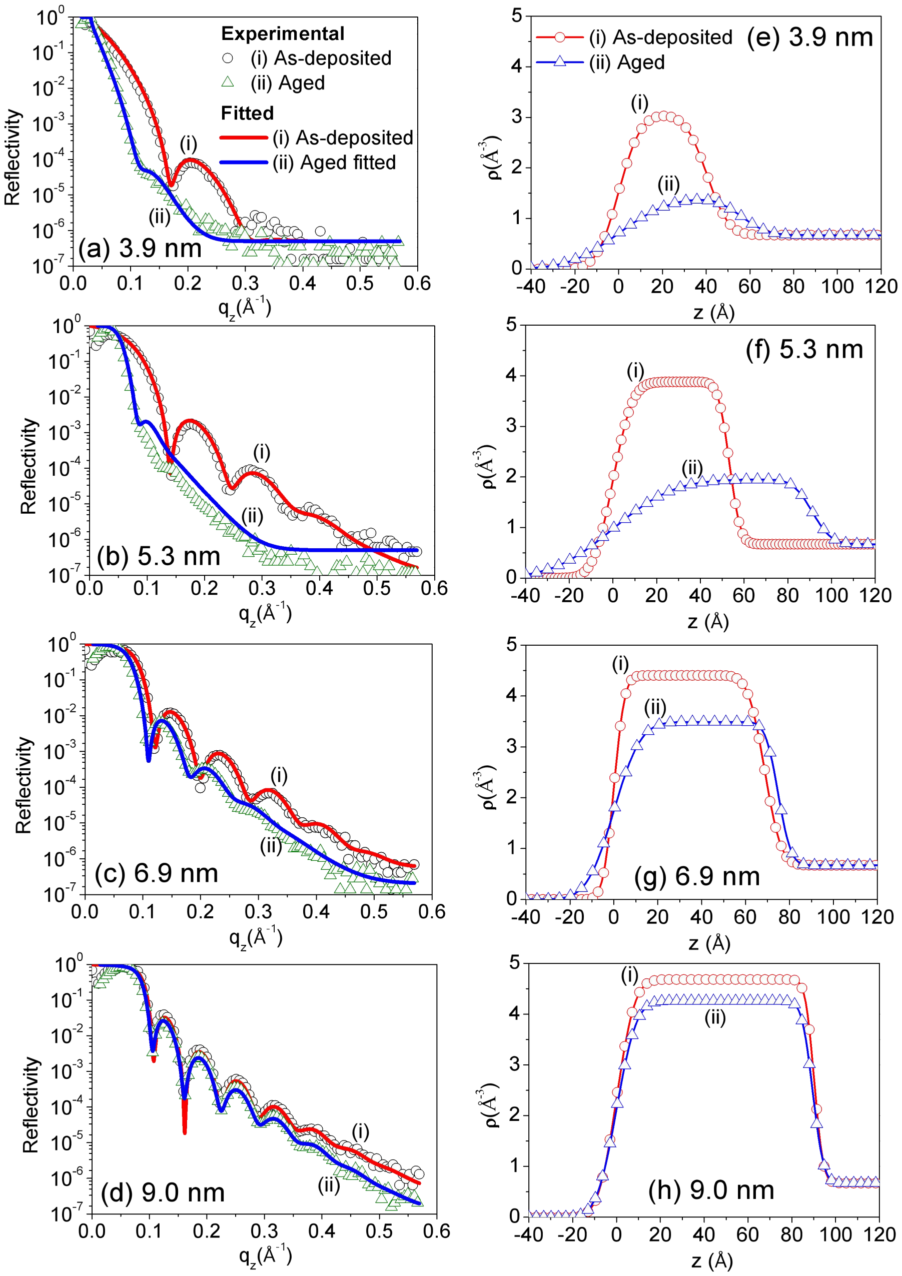

Figure 4.11 Experimental (bubble) and fitted (solid line) XRR pattern (reflected counts as a function of normal component of the x-ray wave vector, q_Z) of as-deposited and aged (120 days) Au thin films of different thickness (a) 3.9 nm, (b) 5.3 nm, (c) 6.9 nm, and (d) 9 nm. The electron density profile (EDP) obtained from best fitted XRR pattern for as-deposited and aged films (e) 3.9 nm, (f) 5.3 nm, (g) 6.9 nm, and (h) 9 nm (set-B).

films but seems less effective (Figure 4.11(c)). For 9.0 nm thick Au film, overlapping in XRR spectra of as-deposited and aged films is found except some difference in the decay rate of the reflectivity profile at higher q_z (>0.3) (Figure 4.11(d)). The damping in the Keissing oscillations in the XRR spectra is the consequence of reduced specular reflection and enhanced diffuse scattering, which clearly indicates the drastic increment in the roughness of the Au film after aging (Table 4.3) [41], [42]. The reduced critical angle (θ_c) could be contributed by the decrement in the average material density or enhanced porosity [42]. The above effects such as an increment in roughness and reduction in average material density are quite expected for an increased average thickness Au films (a constant amount of Au material present on the glass). It is noted that no loss of the amount of Au material is occurring at room temperature during the aging process. Furthermore, all the theoretically generated XRR spectra have good matching with the experimentally obtained XRR data, which allows the evaluation of the thickness, roughness, and the average density as well as average in-plane (x-y) electron density profile (EDP) as a function of depth (z) of the Au films [43].

TABLE 4.3: Variation in thickness, roughness and an average density of the as-deposited and aged Au thin films deposited for 10, 20, 30 and 40 s time by a sputtering technique (set-B).

Thickness (t) (Å)			Roughness (R) (Å)			Average density (ρ) (g/cm^3)		
As-deposited t_1	Aged t_2	$\Delta t = t_2 - t_1$	As-deposited R_1	Aged R_2	$\Delta R = R_2 - R_1$	As-deposited ρ_1	Aged ρ_2	$\Delta\rho = \rho_1 - \rho_2$
39.50	56.13	16.63	10.01	18.92	8.91	13.33	6.10	7.23
53.27	91.17	37.9	7.05	31.42	24.37	16.92	10.47	6.47
68.67	74.47	5.80	3.93	8.63	4.71	19.52	15.23	4.29
90.23	90.6	0.37	6.55	7.35	0.80	20.42	18.58	1.84

The thickness, roughness and the material density of as-deposited and aged Au thin films determined from the model used for generation of the best theoretical simulation are listed in Table 4.3. It is found that thickness and roughness increases and average material density decrease for all the film after aging. It is worthy to note that variation of thickness and roughness are found maximum for 5.3 nm thick film while the variation of average material density between as-deposited and aged Au thin film is monotonically reduces as the thickness increases (Table 4.3). Furthermore, the average in-plane (x-y) EDP as a function of depth (z) for as-deposited and aged Au thin films are plotted in Figures 4.11(e)-4.11(h) (obtained from the best fit of XRR spectra). The suppression of amplitude, expansion of broadening and enlargement of rounding in edges of EDP curves for aged films are also clearly interpreted by increased thickness and roughness along with a reduction in the average material density (Figures 4.11(e)-4.11(h)). The pre-existing rounding in the EDP edge in 3.9 and 5.3 nm thick films lead to the conclusion that as-deposited Au layers are island and semicontinuous (percolated) type respectively that becomes fully discontinuous after aging having different sizes and shapes of the particles [44]. The as-deposited 6.9 nm thick Au films also show a rounding in EDP edge, which corresponds to almost continuous film while aged film depicts significant signature of edge rounding. However, it still seems continuous (middle part of EDP is constant) except the presence of few holes in the Au thin film as concluded from the optical response. Finally, in the case of 9 nm thickness, both as-deposited and aged films show almost overlapping in the EDP broadening while ~7 % change in the density is calculated. Furthermore, all the XRR analysis revealed the thickness and roughness increment, as well as mass-density decrement, caused a change in the morphology of Au thin film during aging which ultimately plays a key role in the variations in the optical response.

All the above findings of XRR spectra and obtained EDP provide necessary and sufficiently strong evidence of morphological evolution in Au thin films during aging that thoroughly explains the transformation in its optical responses. However, three of the Au thin films are also studied by AFM in order to visualize the morphological changes in Au thin films with aging. Figure 4.12 represents the two dimensional AFM images of the as-deposited and aged Au film of 3.9, 5.3, and 6.9 nm thickness (set-B) along with corresponding line scans (cross-section view). It depicts that initial morphology of all the three as-deposited films is no longer sustain and experienced a drastic morphological evolution with aging time. The AFM images of all as-deposited Au thin films show faint morphologies that seem to be a nearly continuous film (Figures 4.12(a-1), 4.12(b-1) and 4.12(c-1)). It may be due to the limited spatial

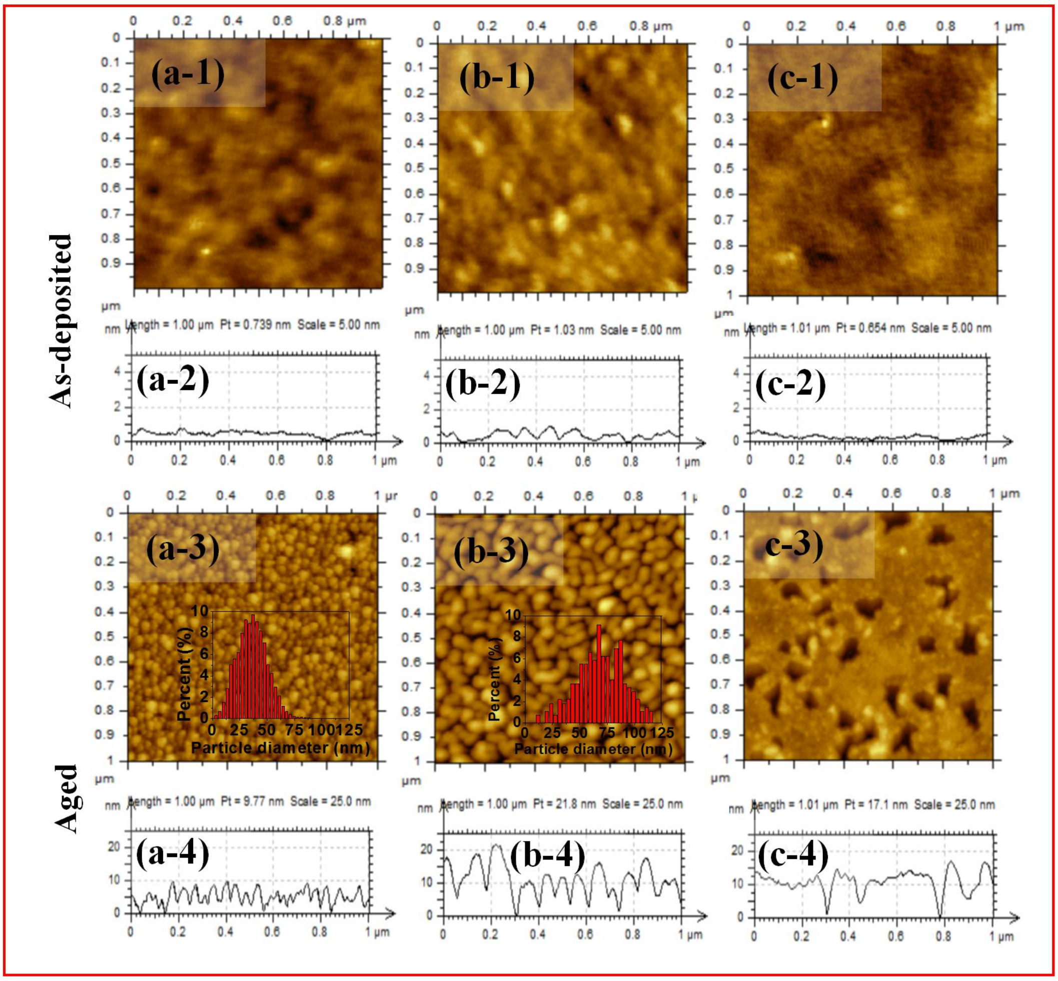

Figure 4.12 Atomic force microscope image and line profile (cross-section view) of as-deposited and aged Au thin film of different thickness (a-1)-(a-4) 3.9 nm, (b-1)-(b-4) 5.3 nm, and (c-1)-(c-4) 6.9 nm. (Images size 1 μm by 1 μm) (set-B). Inset shows the plotted histograms.

resolution of AFM technique (convolution of tip diameter), which cannot discriminate between the closely separated particles as well as voids present in the percolated structures. Even the height variations in the addressed morphologies are also very less (Figures 4.12(a-2), 4.12(b-2) and 4.12(c-2)). This strengthen the XRR observations that as-deposited Au thin films had much less roughness and showed well defined Keissing oscillations. However, broad peaks at ~650, and ~775 nm in the absorbance spectra of 3.9 nm and 5.3 nm thickness films along with their bluish color in the photograph images suggests the presence of densely packed larger size particles and percolated structure respectively[30], [33], [35]. In contrast to the as-deposited Au thin films, the presence of the high number density of Au nanoparticles as well as percolated structures can be realized in aged samples. Figure 4.12(a-3) shows the highly dense assembly of discrete circular particles (closely separated islands) present in 3.9 nm thick aged film. The average lateral size of the particles is 38 nm ±13 nm along with ~8 nm average vertical height (Figures 4.12(a-3)-4.12(a-4) and inset of Figures 4.12(a-3)). The 5.3 nm aged Au film shows bigger and highly compact assembly of coalescing islands (interconnected particles) having lateral average particle size 68 nm ±22 nm along with vertical height ~15 nm (Figures 4.12(b-3)-4.12(b-4) and inset of Figures 4.12(b-3)). The average lateral size of the particles is obtained from histogram using Scanning Probe Image Processor (SPIP) software and the average height obtained from the corresponding line scans. Figure 4.12(c-3) shows that the aged Au film of 6.9 nm thickness is semi-continuous having irregularly shaped voids (black portion) and hills (bright yellow) while no such features are present in the corresponding as-deposited film (Figure 4.12(c-1)). The number of voids present in $1\mu m \times 1\mu m$ is ~30 (void density), having average size ~95 nm, which uncover the ~11.4% area of the film. The corresponding line scan depicts that maximum depth of the voids and height of the hills with respect to the flat surface are ~10 nm and ~5 nm respectively. The formation of voids and ridges can be explained by the dewetting process in which Au atoms migrate from bottom to top [45]. The laddered atoms of Au also roost nearby each void to form island/rim on the edge of voids followed by material conservation law [46]. These grown-up voids and islands ultimately decrease the average film density and increase the average height and roughness in the aged Au thin film. Exactly similar type of voids formations in a protruding process is identified in microstructure analysis of pure metallic (Ag, Pt) and alloy (Au-Pt, Cu-Ni) thin films during annealing [47], [48]. These findings are very much similar to the reduction in the critical angle (film porosity) and the fast decay of fringe pattern of XRR spectra in the aged film. The 9 nm thick Au film is fully continuous, even then some evolution of roughness occurred during aging, which is depicted in corresponding optical response as well as obtained EDP in XRR measurement. This also justifies the reshaping or densification phenomenon of the islands at room temperature. In this process, the vertical height of the islands increases with a decrease in the lateral size, which leads to an increased inter-particle gap and reduced covered area fraction. The modified dimensions of islands (increased height and reduced width) as well as increased nearest-neighbor inter-particle spacing provide a measurable condition for AFM [49]. The AFM is a complementary technique to the XRR. XRR gives good results for a smooth film while AFM works efficiently for rough films. Moreover, in this particular case, the limitations of both the techniques can also be treated as a result to explain the dewetting process in the Au thin films. The combination of XRR and AFM illustrated the morphological transformation in the Au thin films with high accuracy, which is responsible for the variation in the optical response during ambient aging.

The XRR and AFM provide the morphological information. The GIXRD is accomplished to find one of the physical aspects of the morphological transformations occurring in Au thin films during room temperature aging. The experimentally measured and fitted data of GIXRD pattern of as-deposited and aged Au thin films are shown in Figures 4.13(a)-4.13(b) respectively. The XRD spectra represent the single-phase poly-crystalline nature of Au in both as-deposited and aged thin films. The existence of peaks at q_z values of 2.7, 3.1, 4.4 and 5.2 Å^{-1} are easily indexed with (111), (200), (220) and (311) planes of face-centered cubic (fcc) crystal of Au. The variation in FWHM of XRD peaks ((111) and (311) planes) for as-deposited and aged Au thin film samples are plotted in Figures 4.13(c)-4.13(d). The consistent decrement in the FWHM of XRD peaks ((111) and (311) planes) with film thickness is found for as-deposited Au thin films, whereas, consistence increment

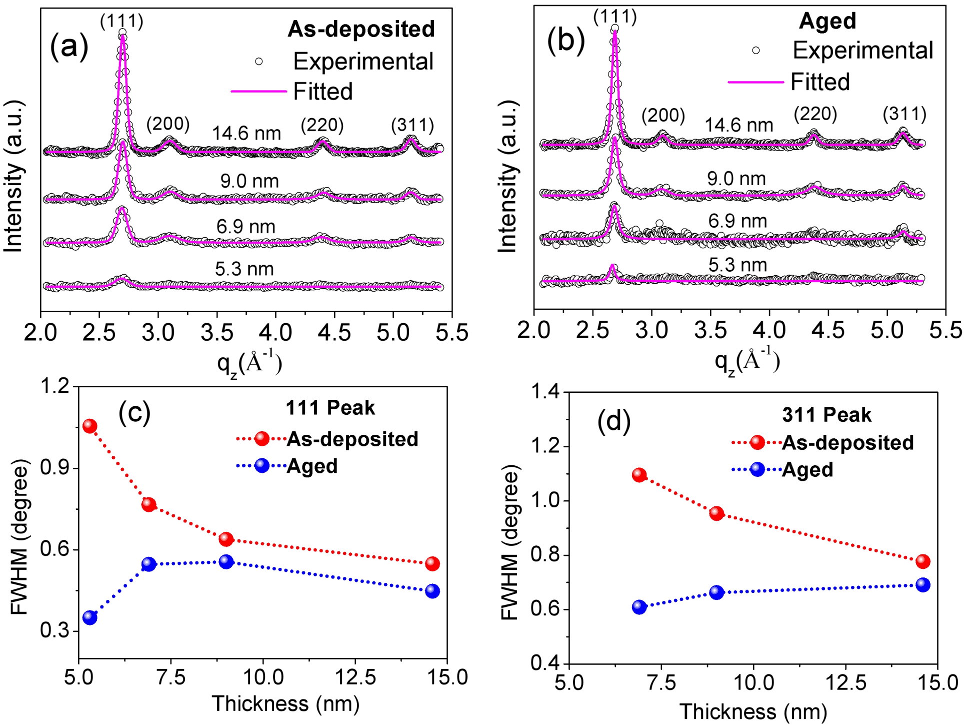

Figure 4.13 Experimental (black bubble) and fitted (pink solid line) x-ray diffraction (XRD) pattern of (a) as-deposited and (b) aged Au thin films of different thickness. The variation in full width at half maxima (FWHM) of XRD peaks of (c) (111) and (d) (311) planes with Au film thickness for as-deposited (red) and aged (blue) films (set-B).

found for aged Au films. It is concluded that the reduction in FWHM of XRD peak is found for both the planes for each Au thin film thickness. However, reduction in the FWHM of XRD peak is thickness dependent. The lowest thickness Au films (5.3 nm in Figure 4.13(c) and 6.9 nm in Figure 4.13(d)) show a maximum reduction in FWHM of XRD peak after aging. The above results are the consequence of grain size enlargement during aging due to total energy minimization via crystallization process at environmental exposure. It is well known that at room temperature growth of polycrystalline metal film consist of large defects density (vacancies), twines and preferential orientation (texture) in the crystal structure, which generates the strain in the lattice planes that make the film thermally unstable. This strain triggers the changes in the crystallinity as well as morphology such that films start recovery of strain just after the growth. The recovery of strain occurs fast in lower thickness films, and eventually, stress reduces and reaches the plateau region. The variation in strain and crystallinity ultimately leads to the variation in FWHM of peaks in the XRD spectra. Recently C. Garozzo et al. also showed the morphological and structural evolution of Au nanodots at room temperature aging using transmission electron microscopy imaging and electron diffraction [50]. It is also reported that even as-deposited amorphous films of Cu_2S grown by sputtering shows polycrystalline nature after aging (room temperature) due to crystallization process and also shows consistent variation in optical transmission and reflection [51].

As discussed earlier in the proposed model that morphological variation (dewetting) occurred in the all type (island, percolated and continuous) of Au films at ambient environmental. In subsequent section proposed modal is experimentally validated by XRR and AFM techniques. GIXRD reveals that crystallization also co-exist with the dewetting of Au thin film at room temperature. Both the above processes (dewetting and crystallization) are extensively studied at high temperature annealing. In which it is described that island, percolated and continuous films are thermodynamically unstable. In this view, it is expected that at room temperature (environmental ambiance) also these films are not stable. At room temperature diffusion coefficient for Au thin films is not zero, therefore there is finite probability to have such variations at room temperature for minimization of total energy associated with the film. Hence, the similar analogy can be applied for the explanation of dewetting and crystallization of Au thin films at environmental ambiance. For a single phase poly-crystalline film total energy (E_t) can be written as

$$E_t = E_s + E_i + E_{GB} + E_\varepsilon \qquad \textbf{4.2}$$

where E_s, E_i, E_{GB}, and E_ε are surface energy, interface energy, grain boundary energy, and strain energy. In the island film, most of the individual islands are single crystals or have few number of grain boundaries or triple junctions but can have vacancies or other defects. Therefore, it is expected that grain boundary energy has very less contribution in evolution process for island films. Due to large surface and interface area associated surface and interfaces energies are dominating. In the case of percolated films, partial coalesce occurs in the nearest neighbor island during film growth which leads to the grain boundary formation. Therefore, in the percolated and continuous films all four energies have significant contribution in the room temperature evolution of morphology. Figure 4.9 shows the equilibrium position of percolated Au nanostructure at glass substrate. In thermodynamic equilibrium condition Au nanostructure system can be define by the following equation

$$\gamma_{sg}=\gamma_{sl}\cos(\theta)+\gamma_{lg} \qquad \mathbf{4.3}$$

The γ_{sg}, γ_{sl} and γ_{lg} are the interfacial energies between solid-gas, solid-layer and layer-gas phases and θ is the contact angle which decides wetting and non-wetting nature of the material. For non-wetting substrate $\gamma_{sg}<\gamma_{sl}+\gamma_{lg}$ or $\theta>0$. The large/small values of θ corresponds to partial/full material surface coverage respectively even for a constant Au thin film thickness. Due to non-wetting nature of Au nanostructure, the contact angle increases during aging therefore vertical dimension of the Au nanostructure increases and lateral dimension reduces via dewetting. The dewetting also leads to shrinking or breaking the weakly connected islands in the percolated structures and form a clear cut LSPR peak in the absorbance spectra after aging. This process is very much similar to the annealing at higher temperatures as discussed in chapter 3.

4.7 Application of nanostructured Au thin film as a SERS substrate

In order to use the nanostructured Au thin film for SERS application, SERS spectra of R6G dye drop coated on the aged Au thin films recorded. Figure 4.14 show the

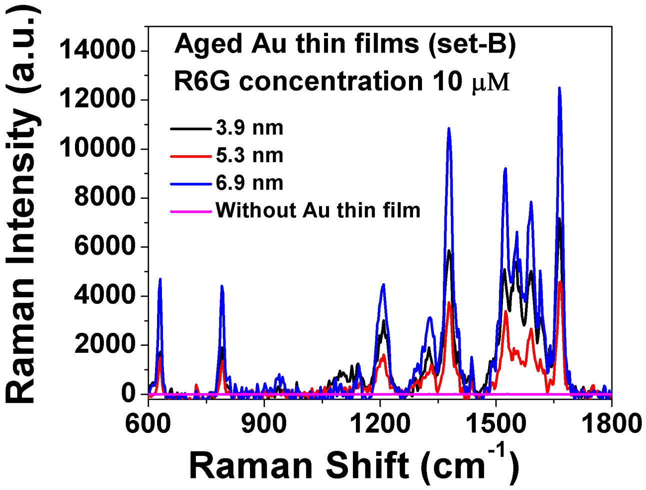

Figure 4.14 SERS spectra of drop coated R6G having concentration of 10 μM on aged Au thin films of various morphologies.

recorded Raman spectra for the R6G dye (10 μM) drop coated on the 3.9 nm, 5.3 nm and 6.9 nm thick aged films. It is found that all the characteristic Raman peak show maximum enhancement for 6.9 nm thick aged film. The 6.9 nm thick Au film is also used for detection of lower concentration of R6G dye. 1 μM concentration of R6G shows significant Raman signal. As demonstrated earlier in the absorbance spectra that voids presents in the Au films also show the LSPR excitation similar to the nanoparticles. The maximum enhancement in the Raman signal is due to the existence of relatively higher intensity in the hot spot exist in the voids as well as associated nearest hummocks structures. The exact calculation of field intensity in voids films and their comparison to island and percolated films is the topic of future research.

4.8 Conclusions

Gold (Au) thin films of 1.4 nm to 28.2 nm thickness have been fabricated on glass substrate, and the experimental evidence of huge transformations in its plasmonic responses are demonstrated for short and prolonged ambient aging. The as-deposited Au island films show a blue shift in localized surface plasmon resonance (LSPR) peak position along with a reduction in its broadening and strength after aging. The as-deposited percolated films display the clear-cut transformation of broadened spectra into a sharp LSPR peak after aging. The dynamical model based on variation in LSPR peak position with aging have also been established for island type Au film. The transformations in the plasmonic response of island, percolated, and continuous Au films are correlated with aging-induced morphological changes, which are governed by the room temperature solid-state dewetting as well as crystallization processes. The solid-state dewetting and crystallization are monitored by x-ray reflectivity, atomic force microscopy and grazing-incidence x-ray diffraction techniques and reliably described and correlated. It is concluded that optical, morphological and crystallographic transformations in the Au thin films are strongly dependent on the thickness as well as on aging time. The kinetics of the aging process is found very much similar to the annealing process except its rate. Finally, aged film are used for the SERS application and its found that Au thin films having voids show large SERS intensity for drop coated R6G dye in comparison to the thin film having island and percolated type Au structures.

References:

[1] P. Pavaskar, I. K. Hsu, J. Theiss, W. H. Hung, and S. B. Cronin, "A microscopic study of strongly plasmonic Au and Ag island thin films," vol. 113, no. 34302, pp. 1–6, 2013.

[2] C. Chen *et al.*, "Nanoporous gold films prepared by sputtering- dealloying combination for total internal reflection SERS measurement," *Opt. Mater. Express*, vol. 6, no. 5, pp. 1561–1569, 2016.

[3] L. E. Kreno, J. T. Hupp, and R. P. Van Duyne, "Metal-organic framework thin film for enhanced localized surface Plasmon resonance gas sensing," *Anal. Chem.*, vol. 82, no. 19, pp. 8042–8046, 2010.

[4] E. Stratakis and E. Kymakis, "Nanoparticle-based plasmonic organic photovoltaic devices," *Mater. Today*, vol. 16, no. 4, pp. 133–146, 2013.

[5] A. M. Michaels, Jiang, and L. Brus, "Ag nanocrystal junctions as the site for surface-enhanced Raman scattering of single rhodamine 6G molecules," *J. Phys. Chem. B*, vol. 104, no. 50, pp. 11965–11971, 2000.

[6] G. Kalyuzhny, A. Vaskevich, G. Ashkenasy, A. Shanzer, and I. Rubinstein, "UV/Vis spectroscopy of metalloporphyrin and metallophthalocyanine monolayers self-assembled on ultrathin gold films," *J. Phys. Chem. B*, vol. 104, no. 34, pp. 8238–8244, 2000.

[7] W. Bai *et al.*, "Design of plasmonic back structures for efficiency enhancement of thin-film amorphous Si solar cells," *Opt. Lett.*, vol. 34, no. 23, pp. 3725–3727, 2009.

[8] E. Thouti, N. Chander, V. Dutta, and V. K. Komarala, "Optical properties of Ag nanoparticle layers deposited on silicon substrates," *J. Opt.*, vol. 15, no. 35005, pp. 1–7, 2013.

[9] G. F. Bohren and D. R. Huffman, *Absorption and Scattering of Light by Small Particles*. New York: Wiley, 1983.

[10] U. Kreibig and M. Vollmer, *Optical properties of metal clusters*. Berlin: Springer, 1995.

[11] L. Yan, Y. Yan, L. Xu, R. Ma, F. Jiang, and X. Xu, “Large range localized surface plasmon resonance of Ag nanoparticles films dependent of surface morphology,” *Appl. Surf. Sci.*, vol. 367, pp. 563–568, 2016.

[12] S. Verma *et al.*, “Surface plasmon resonances of Ag-Au alloy nanoparticle films grown by sequential pulsed laser deposition at different compositions and temperatures,” *J. Appl. Phys.*, vol. 117, no. 133105, pp. 1–11, 2015.

[13] X. Liu *et al.*, “Tunable dipole surface plasmon resonances of silver nanoparticles by cladding dielectric layers,” *Sci. Rep.*, vol. 5:12555, pp. 1–7, 2015.

[14] H. Hieber, “Aging properties of gold layers with different adhesion layers,” *Thin Solid Films*, vol. 37, pp. 335–343, 1976.

[15] M. Pattabi *et al.*, “Aging studies on discontinuous silver films in ultrahigh vacuum,” *Thin Solid Films*, vol. 322, pp. 340–343, 1998.

[16] X. Chen *et al.*, “Effect of aging on optical properties of bimetallic sensor chips,” *Opt. Express*, vol. 18, no. 2, pp. 1105–1112, 2010.

[17] R. Sachan *et al.*, “Oxidation-resistant silver nanostructures for ultrastable plasmonic applications,” *Adv. Mater.*, vol. 25, pp. 2045–2050, 2013.

[18] T. Kawaguchi and S. Maruno, “Change in optical transmission spectra of Ag discontinuous films due to aging,” *Jpn. J. Appl. Phys*, vol. 35, no. 10, pp. 5485–5486, 1996.

[19] Z. M. Qi, S. Xia, and H. Zou, “Slow spontaneous transformation of the morphology of ultrathin gold films characterized by localized surface plasmon resonance spectroscopy,” *Nanotechnology*, vol. 20, no. 255702, pp. 1–5, 2009.

[20] H. Shirakawa and H. Komiyama, “Migration-coalescence of nanoparticles during deposition of Au, Ag, Cu, and GaAs on amorphous SiO2,” *J. Nanoparticle Res.*, vol. 1, pp. 17–30, 1999.

[21] C. Gatel and E. Snoeck, “Comparative study of Pt, Au and Ag growth on Fe3O4 (0 0 1) surface,” *Surf. Sci.*, vol. 600, pp. 2650–2662, 2006.

[22] L. Zhang, F. Cosandey, R. Persaud, and T. E. Madey, “Initial growth and morphology of thin Au films on TiO2(110),” *Surf. Sci.*, vol. 439, pp. 73–85, 1999.

[23] A. Reznickova, Z. Novotna, N. S. Kasalkova, and V. Svorcik, “Gold nanoparticles deposited on glass: Physicochemical characterization and cytocompatibility,” *Nanoscale Res. Lett.*, vol. 8:252, pp. 1–8, 2013.

[24] A. Merlen, V. Gadenne, J. Romann, V. Chevallier, L. Patrone, and J. C.

Valmalette, “Surface enhanced Raman spectroscopy of organic molecules deposited on gold sputtered substrates,” *Nanotechnology*, vol. 20, no. 215705, pp. 1–7, 2009.

[25] Sudheer, P. Mondal, V. N. Rai, and A. K. Srivastava, “A study of growth and thermal dewetting behavior of ultra-thin gold films using transmission electron microscopy,” *AIP Adv.*, vol. 7, no. 75303, pp. 1–13, 2017.

[26] V. N. Rai, A. K. Srivastava, C. Mukherjee, and S. K. Deb, “Surface enhanced absorption and transmission from dye coated gold nanoparticles in thin films,” *Appl. Opt.*, vol. 51, no. 14, pp. 2606–2615, 2012.

[27] A. Herz *et al.*, “Solid-state dewetting of single- and bilayer Au-W thin films: Unraveling the role of individual layer thickness, stacking sequence and oxidation on morphology evolution,” *AIP Adv.*, vol. 6, no. 35109, pp. 1–10, 2016.

[28] S. Verma, B. Tirumala Rao, S. Rai, V. Ganesan, and L. M. Kukreja, “Influence of process parameters on surface plasmon resonance characteristics of densely packed gold nanoparticle films grown by pulsed laser deposition,” *Appl. Surf. Sci.*, vol. 258, pp. 4898–4905, 2012.

[29] B. Balamurugan and T. Maruyama, “Evidence of an enhanced interband absorption in Au nanoparticles: Size-dependent electronic structure and optical properties,” *Appl. Phys. Lett.*, vol. 87, no. 143105, pp. 1–3, 2005.

[30] A. B. Tesler *et al.*, “Tunable localized plasmon transducers prepared by thermal dewetting of percolated evaporated gold films,” *J. Phys. Chem. C*, vol. 115, pp. 24642–24652, 2011.

[31] H. Sun, M. Yu, X. Sun, G. Wang, and J. Lian, “Ultrathin gold island films for time-dependent temperature sensing,” *J. Nanoparticle Res.*, vol. 16:2273, pp. 1–8, 2014.

[32] S. Verma, B. T. Rao, S. Bhartiya, V. Sathe, and L. M. Kukreja, “Growth temperature dependent surface plasmon resonances of densely packed gold nanoparticles’ films and their role in surface enhanced Raman scattering of Rhodamine6G,” *Appl. Surf. Sci.*, vol. 346, pp. 379–387, 2015.

[33] Y. Gong *et al.*, “Systemically tuning the surface plasmon resonance of high-density silver nanoparticle films,” *Eur. Phys. J. D*, vol. 67: 87, pp. 1–6, 2013.

[34] P. K. Jain, W. Huang, and M. A. El-Sayed, “On the universal scaling behavior of the distance decay of plasmon coupling in metal nanoparticle pairs: A plasmon ruler equation,” *Nano Lett.*, vol. 7, no. 7, pp. 2080–2088, 2007.

[35] A. B. Tesler, B. M. Maoz, Y. Feldman, A. Vaskevich, and I. Rubinstein, “Solid-state thermal dewetting of just-percolated gold films evaporated on glass: Development of the morphology and optical properties,” *J. Phys. Chem. C*, vol. 117, p. 11337−11346, 2013.

[36] H. Sun, M. Yu, G. Wang, X. Sun, and J. Lian, “Temperature-dependent morphology evolution and surface plasmon absorption of ultrathin gold island

films," *J. Phys. Chem.C,* vol. 116, p. 9000−9008,*C*, 2012.

[37] H. Sun, M. Yu, X. Sun, G. Wang, and J. Lian, "Effective temperature sensing by irreversible morphology evolution of ultrathin gold island films," *J. Phys. Chem. C*, vol. 117, pp. 3366–3373, 2013.

[38] C. Worsch, M. Kracker, W. Wisniewski, and C. Rüssel, "Optical properties of self assembled oriented island evolution of ultra-thin gold layers," *Thin Solid Films*, vol. 520, no. 15, pp. 4941–4946, 2012.

[39] L. G. Parratt and C. F. Hempstead, "Anomalous dispersion and scattering of X-rays," *Phys. Rev.*, vol. 94, no. 6, pp. 1593–1600, 1954.

[40] I. Stabrawa *et al.*, "Investigation of gold nanolayer properties using X-ray reflectometry and spectroscopic ellipsometry methods," in *Acta Physica Polonica A*, 2016, vol. 129, no. 2, pp. 233–236.

[41] H. You, R. P. Chiarello, H. K. Kim, and K. Q. Vandervoort, "X-ray reflectivity and scanning-tunneling-microscope study of kinetic roughening of sputter-deposited gold films during growth," *Phys. Rev. Lett.*, vol. 70, no. 19, pp. 2900–2903, 1993.

[42] K. Leosson, A. S. Ingason, B. Agnarsson, A. Kossoy, S. Olafsson, and M. C. Gather, "Ultra-thin gold films on transparent polymers," *Nanophotonics*, vol. 2(1), pp. 3–11, 2013.

[43] M. Schwartzkopf *et al.*, "Real-time monitoring of morphology and optical properties during sputter deposition for tailoring metal-polymer interfaces," *ACS Appl. Mater. Interfaces*, vol. 7, pp. 13547–13556, 2015.

[44] S. Kundu *et al.*, "Morphology of thin silver film grown by dc sputtering on Si(001)," *J. Phys. D Appl. Phys*, vol. 31, no. 98, pp. L73–L77, 1998.

[45] C. V. Thompson, "Solid-state dewetting of thin films," *Annu. Rev. Mater. Res.*, vol. 42, pp. 399–434, 2012.

[46] C. M. Müller and R. Spolenak, "Microstructure evolution during dewetting in thin Au films," *Acta Mater.*, vol. 58, pp. 6035–6045, 2010.

[47] H. Krishna, R. Sachan, J. Strader, C. Favazza, M. Khenner, and R. Kalyanaraman, "Thickness-dependent spontaneous dewetting morphology of ultrathin Ag films," *Nanotechnology*, vol. 21, no. 155601, pp. 1–7, 2010.

[48] P. Pandey, M. Sui, Q. Zhang, M. Y. Li, S. Kunwar, and J. Lee, "Systematic control of the size, density and configuration of Pt nanostructures on sapphire (0 0 0 1) by the variation of deposition amount and dwelling time," *Appl. Surf. Sci.*, vol. 368, pp. 198–207, 2016.

[49] D. Lee *et al.*, "Observation of shape, configuration, and density of Au nanoparticles on various GaAs surfaces via deposition amount, annealing temperature, and dwelling time," *Nanoscale Res. Lett.*, vol. 10:2040, pp. 1–14, 2015.

[50] C. Garozzo, A. Filetti, C. Bongiorno, A. La Magna, F. Simone, and R. A.

Puglisi, “Room temperature evolution of gold nanodots deposited on silicon,” *Gold Bull.*, vol. 47, pp. 185–193, 2014.

[51] H. A. Alburaih and A. El-Denglawey, “Aging effect on the structure and optical properties of nano Cu2S films,” *Results Phys.*, vol. 7, pp. 1010–1015, 2017.

Chapter 5

Fabrication of plasmonic nanoparticle grating structures and its application for SERS substrate

5.1 Introduction

Plasmonic periodic structures like nanoparticle gratings, periodic array of holes, triangular shape islands and voids have shown many exciting and conspicuous applications like signal propagation in sub-wavelength waveguide, light trapping in solar cell, circumventing the sub-diffraction limited imaging, enhanced optical diffraction efficiency [1],[2] and surface-enhanced Raman spectroscopy (SERS) based chemical and biological sensor [3],[4]. In SERS application, electromagnetic field enhancement occurs on metallic nanostructured surfaces [5], and this supports in increasing the weak Raman signal of Raman-active chemo and bio-entities placed over the surfaces of metallic structures by many orders of magnitude [6]–[8]. The periodic structures have been fabricated using different techniques like electron beam evaporation, holography [9]–[11], electron beam lithography (EBL) [12], nano-sphere lithography [13], inert gas aggregation [3], soft nano-imprint lithography [14],[15] and a combination of soft and nanosphere lithography [4], etc. These periodic structures are prepared on different substrates like quartz [3], float glass [12], silica [13], Si wafer [14], and on the flexible polymer substrates like polydimethylsiloxane (PDMS)

[4] and polyethylene terephthalate (PET) [15]. These substrates offer better reproducibility, uniformity along with durability [4],[14]. This kind of substrate also finds application in the field of chemical micro-sensor using SERS technique [16], [17]. Most of the methods mentioned above are difficult and time taking in preparing a periodic structure. However, there is also a quest for finding an alternative technique which is easy, fast and suitable for large area fabrication with high reproducibility at low-cost of production for periodic structures for such practical applications.

The present chapter is focused on the alternative technique and suitable substrate for the fabrication of plasmonic nanoparticle grating (PNG) structures. The EBL technique is suitable in producing different types of structures by varying its operating parameters. Apart from the lithography technique, a suitable substrate to secure architecture of the PNG structures also plays a vital role. Here, a single step fabrication of the PNG structure by the EBL using conventional SEM on the commercially available silver halide (AgBr) film which is generally used in high-resolution transmission electron microscope (TEM) imaging is descried. The silver (Ag) nanoparticle gratings of the different period are made by varying the number of lines per frame in raster scanning of the electron beam at a constant exposure. The morphological characterization of fabricated gratings is performed by LM, SEM and AFM techniques. The elemental mapping of AgBr based film (bare substrate) as well as fabricated PNG structure are performed by EDS technique. The crystallographic characterization of the fabricated grating is performed by XRD technique. The LSPR response of the fabricated grating is analyzed by recording the absorption spectra. Finally, the fabricated PNG structures are tested as a SERS substrate for the Rodamine6G (R6G) dye. The SERS enhancement factors achieved using Ag PNG substrate is also compared with the similar type of sputtered grown Ag thin film substrates.

5.2 Characterization of silver halide based film

The AgBr based electron microscopy film has been used as a substrate for the electron beam writing to fabricate the PNG structures. The Figure 5.1(a), shows the top side flat view of the commercially available AgBr based microscope film (Kodak-4489). The standard size of the film available is 100 mm × 80 mm. The AgBr based film is specially engineered for high-resolution microscopic imaging. It consists of four layers as shown schematically in Figure 5.1(b) [18]. The base of the film is made of polyethylene terephthalate (PET) of thickness ~278 µm [19]. One side of the PET is coated with ultra-fine AgBr grains which are randomly suspended in the gelatin matrix (binder) called an emulsion.

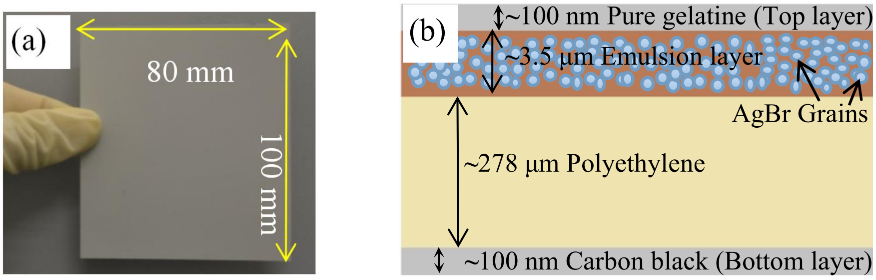

Figure 5.1 (a) Image of silver halide (AgBr) based film (top side view) and (b) schematic of the cross-sectional view of unexposed AgBr film (substrate).

These AgBr grains are sensitive to the electron beam exposure. The emulsion layer ~3.5 µm thick is coated with scratch proof gelatin layer of ~100 nm from top. The back side of the PET (bottom layer) is coated with black carbon particles, which reduces the backscattering of electrons during the exposure and helps to improve the quality of fabrication during EBL process.

A cross-sectional sample was prepared for finding the emulsion thickness of the bare substrate (Kodak-4489 film) and the shape, size and the arrangement of embedded AgBr grains inside the emulsion. The sample is prepared by sticking two bare substrates face to face as shown in the schematic (Figure 5.2(a)). Figure 5.2(b) shows the cross sectional SEM image of the bare substrate. The emulsion layer has thickness of ~3.5 µm. Figure 5.2(c) shows a magnified view of the small portion of the emulsion having platelet shape AgBr grains (crystals) randomly embedded (homogeneously) in the whole volume of the emulsion. The average thickness and the lateral dimension of the pebbles shape AgBr grains are found as ~120 nm and ~450 nm respectively.

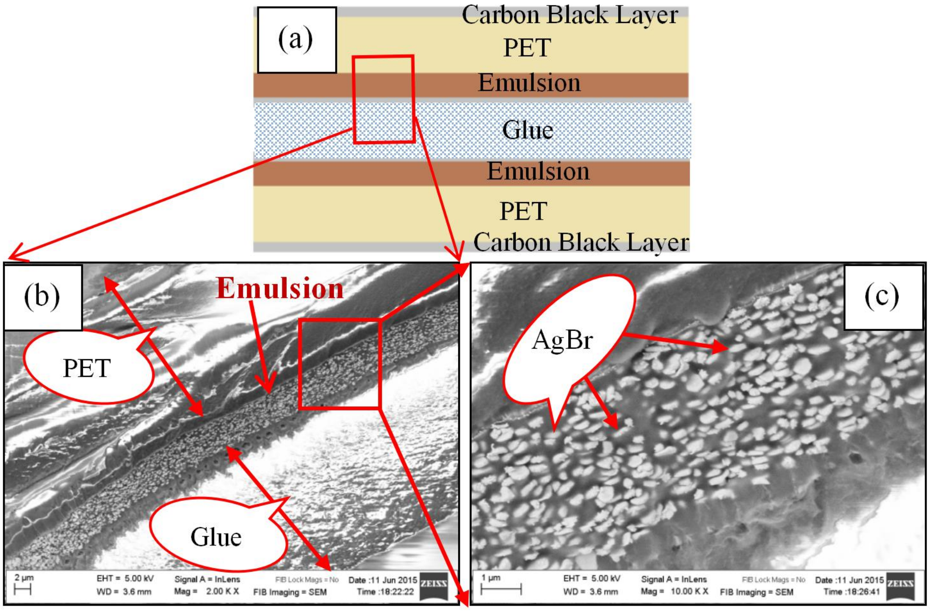

Figure 5.2 (a) Schematic of the cross-sectional view of unexposed silver halide (AgBr) film (bare substrate), (b) lower and (c) higher magnification cross-section SEM images of AgBr based film.

The crystalline phase and grain size of AgBr (present in the substrate) is determine by analyzing the x-ray diffraction spectra (XRD) at 18 keV energy (λ = 0.6689 Å) with synchrotrons radiation source on ADXRD beam line-11 (BL-11) of INDUS-2 in transmission mode. Image plate area detector is used to obtain diffraction pattern. XRD spectra shows various peaks in the pattern corresponding to different planes of

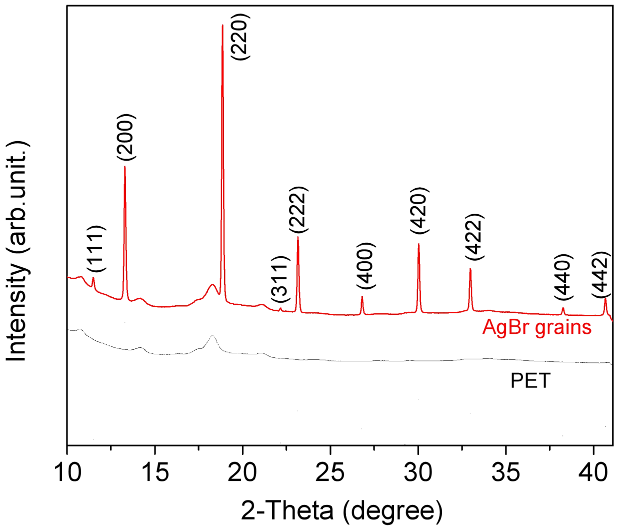

Figure 5.3 XRD pattern of silver halide (AgBr) grains embedded in the emulation of microscope film and base material PET.

AgBr crystal. The ten peaks at 11.49°, 13.29°, 18.87°, 22.17°, 23.15°, 26.81°, 30.03°, 32.97°, 38.25° and 40.67° in the XRD spectra are corresponding to the reflection from (111), (200), (220), (311), (222), (400), (420) (422), (440) and (442) planes of the face-centered cubic crystal phase of AgBr [20], [21] (JCPDF file no 6-438) [22].

5.3 Fabrication of plasmonic grating structures

The conventional SEM is used for the electron beam lithography for the fabrication of PNG structures. The Figure 5.4 (a) shows the raster scan process of the electron beam on the substrate. During raster scan, electrons interact with the sample in tear-shaped volume. Figure 5.4 (b) shows the schematic of two different interaction volume at 5 keV and 30 keV in the specimen. The SE, BSE, x-rays, and photons come from the different depths of the interaction volume which also differs in diameter according to the energies of the primary electrons (typically between 200 eV and 30 keV).

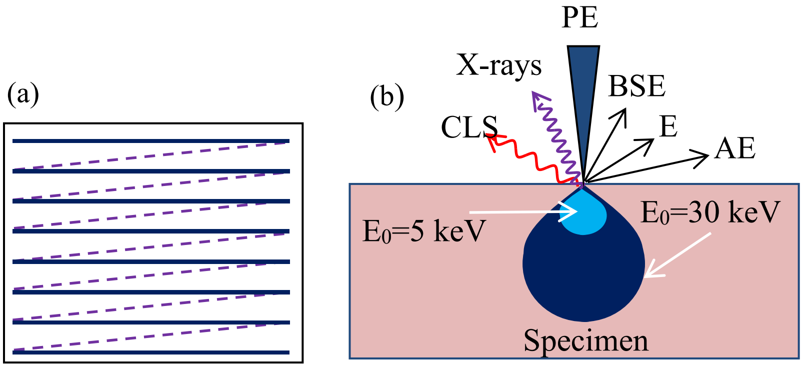

Figure 5.4 (a) Schematic of raster scan process and (b) primary electron intersection volume in the specimen along with produced electrons, x-rays, and photons.

The electron beam writing process is carried out using the conventional SEM. The raster scan of the SEM is used for the fabrication of PNG structures. The complete fabrication process is described in the Figure 5.5. A piece of film is mounted on the SEM stage. The focused electron beam is used to expose the AgBr grains embedded in the emulsion of the substrate from the top side in raster scan fashion (line by line scanning). The exposed films were developed and fixed by the standard chemical processing technique optimized for Kodak 4489 microscope film [23]. The developer solution is made by dissolving standard Kodak DA-163 (part-A 29 gm and part-B

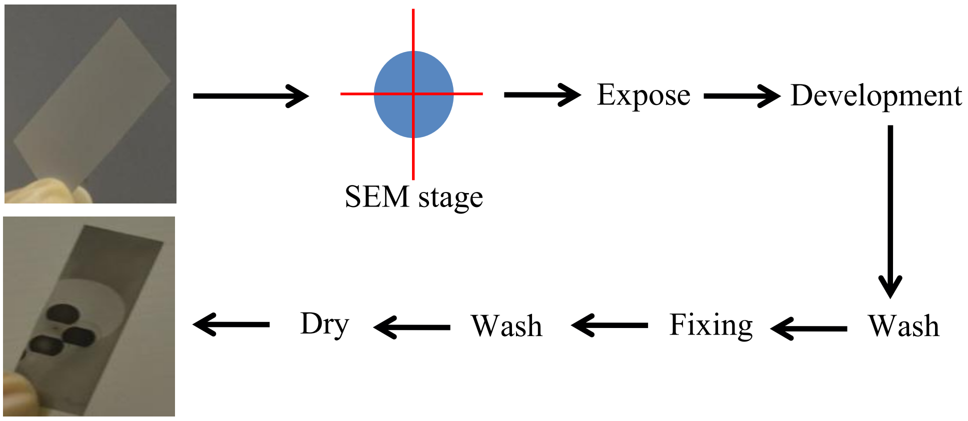

Figure 5.5 Route for fabrication of PNG structure using raster scan for conventional SEM.

235 gm) powder in 9 liters of water. The fixer solution is made by dissolving 10 gm sodium thiosulphate crystals in 80 ml water. The development process converts the exposed AgBr grains into Ag nanoparticles whereas the fixing process removes the unexposed AgBr grains and unexposed gelatin. The exposed portion of the film contains Ag particles and gelatin after development and fixing process. The Ag particles are embedded in the gelatin which protect the Ag particles from environmental degradation. Finally, it provides a surface relief plasmonic nanoparticle gratings. The AgBr film is exposed at three different places for fabrication of grating structure (Figure 5.5), which appear as black disk type spots in processed film (after development and fixing). It was also noted that only region (equal to the stub area) in the processed film was found to be transparent. While it was expected that whole film should be transparent except the three exposure areas. The exposure of the film other than the regions exposed by the e-beam is due to charge accumulated on the film. As discussed earlier PET is the base material of the film and is an insulator polymer. The film area which is in contact with the conducting SEM stub could easily conduct charge to the ground. In order to provide conducting path to the electrons an aluminum holder is fabricated which allows large conducting area on the plate film. This helps in achieving the large area for the fabrication of PNG structure. Figures 5.6(a)-5.6(c) show the schematic of the

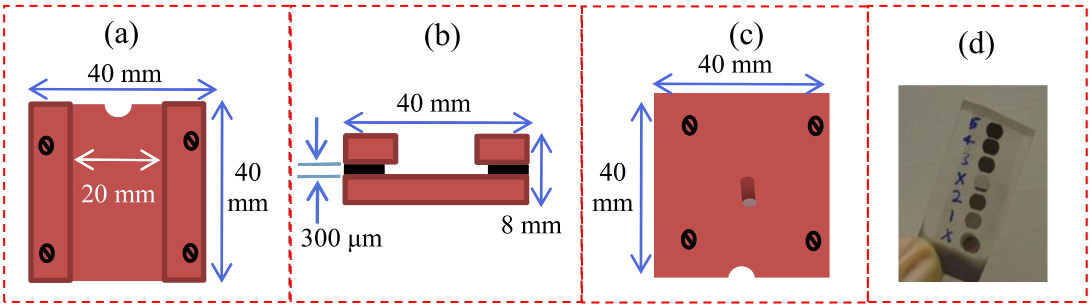

Figure 5.6 Schematic of aluminum holder (a) top side view, (b) cross-sectional view, and (c) back side view. (d) Photographic images of processed substrate with aluminum holder

aluminum holder fabricated for holding the AgBr based film. The length and width are decided by the stage movement of the SEM. A gap ~300 µm is kept between the top plate and bottom plate of the holder for holding the film. The gap is decided by the thickness of the AgBr film (Figure 5.1(b)). Finally, prepared holder offers a 40 mm × 20 mm area for the electron beam exposure. It is noted that whole process has to be performed in the dark room or in the presence of red light. Hence a notch is made in the bottom plate of the aluminum holder to make the insertion process of the film easier. On the back side of the holder a pin is also welded in the center of the aluminum plate which helps in the placement of the holder on the SEM stage. When mounting of sample into SEM stage is carried out using this holder, the stage (0,0) position ensures that the holder center is below the beam. Figure 5.6(d) represents the photographic images of processed sample using aluminum holder. It can be seen that charging problem is significantly reduced. Exposure can be done in a selected area by fixing the coordinate on a rectangular area. Multiple exposure is possible over an increased area of a larger rectangular stub designed specially for the fabrication purpose.

The typical parameters of SEM instruments used for the fabrication of PNG structures are accelerating voltage, beam current, dwell time, spots size, magnification, line per frame and working distance. The accelerating voltage is changed to increase the depth of interaction volume which ultimately decides the height of the fabricated PNG structures. The beam current and the dwell time determines the dose received by the specimen. The spot size selects the width of the single exposure line in the PNG structures. The lines per frame at a fixed magnification and working distance controlled the period of the PNG structures. Finally, the magnification and the working distance decide the fabricated area. In the present work, two sets of PNG structures were fabricated. In set-A, the film was exposed by a 30 keV electron beam with a beam size of ~15 nm in the raster scan mode. For the fabrication of PNG structures of the different periodicities and thicknesses single raster scans were used. These scans with different lines per frame e.g., 484, 968, 1452, and 1936 having dwell time of ~40 ms at 20× magnification were used for the fabrication. The maximum area exposed in the film at 20× magnification was 4 mm in diameter [24]. The time required to expose 4 mm diameter area can be estimated by the number of lines per frame and the dwell time. In the present case, the time taken for exposure of 484, 968, 1452, and 1936 lines per frame is estimated as 19, 38, 58, and 77 s, respectively. In set-B, the exposure energies of the electron beam were 5, 10, 15, and 30 keV with 10, 20, 31, and 63 μA beam current, respectively, providing four different gratings. However, rest of the parameters of the beam like 484 lines per frame, beam size ~50 nm, and 240 ms dwell time, were kept same for all samples. Exposure was carried out at 10.5 mm working distance for 20× magnification to provide a ~ 4 mm diameter exposed area on the substrate for both the sets. The total exposure time to expose ~ 4 mm diameter was ~116 s corresponding to 484 lines per frame and 240 ms dwell time. In both the sets, the exposed films were developed as discussed earlier in this section.

5.4 Morphological characterization of PNG structures

A aluminum holder is used to fabricated the PNG structure in a large area. The aluminum holder offers a 40 mm by 20 mm area for fabrication. The Figure 5.1(a) shows the photographic image of the PNG structures fabricated on AgBr based TEM film using the aluminum holder. A 3×6 matrix of the grating structures was written on the 40 mm × 20 mm size film (Figure 5.7(a)). The area of each grating structure

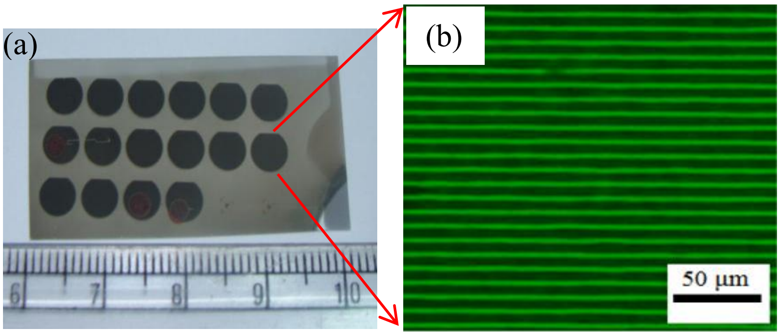

Figure 5.7 (a) Photographic image of the PNG structures fabricated on the silver halide (AgBr) based electron microscope film, (b) magnified LM image showing the grating structure present in the exposed area.

written on the film is ~12.5 mm^2. The total fabricated area on the film is ~200 mm^2. Figure 5.7(b) shows the magnified LM image of one of the fabricated regions in the matrix revealing the grating structure formed on these areas. Each exposed area in the matrix contains grating structure with different periodicity.

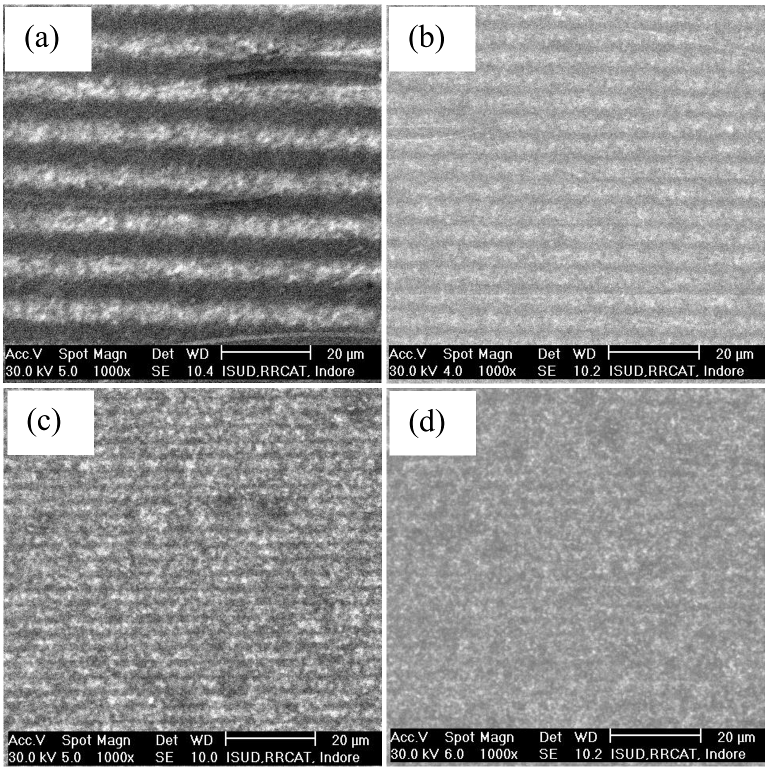

Figure 5.8 The SEM image of the PNG structures fabricated by the electron beam raster of (a) 484, (b) 968, (c) 1452 and (d) 1936 lines per frame.

TABLE 5.1: Variation in the silver (Ag) coverage area with the change in the grating period.

Lines per frame	Grating period W_G (μm)	Exposed region W_{ER} (μm)	Unexposed region W_{UER} (μm)	W_{ER}/W_{UER}	$(W_{ER}/W_G) \times 100$ (% Volume fraction)
484	10	5.82	4.18	1.39	58.2
968	5	3.35	1.65	2.03	67
1452	3.4	2.85	0.55	5.18	83.8
1936	2.5	-	-	-	>95

All the periodic structures were written and developed in similar conditions. The SEM images of the PNG structures fabricated using raster scan of 484, 968, 1452, and 1936 lines per frame are shown in Figures 5.8(a)-5.8(d) respectively. These SEM images confirm the presence of one-dimensional grating structures. The PNG structures with a period of 10, 5, 3.4, and 2.5 μm corresponds to the raster scan of 484, 968, 1452, and 1936 lines per frame respectively. These scan rates are standard scan rates provided by the manufacturer of the microscope, as described in chapter 2. The periodicity of the PNG structures is calculated by taking the line scan of the images by using the image analysis software ImageJ. The intensity plot is generated by integrating the fixed area in all the micrographs of different lines per frame.

The quantitative analysis of SEM images of the PNG structures are performed in terms of Ag coverage area fraction and shown in Table 5.1. The Table 5.1 shows that as the lines per frame increases, the exposed area (Ag coverage) increases. Particularly, in the case of 1936 lines per frame corresponding to 2.5 μm period grating nearly entire area is exposed, and very feeble periodic structure is observed (Figure 5.8(d)).

The high-resolution FESEM images of the PNG structure (2.5 μm) and the randomly distributed Ag nanoparticles grown by sputtering for 60 s and 240 s on the virgin PET substrate were recorded at 100000X magnification and are shown in Figures 5.9(a)-5.9(c). The high-resolution image of PNG structure at 100000X magnification is not very clear because of the charging effect (Figure 5.9(a)). But still, it is possible to find an approximate value of particle size as ~22 nm. Figures 5.9(b)-5.9(c) show that the Ag nanoparticle density is less as well as the particle size is small in 60 s sputtered thin film compared to 240 s sputtered film. The size of the Ag nanoparticles in 60 and 240 s sputtered thin films are found as ~16 nm and ~20 nm respectively. The morphology of nanoparticles in the PNG structure and the sputtered thin films are nearly same.

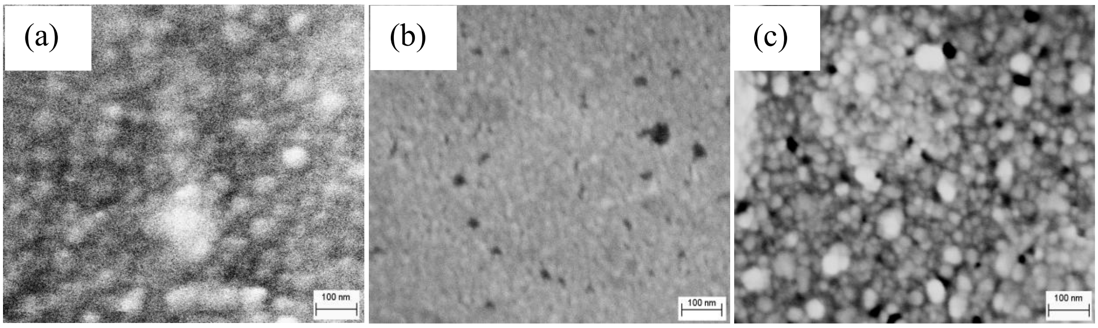

Figure 5.9 The high-resolution FESEM images of (a) the PNG structure having 1936 lines per frame, sputtered grown thin films of Ag for (b) 60 s, and (c) 240 s.

Figures 5.10(a)-5.10(d) shows AFM images of the PNG gratings of 10, 5, 3.4, and 2.5 μm periods. The line scan of AFM images are obtained for confirmation of the periodicity of the grating as well as to find the depth of the structure (Figures 5.10(e)-5.10(h)). Here, periods of the gratings with 484, 968, 1452, and 1936 lines per frame

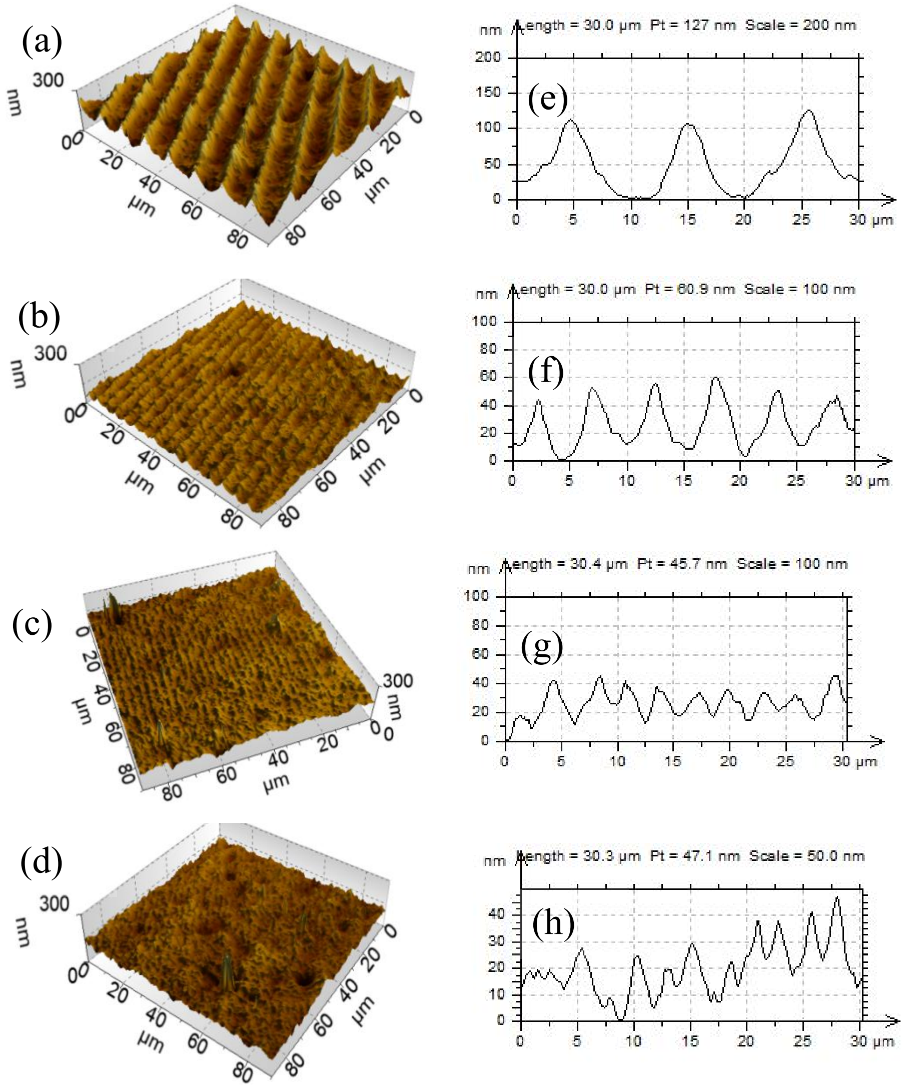

Figure 5.10 The AFM image and line scan of the PNG structures fabricated by the electron beam lithography, (a,e) 484, (b,f) 968, (c,g) 1452, and (d,h) 1936 lines per frame respectively.

scans are estimated to be 10, 5, 3.4, and 2.5 µm respectively. These are in agreement with the values obtained from the SEM. However, the depth of the grating structure decreases as the number of lines per frame is increased.

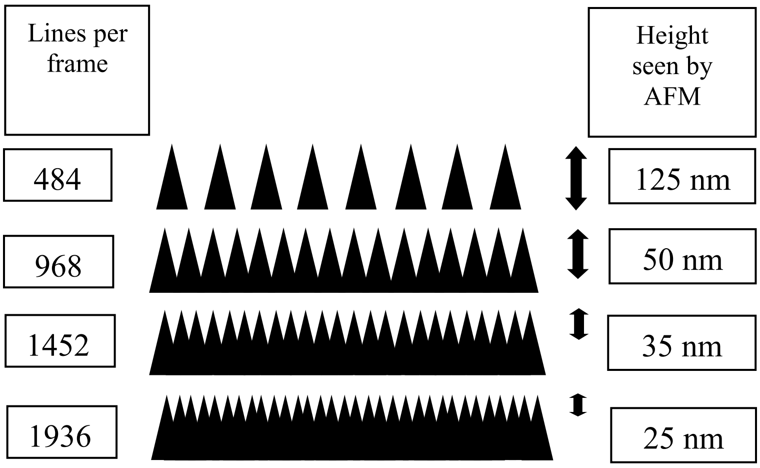

Figure 5.11 Schematic diagram showing a variation of depth of PNG structures with an increase in the number of lines per frame.

The variation in the thickness of the PNG structures along with a change in lines per frame scan is shown schematically in Figure 5.11. This is attributed to an increase in the interaction volume of the electron beam inside the AgBr emulsion with an increase in the number of lines per frame. The exposed AgBr width is found much broader than the actual electron beam size. The calculated electron beam spread in the AgBr based film using Monte Carlo simulation [25] is found as ~4-5 μm [26]. The height of the grating structure decreases or the thickness of the bottom layer increases with a reduction of the grating period due to overlapping of the beam from the adjacent lines during the scan as shown in Figure 5.11.

The EDS analysis of the film was carried out to confirm the presence of Ag after the development process of the exposed film. Figure 5.12(a) the shows EDS spectra of the unexposed and the undeveloped AgBr based electron microscope film, which reveals the presence of both Ag and Br elements. The copper peaks are due to the conducting coating deposited on the film to avoid the charging effect during the EDS measurement. The EDS spectrum of the fabricated grating structure after development process shows the presence of only Ag (Figure 5.12(b)). The elemental

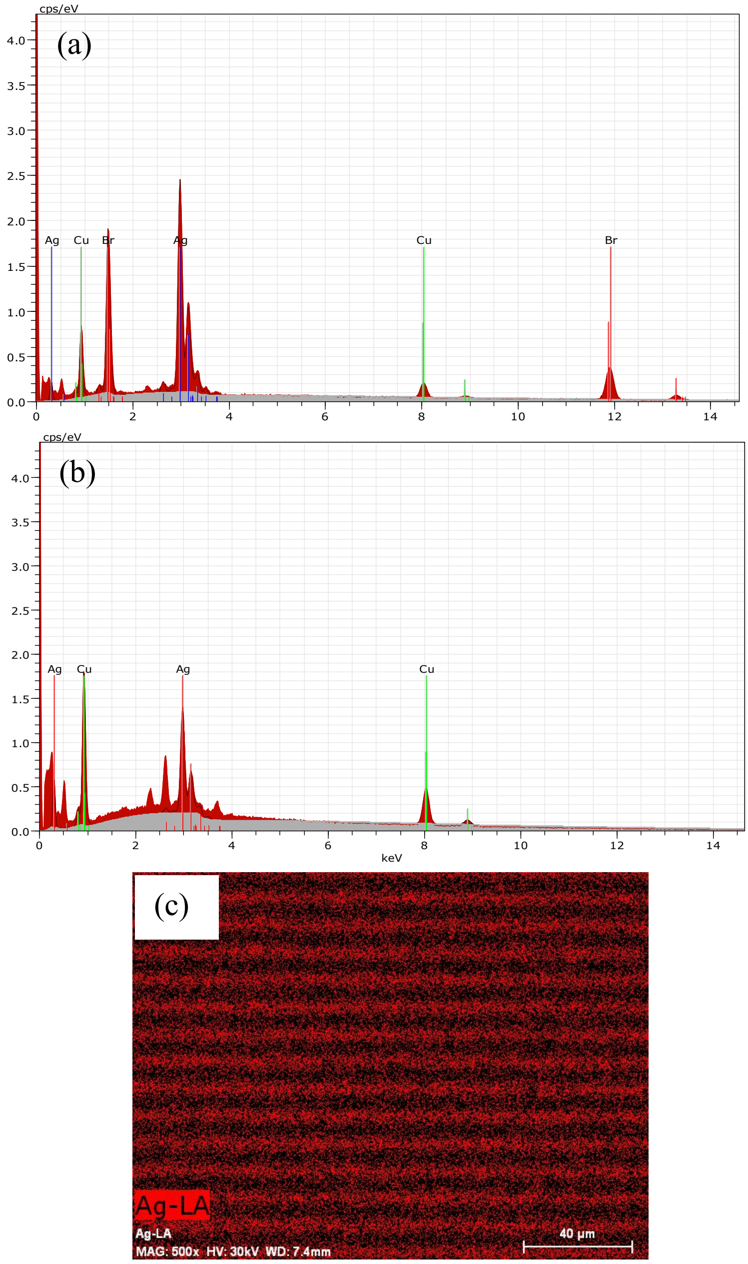

Figure 5.12 (a) EDS spectra of the unexposed and undeveloped silver halide (AgBr) based electron microscope film, (b) EDS spectra of the exposed and developed film, and (c) elemental mapping showing the presence of the silver (Ag) in the form of periodic structure (10μm).

mapping of the fabricated grating structure also indicates the presence of ordered structure of Ag (Figure 5.12(c)).

5.5 XRD Characterization

XRD pattern of fabricated PNG structures are recorded in transmission mode with PET base substrate using image plate area detector (MAR 345). The wavelength and the sample to detector distance were accurately calibrated using LaB_6 NIST standard. It known from the AFM images that thickness of the fabricated PNG structures are very much less (<120 nm) compare to thickness of base material PET (~273 µm).

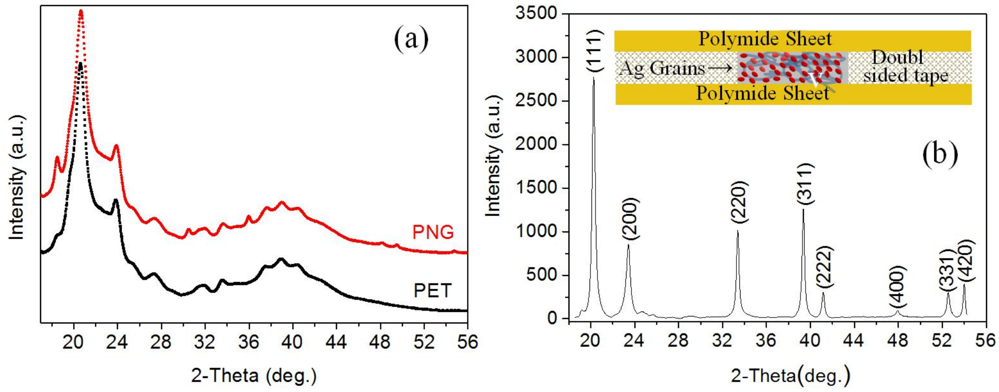

Figure 5.13 XRD spectra of the (a) silver nanoparticles present in the PNG structure and bare PET (b) silver nanoparticle.

In this case XRD spectra of PET dominates over the Ag nanoparticles of PNG structures. The intensity of peak Ag grains are very less and some of the peaks do not appear as shown in Figure 5.13(a). This type of XRD spectra are complicated to analyze and no clear conclusion obtained about the size of Ag grains embedded in the fabricated PNG structure. New samples are made by scratching Ag particles from the PET substrate. The scratched Ag particles are sandwiched between the polyamide sheets (kapton sheets) making a 5 mm hole in the double-sided tape as shown in inset of Figure 5.13(b). The polyamide sheet is considered as transparent for the 0.8282 Å (~16keV) x-rays. In this type of sample Ag nanoparticles are embedded in the gelatin matrix with a random orientation. XRD pattern of nanoparticles appears equal to the powder diffraction pattern of LaB6. The crystallographic characterization of PNG grating is performed by the synchrotrons radiation source with 16keV energy. Figure 5.13(b) shows the XRD spectra of the Ag nanoparticle embedded in the fabricated PNG structure. The background subtracted XRD pattern of the Ag nanoparticles shows eight different peaks located at 20.27°, 23.41°, 33.38°, 39.34°, 41.15°, 47.92°, 52.54°, and 53.97°corresponding to the reflection from (111), (200), (220), (311), (222), (400), (311), and (420) planes of the face-centered cubic (fcc) Ag. The XRD pattern is indexed with the JCPDS (file no-40783). The experimentally calculated value of the lattice constant for Ag is a=0.4083 nm, which is in good agreement with the reported value a=0.4086nm [27]. This diffraction pattern is used for the calculation of the average particle size (L) of the Ag nanoparticles using Scherrer formula given as

$$L = \frac{0.96\lambda}{\beta \cos\theta} \qquad \textbf{5.1}$$

where λ is the wavelength (λ=0.8282Å) of the incident x-ray, β is the FWHM of the peaks at 2θ value. The calculated average crystallite size of the Ag nanoparticle is found as 18 ±2 nm, which is in good agreement with the FESEM results.

5.6 Optical Characterization

The optical properties of the PNG gratings have been studied by UV-Vis spectroscopy to obtain information about the LSPR response, which describes the collective excitation of conduction band electrons in the metal. Figure 5.14 shows the absorption spectra of the PNG structures fabricated on PET as well as of the virgin PET. It is observed that the Ag PNG structure of the period 10 μm has the lowest absorption intensity peak at 366 nm due to the LSPR. The spectrum shows that the peak is broad and extends up to NIR region due to the slow decay of the resonance

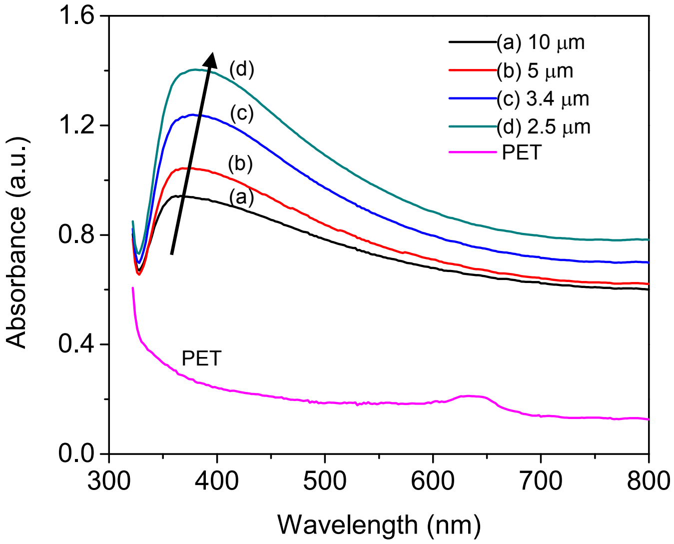

Figure 5.14 Absorption spectra of the PNG structure having 10, 5, 3.4, and 2.5 μm period.

peak. The resonance absorption peaks shift towards the higher wavelength side as the period of the PNG structure decreases from 10 μm to 2.5 μm. Also, the resonance peaks show an increase in the absorption along with the broadening in the spectral profile as the grating period is decreased. The virgin PET is found to be transparent in the whole visible region but has fundamental absorption band near about 320 nm wavelength [17]. These gratings have Ag nanoparticles of size 16 to 20 nm distributed along the grating strips. The depth of the gratings also decreases as the period of the grating decreases. This indicates that the plasmon resonance of the PNG structures will have contributions from the distribution of the Ag nanoparticles on the grating structure as well as on the nanoparticle layer present below the grating structure (Figure 5.11). The plasmon resonance peak shift in Figure 5.14 seems to be due to an increase in the volume fraction/covered area by the Ag nanoparticles. It has been reported that the LSPR peak is dependent mainly on the size and the shape of the nanoparticles [5], volume fraction of the nanoparticles as well as on the refractive index of the media surrounding the nanoparticles [28]. The effect of volume fraction

(F) of the nanoparticles and the refractive index (n_s) of the surrounding medium on the LSPR peak wavelength (λ_m) has been reported as [28]

$$\lambda_m = \lambda_p\left[1+\left(\frac{2+F}{1-F}\right)n_s^2\right]^{1/2} \qquad \textbf{5.2}$$

where λ_p is the plasmon resonance of the bulk metal. In this case, shape and size of the Ag nanoparticles present in the PNG structure as well as the refractive index of the gelatin (surrounding medium) are not changing. However, a decrease in the period of the grating increases the density of the Ag nanoparticles, which ultimately increases volume fraction (F) and finally the value of λ_m. This seems to be the reason behind a small change in the LSPR wavelength with a decrease in the period of gratings. An increase in the broadening of the LSPR peak is also observed with decrease in the grating period [29]. Similar broadening in the LSPR peak has been reported earlier in the case of polymer diffraction grating coated with Ag nanoparticles [17]. An increase in the broadening of the LSPR peaks with decrease in the periodicity of the grating may be due to an increase in the particle-particle interaction as a result of the increased particle and the line density for 2.5 µm grating [30]. Enhancement in the absorption signal in the PNG gratings can be attributed to the interaction of incident light with the free electrons in the Ag nanoparticles and excitation of the surface plasmon resonance in it. Similar enhancement in the absorption efficiency due to excitation of the surface plasmon resonance has been reported in the case of the Ag nanoparticles as well as in the Ag grating present near or embedded in the polymer layer [31],[32]. Particularly, an increase in the amplitude of the resonance peak (absorption) with a decrease in the periodicity (up to 2.5 µm) of the grating seems to be due to an increase in the (volume fraction) area covered by the nanoparticle/number density of the Ag nanoparticles as mentioned in Table 5.1.

Here, volume fraction is defined as the ratio of the region of the film exposed by the electron beam to the unexposed region. In this case, the Ag nanoparticles are present in the exposed region of the film. The ratio of exposed and unexposed area of in the fabricated grating increases with the decrease in the period of the grating as shown in Table 5.1.

5.7 Application of PNG structures as SERS substrate

In order to use these PNG structures as plasmonic sensor, the SERS spectra of the R6G dye (16 mM) drop coated on these gratings have been recorded. Figure 5.15 (a) shows the SERS spectra of the R6G deposited on the PNG structures having periodicity ranging from 10 to 2.5 µm. Various characteristic peaks are observed in the SERS spectra. It is found that the SERS intensity of all the peaks increases as the periodicity of PNG structures decreases from 10 to 2.5 µm. Figure 5.15(b) shows an enhancement in the SERS peak intensities as the period of grating changes for a constant concentration (16 mM) of R6G dye. It is observed that the maximum enhancement is ~3 times at 608 cm^{-1} peak as the period of grating decreases from10 µm to 2.5 µm. This enhancement varies from 2.5 to 3 times for various other peaks. An increase in the SERS peak intensities with the dye concentration has been shown in Figure 5.15(c) for the 10 µm PNG structure coated with different concentrations of R6G dye. It is observed that the SERS peak intensities increases with an increase in the dye concentration and start saturating after a concentration of ~6 mM. Some of the peak intensities decrease as the concentration of the dye increases from 4 to 16 mM. This indicates that some of the peaks are showing concentration quenching at higher concentration of the dye. Higher SERS intensities were observed for all the

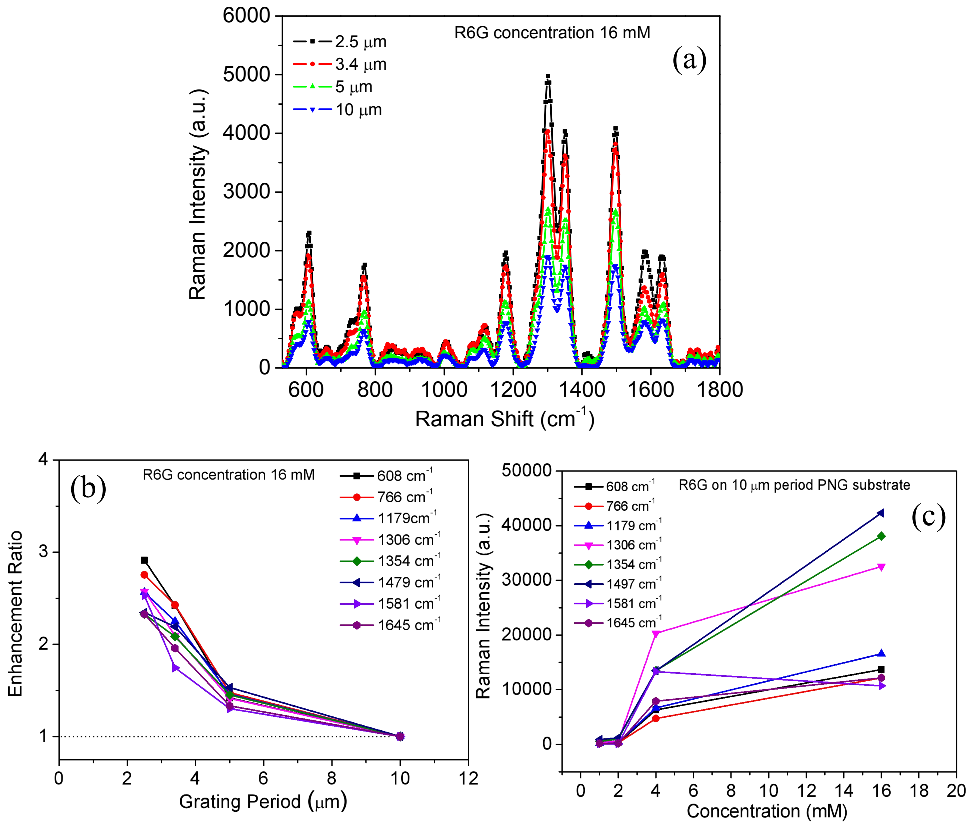

Figure 5.15: (a) SERS spectra of the drop coated R6G having concentration of 16mM on the PNG grating of 10, 5, 3.4, and 2.5 μm period. (b) Variation in the intensity of the Raman peaks with a change in the PNG grating period (R6G concentration 16 mM). (c) Variation in the intensity of the Raman peaks with a change in the concentration of R6G dye (grating period 10μm).

gratings. However, enhancement in intensity with decreasing grating period is monotonic (Figure 5.15(b)). A small improvement in the SERS signal with a decrease in the grating period seems to be due to the increased number of the grating lines and/or increased surface density of the Ag nanoparticles within the laser focal spot. Similar enhancement (~3 times) have been reported in the case of the pure metallic grating when the period was decreased from 800 to 400 nm [33]. This indicates that further decrease in the period of gratings in the present case may provide more enhancement in the SERS intensity. However, fabrication of such gratings needs further optimization of the lithographic process (e-beam writing).

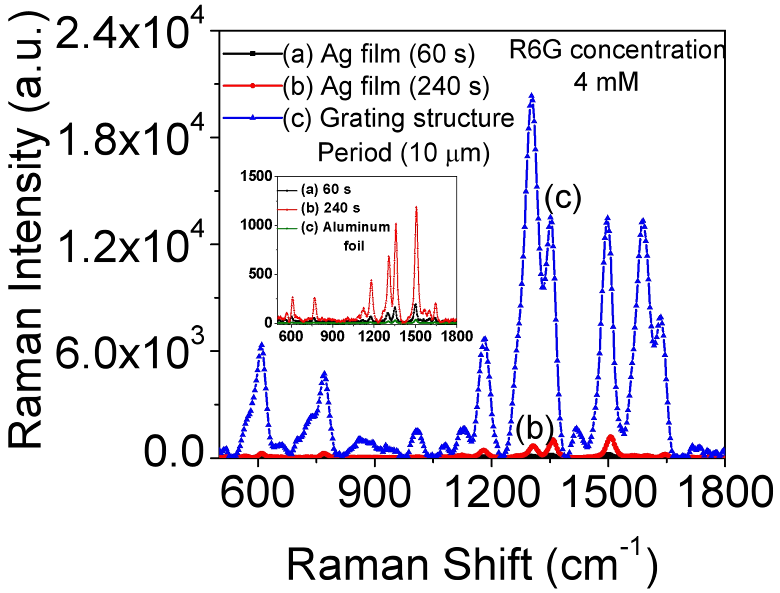

Figure 5.16 SERS spectra of drop coated R6G having concentration of 4mM on (a) silver thin film deposited for 60 s, (b) silver film deposited for 240 s, and (c) PNG structure period 10 µm. Inset shows the Raman spectra of R6G drop coated on Ag thin film and Al foil. The Raman spectra of R6G drop coated on Al foil is recorded to obtained the references R6G spectra with out Ag thin film.

In order to compare an enhancement in the SERS intensity on a different substrate, SERS spectra were recorded after coating similar dye concentration on the Ag thin films deposited for 60 and 240 s. Such thin films are supposed to have randomly distributed Ag nanoparticles of different shape and size as well as surface roughness (morphology). Many researchers have used such substrate for recording the SERS spectra [7]. Figure 5.16 shows the SERS spectra of the R6G dye of concentration 4 mM coated on the PNG structure (10 µm period) as well as on the randomly distributed nanoparticles of Ag deposited on the PET for 60 s and 240 s (deposited by sputtering). The background intensity from all the spectra has been subtracted to compare the SERS intensity at each peaking frequencies. It has been observed that the dye on the PNG structure of period 10 µm shows much higher SERS signal in comparison to the randomly distributed Ag nanoparticles in the form of thin films. Inset in Figure 5.16 shows that thin film deposited for 60 s is providing less SERS

TABLE 5.2: Enhancement in the SERS intensity from the PNG structure in comparison to the deposited thin films for different Raman frequencies.

R6G concentration 4 mM					
Peak position (cm^{-1})	PNG (10 μm)	Silver thin film (Deposited for 60s)		Silver thin film (Deposited for 240 s)	
	Raman Intensity I_{PNG} (a.u.)	Raman Intensity I_{60} (a.u.)	Gain (Enhancement) I_{PNG}/I_{60}	Raman Intensity I_{240}(a.u.)	Gain (Enhancement) I_{PNG}/I_{240}
608	6339	68	93.22	266	23.83
766	4731	54	87.61	255	18.55
1179	6688	66	101.33	439	15.23
1305	20335	105	193.67	685	29.69
1354	13513	160	84.46	1018	13.27
1479	13464	185	72.78	1188	11.33
1645	7893	53	148.92	203	38.88

signal than film deposited for 240s. This indicates that the thin film deposited for 60 s seems to be having less number density of the Ag nanoparticles. Therefore higher number density of the Ag nanoparticles, as well as increased surface roughness in the thick film deposited for 240 s, may be the reason behind the larger SERS signal [7]. Table 5.2 shows the peak intensity of SERS signal for most of the R6G peaks obtained on different substrates (grating structure and thin films) as shown in Figure 5.16. An enhancement in terms of gain in the Raman intensity has also been obtained for PNG structures in comparison to the thin and thick Ag films. Here, enhancement/gain is defined as the ratio of the Raman intensity from the PNG structure and the Ag films for the specific peak. It is noted that the PNG structure provides two orders of magnitude enhancement in the SERS signal in comparison to the thin film (60 s), whereas it is one order of magnitude in comparison to the thick film (240 s). However, this enhancement factor changes from peak to peak. Maximum enhancement ~39 times was noted for 1645 cm^{-1} peak in comparison to thick film, whereas it is ~194 times for 1306 cm^{-1} in the thin film case. The SERS enhancement in the case of the PNG structure occurs as a result of the plasmon resonance in the Ag nanoparticles as well as due to excitation of the waveguide mode [31],[34]. Both processes may be playing an equally important role. It has been reported earlier that the increase in SERS enhancement is possible due to the high electromagnetic coupling between very close metallic objects either in the case of nanoparticles or the form of periodic structures such as grating structure [3], [35]. This is similar to our observation of the SERS enhancement in 240 s deposited film in comparison to 60 s as discussed earlier. The SERS enhancement in the PNG grating with a smaller period (2.5 μm) is also due to a similar reason because the number density of nanoparticles is the highest in this case due to the superposition of the base of the grating rulings (Figure 5.11). These results indicate that the PNG structures fabricated using AgBr based microscope film may work as a superior plasmonic sensor with better sensitivity in comparison to the nanostructured Ag thin films. Its fabrication is easy in comparison to other techniques used for making metallic gratings. These periodic structures can be reproduced with the same parameters consistently in comparison to nanostructured Ag thin films. The optimization of the electron beam lithographic technique for the fabrication of the PNG structures can provide a large number of lines or small period in future to get even a more substantial enhancement/gain of the SERS signal. The main restricting factor in the fabrication of small period (< 2 μm) grating in the present case is the higher thickness (3.5 μm) of the AgBr layer. If thin AgBr layer is used for the electron beam exposure, the neck region of electron beam interaction volume (teared shape volume) can be use for the fabrication of smaller period grating. Moreover, no overlapping between the of interaction volume of adjacent line exposure will occurs in the AgBr layer. In that case, the same conventional SEM can be used for the production of smaller period gratings. The double exposure of electron beam in a different direction on the film can provide 2-D nanoparticle array instead of the grating (1-D nanoparticle array). Such structures may also be beneficial for further enhancement of the sensitivity of the SERS signal. It is important to note that the excitation wavelength also play a significant role in the SERS enhancement. Here, excitation wavelength (λ_{ext}) is 785 nm which is far away from the LSPR peak position (λ_{LSPR}) of PNG structures. It is demonstrated in the literature that λ_{LSPR} should lie between the λ_{ext} and Raman wavelength signal (λ_{RS}) for higher SERS enhancement. Maximum enhancement occurs when $\lambda_{LSPR}= (\lambda_{ext}+\lambda_{RS})/2$ [4]. So in the present case, if we reduce λ_{ext} , more SERS enhancement can be achieved. But for lower λ_{ext}, we have to compromise with the large fluorescence signal. However, large fluorescence background appear for the lower λ_{ext} which suppress the weak Raman signal. However, it is a matter of further investigation.

5.8 Conclusions

The PNG structures of different periods have been fabricated on the transmission electron microscopy film by the reduction of silver halide (AgBr) grains into metallic silver (Ag) after exposing it to the electron beam from the conventional SEM. The exposure followed by the development and fixing process provide good quality PNG structures. Morphological studies of the PNG structures performed by the SEM and the AFM show that the depth of the groove in grating decreases and the area of the film covered by the Ag strips increases with an increase in the number of lines per frame in the grating. The optical absorption spectra of the PNG structures indicate that the redshift in LSPR peak with a decrease in the period of the gratings. The amplitude of the LSPR peak, as well as its width, also increases with the reduction of the period of the grating as a result of the increased number density of the Ag nanoparticles (area covered by Ag) in observation region. It has been noted that the Raman signal obtained from R6G dye coated on the PNG grating (10 μm period) provides an enhancement by two orders of magnitude in comparison to the randomly distributed Ag nanoparticles deposited on the virgin PET substrate for 60 s. Even 3 times improvement in the Raman signal was noted, when the period of the gratings decreased from 10 to 2.5 μm. This indicates that a further decrease in the period of gratings may increase the SERS signal. This study shows that the PNG structures obtained using EBL can be used as a sensitive sensor for the surface-enhanced Raman spectroscopy. The advantage of this technique in making the PNG structures includes high reproducibility, large area fabrication, easy, fast and low-cost fabrication. The versatility of this method is that by using conventional scanning electron microscope, one can fabricate such plasmonic structures. Even double exposure of the film in different directions can provide a 2D-nanoparticle array which may further enhance the sensitivity of PNG structure, which is a matter of further investigation.

References:

[1] W. C. Hung, W. H. Cheng, M. S. Tsai, W. C. Chung, I. M. Jiang, and P. Yeh, "Laser pulse induced gold nanoparticle gratings," *Appl. Phys. Lett.*, vol. 93, no. 6, 2008.

[2] T. K. Liu, W. C. Hung, M. S. Tsai, Y. C. Tsao, and I. M. Jiang, "Fabrication of tunable grating with silver nanoparticles," *Proc. SPIE*, vol. 7390, no. 73901A, pp. 1–9, 2009.

[3] M. Panagopoulou, N. Pantiskos, P. Photopoulos, J. Tang, D. Tsoukalas, and Y. S. Raptis, “Raman enhancement of rhodamine adsorbed on Ag nanoparticles self-assembled into nanowire-like arrays,” *Nanoscale Res. Lett.*, vol. 6:629, pp. 2–7, 2011.

[4] M. Kahraman, P. Daggumati, O. Kurtulus, E. Seker, and S. Wachsmann-Hogiu, “Fabrication and characterization of flexible and tunable plasmonic nanostructures,” *Sci. Rep.*, vol. 3:3396, pp. 1–9, 2013.

[5] A. Bansal and S. Verma, “Searching for Alternative Plasmonic Materials for Specific Applications,” *Indian J. Mater. Sci.*, vol. 897125, pp. 1–10, 2014.

[6] M. Fleischmann, P. J. Hendra, and A. J. M. Quilllan, “Raman spectra of pyridzne adsorbed at a silver elelctrodes,” *Chem. Phys. Lett.*, vol. 26, no. 2, pp. 163–166, 1974.

[7] M. Moskovits, “Surface-enhanced spectroscopy,” *Rev. Mod. Phys.*, vol. 57, no. 3, pp. 783–826, 1985.

[8] G. Editor and P. Arnold, “surface-enhanced Raman scattering,” *J. Phys. Condens. Matter*, vol. 4, pp. 1143–1212, 1992.

[9] X. Zhang, M. Theuring, Q. Song, W. Mao, M. Begliarbekov, and S. Strauf, “Holographic control of motive shape in plasmonic nanogap arrays,” *Nano Lett.*, vol. 11, pp. 2715–2719, 2011.

[10] X. Zhang and S. Strauf, “Formation of triplet and quadruplet plasmonic nanoarray templates by holographic lithography,” *Appl. Phys. Lett.*, vol. 102, no. 93110, pp. 1–5, 2013.

[11] J. Lutkenhaus, D. George, M. Moazzezi, U. Philipose, and Y. Lin, “Digitally tunable holographic lithography using a spatial light modulator as a programmable phase mask,” *Opt. Express*, vol. 21, no. 22, pp. 26227–26235, 2013.

[12] B. Yan, A. Thubagere, W. R. Premasiri, L. D. Ziegler, L. D. Negro, and B. M. Reinhard, “Engineered SERS substrates with multiscale signal enhancement: nanoparticle cluster arrays,” *ACS Nano*, vol. 3, no. 5, pp. 1190–1202, 2009.

[13] S. Astilean, M. Bolboaca, D. Maniu, and T. Iliescu, “Ordered metallic nanostructures for surface-enhanced Raman spectroscopy,” *Rom. Reports Phys.*, vol. 56, no. 3, pp. 346–351, 2004.

[14] A. Kocabas, G. Ertas, S. S. Senlik, and A. Aydinli, “Plasmonic band gap structures for surface-enhanced Raman scattering.,” *Opt. Express*, vol. 16, no. 17, pp. 12469–12477, 2008.

[15] M. Geissler, K. Li, B. Cui, L. Clime, and T. Veres, “Plastic substrates for surface-enhanced raman scattering,” *J. Phys. Chem. C*, vol. 113, pp. 17296–17300, 2009.

[16] K. B. Biggs, J. P. Camden, J. N. Anker, and R. P. V. Duyne, “Surface-enhanced raman spectroscopy of benzenethiol adsorbed from the gas phase onto silver film over nanosphere surfaces: Determination of the sticking probability and detection limit time,” *J. Phys. Chem. A*, vol. 113, pp. 4581–4586, 2009.

[17] M. Fan, G. F. S. Andrade, and A. G. Brolo, “A review on the fabrication of substrates for surface enhanced Raman spectroscopy and their applications in analytical chemistry,” *Anal. Chim. Acta*, vol. 693, pp. 7–25, 2011.

[18] S. J. Beck, *Electron Microscopy: A Handbook of Techniques for the Biologist*. Nassau Community College, 1996.

[19] “Physical properties of polyester film base,” *Technical bulletin*, Eastman Kodak Company, p. TI-2598, 2010.

[20] S. Liu, J. Yue, S. Fu, and H. Kobayash, “Investigation on nanocrystallite silver halide photographic emulsion,” *Imaging Sci. J.*, vol. 46, no. 2, pp. 69–72, 1998.

[21] K. Dai *et al.*, “Facile synthesis of a surface plasmon resonance-enhanced Ag/AgBr heterostructure and its photocatalytic performance with 450 nm LED illumination,” *Dalt. Trans.*, vol. 42, pp. 4657–4662, 2013.

[22] H. Zheng, P. Li, L. Gao, and G. Li, “RSC Advances Hexagonal AgBr crystal plates for e ffi cient photocatalysis through two methods of degradation : methyl orange oxidation and Cr VI,” *RSC Adv.*, vol. 7, pp. 25725–25731, 2017.

[23] C. E. Hall and A. L. Schoen, “Application of the electron microscope to the study of photographic phenomena,” *J. Opt. Soc. Am.*, vol. 31, no. 4, pp. 281–285, 1941.

[24] M. Altissimo, “E-beam lithography for micro-/nanofabrication,” *Biomicrofluidics*, vol. 4, no. 26503, pp. 1–6, 2010.

[25] “Monte Carlo Simulation of electron trajectory in solids,” *Casino V2.48*, 2011. [Online]. Available: www.gel.usherbrooker.ca.

[26] K. Sangeeth and G. M. Hegde, “Fabrication and characterization of sub 100 nm period polymer gratings for photonics applications,” *Curr. Sci.*, vol. 107, no. 5, pp. 749–752, 2014.

[27] M. A. Majeed Khan, S. Kumar, M. Ahamed, S. A. Alrokayan, and M. S. AlSalhi, “Structural and thermal studies of silver nanoparticles and electrical transport study of their thin films,” *Nanoscale Res. Lett.*, vol. 6:434, pp. 1–8, 2011.

[28] J. I. Treu, “Mie scattering, Maxwell Garnett theory, and the Giaever immunology slide,” *Appl. Opt.*, vol. 15, no. 11, pp. 2746–2750, 1976.

[29] V. N. Rai, “Optical properties of silver-island films having an overlayer of RhB dye.,” *Appl. Opt.*, vol. 26, no. 12, pp. 2395–400, 1987.

[30] T. J. Davis, K. C. Vernon, and D. E. Gómez, “Designing plasmonic systems using optical coupling between nanoparticles,” *Phys. Rev. B - Condens. Matter Mater. Phys.*, vol. 79, no. 155423, pp. 1–10, 2009.

[31] Z. Sun, Y. S. Jung, and H. K. Kim, “Role of surface plasmons in the optical interaction in metallic gratings with narrow slits,” *Appl. Phys. Lett.*, vol. 83, no. 15, pp. 3021–3023, 2003.

[32] H. Shen, P. Bienstman, and B. Maes, “Plasmonic absorption enhancement in organic solar cells with thin active layers,” *J. Appl. Phys.*, vol. 106, no. 73109, pp. 1–5, 2009.

[33] M. Kahl, E. Voges, S. Kostrewa, C. Viets, and W. Hill, “Periodically structured metallic substrates for SERS,” *Sensors Actuators, B Chem.*, vol. 51, pp. 285–291, 1998.

[34] P. Senanayake *et al.*, “Surface plasmon-enhanced nanopillar photodetectors,” *Nano Lett.*, vol. 11, pp. 5279–5283, 2011.

[35] F. J. García-Vidal and J. B. Pendry, “Collective Theory for Surface Enhanced Raman Scattering.,” *Phys. Rev. Lett.*, vol. 77, no. 6, pp. 1163–1166, 1996.

Chapter 6

Optical diffraction studies on plasmonic grating structures

6.1 Introduction

The diffraction grating is an essential optical component, which has extensive development in the field of fundamental and engineering optical sciences [1]. Generally, gratings are categorized based on its geometrical configuration (plane, concave, and convex), execution of state (absorption, phase and mixed) and the mode of utility (transmission and reflection) [2]. Usually, a reflection type gratings are exploited for almost all the optical appliances. Recently, transmission gratings are explored to accomplish nearly 100% optical diffraction efficiency along with tunable spectral bandwidth, which are rarely sensitive to the optical misalignment [2]. The output characteristics (efficiency and bandwidth) of the planar transmission gratings are defined by a parameter Q (normalized grating thickness), where the thin grating ($Q < 1$) exhibit the Raman-Nath diffraction behavior, while the thick gratings ($Q > 10$) obey Bragg diffraction behavior [3]–[6]. The region between $1 < Q < 10$ is not very well defined as it overlaps between Raman-Nath diffraction and Bragg diffraction behavior [7]–[9]. Furthermore, if the period of the grating is very much larger than incident wavelength and modulation depth of grating then it is contemplated within the thin grating range. In thick sinusoidal gratings, the zeroth and the first order diffraction are desirable modes, and 100% theoretical diffraction efficiency (DE) can be obtained in the first order diffraction spectra [7]. In the thin sinusoidal phase gratings, the existence of higher diffraction orders suppresses the first order DE up to ~33.8% [7]. However, the DE is still low ~4.8% and ~6.25% for thin sinusoidal absorption and transmittance gratings respectively, which can be increased by using a appropriate technology [8]. The localized surface plasmon resonance (LSPR) [10] generation in metal nanoparticles intensifies light transmission, absorption, and scattering, which has been found useful in different applications like SERS sensors [11]–[13], fluorescence microscopy [14], optical switching [15], enhancement of DE as well as wavelength tuning of both the thin [16]–[20] and the thick gratings [21]–[24] as well as in various other multidisciplinary applications [25]. The DE and its bandwidth in thin plasmonic nanoparticle transmission gratings (PNG) is calculated primarily by the magnitude of spatial modulation of the refractive index (n) and the absorption coefficient (α) along with the phase deviation between these spatial modulations, where maximum DE is anticipated with zero phase difference. Even, the readout wavelength, angle of incidence, and state of polarization of source light also control the total performance of the grating [16]–[20]. The variation in absorption coefficient in the grating is assimilated either by the periodic decoration of plasmonic nanoparticles [17], [19], [20] or by the periodic change of the refractive index of surrounding medium associated with the self-assembled plasmonic nanostructured thin film over a substrate [16], [26]. The ingratiation of PNGs on a flat substrate has been demonstrated by using laser interference technique, liquid crystal based techniques as well as using optical lithography [16]–[21]. The laser interference methodology based on the photo-reduction process exhibits a change in gold (Au) nanoparticles size in PNG structure (~25 µm period), but these structures are associated with some cracks along with very less DE ~0.01% [21], [22]. The periodic change in refractive index of interacting medium over the silver (Ag) nanoparticles render DE ~9% [16], [17]. The PNG structures of ~8 and ~12 μm period fabricated by optical lithography also exhibit a tuned DE profile [19], [20]. However, these methods for the fabrication of PNG structures are not simple and also time-consuming. In the previous chapter, a potential and easy technique for the fabrication of PNG grating of various periodicities has been demonstrated using the EBL on silver halide (AgBr) emulsion films for SERS application. However, the effect of modification in the parameters of EBL process on the performance of PNG grating fabricated on AgBr films was not delineated. So, it is worthy to examine the role of electron beam processing parameters on the performance of the gratings especially on the plasmonic outcome and its DE to optimized an efficient grating structure. This chapter presents the role of electron beam energy (dose) on the morphology (shape and height) and LSPR response and experimental testing of DE followed by the theoretical analysis (Raman-Nath diffraction). The detailed fabrication procedure of the PNG structures is described in chapter 2 and chapter 5. Two sets of PNG structure are fabricated using a conventional SEM on a AgBr based film. In one set, PNG structures of the different period are fabricated by varying the number of lines in a constant scanning area at a fixed exposure energy of electron beam. In another set, PNG structures of different height are fabricated using different exposure energy of scanning electron beam for a fixed number of line at a constant scanning area. The fabrication of different period grating structures are rigorously studied in chapter 5 and used as superior chemical sensors compared to similar type of island film. In this chapter morphological imaging of the fabricated PNG structures of set-2 is carried out using LM and AFM techniques. The LSPR response of PNG structures is also recorded using absorption spectroscopy. The DE testing of PNG structure of both the sets (set-A and set-B) is performed on a custom-made set-up. The detailed information about the experimental set-up is described in chapter 2. Finally, the theoretical analysis based on Raman-Nath diffraction of PNG structures are done to describe the experimental observed response of DE.

6.2 Morphological characterization of PNG structures

Figure 6.1 presents the optical microscopic images of the PNG structures fabricated at 5, 10, 15 and 30 keV. It can be seen that the period of the gratings produced at different energies (both of the sets) is almost same because of a fixed number of lines per frame used during all the raster scans of electron beam exposures. The lowest electron beam energy of 5 keV is found close to the threshold for the formation of the PNG structure as the grooves are not sharper and well defined. In the case of 10 keV,

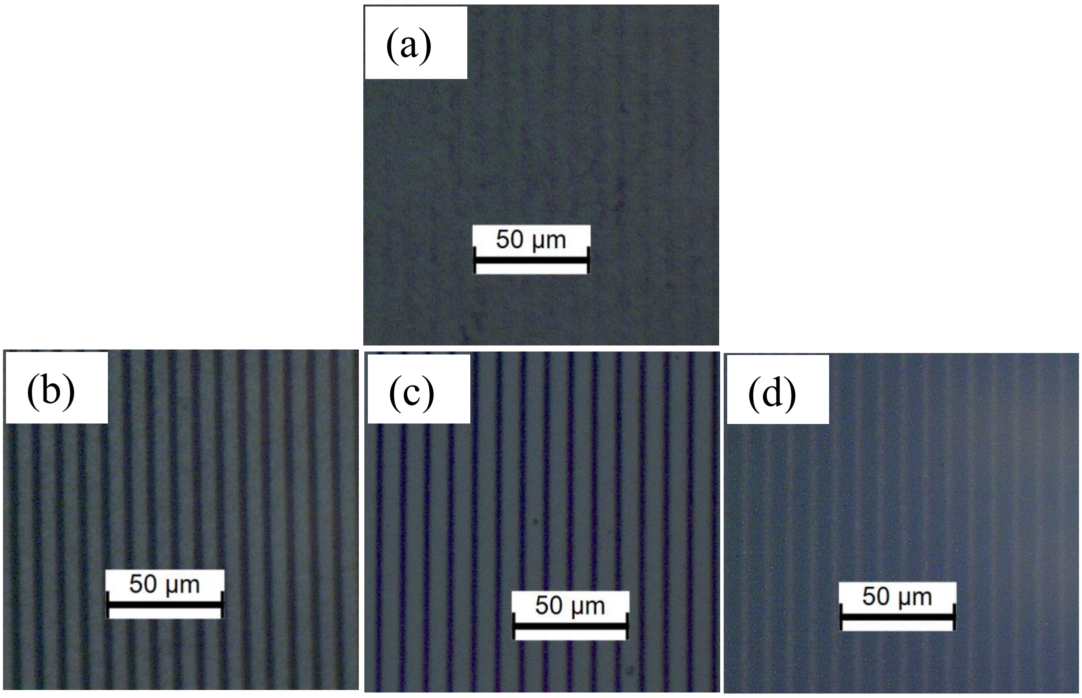

Figure 6.1 Optical microscopic images of the PNG structures fabricated by the electron beam accelerated at (a) 5 keV, (b) 10 keV, (c) 15 keV and (d) 30 keV.

the clearly observable regularly spaced grating is formed whereas its quality degrades for 30 keV because of excess enlargement in the line-width of the grating. However, it can be observed that the grating fabricated at 15 keV is exhibiting sharper and better contrast between the two adjacent lines.

AFM analysis was carried out to evaluate the detailed morphological features of the fabricated PNG structure. Figures 6.2 (a)-6.2 (f) show the AFM image and the line scan profiles of the PNG structures fabricated at 10, 15 and 30 keV electron beam

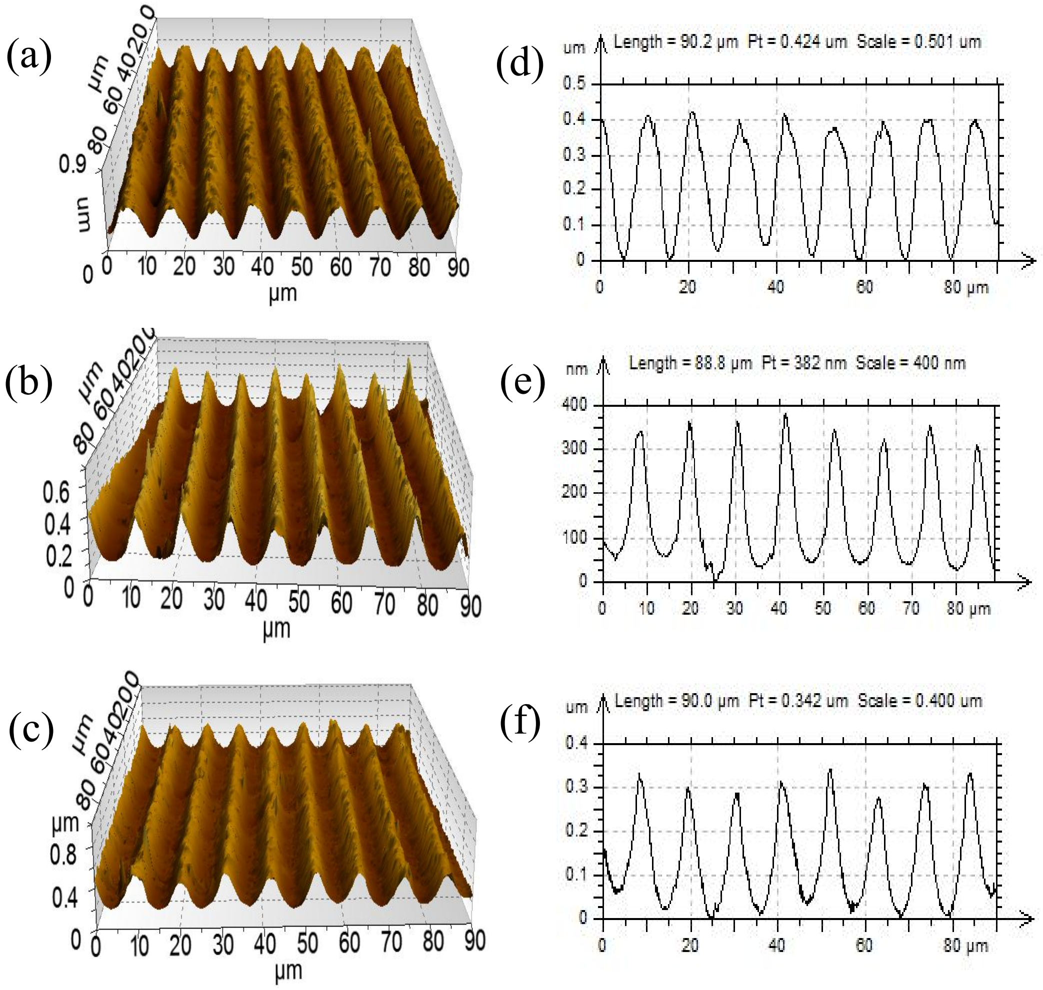

Figure 6.2 AFM images of the PNG structures along with corresponding line scan profiles of the gratings. (a, d) 10 kV, (b,e) 15 kV and (c,f) 30 kV.

energy. The line scan profile of the PNG structures provide the periodicity of the gratings as ~10 µm for each of the gratings whereas the depth of these gratings are

~400, ~350 and ~300 nm for 10, 15, and 30 keV electron beam energies respectively. The full width at half maxima (FWHM) obtained from the AFM line scan is found as ~6.12, ~3.42 and ~3.7 µm for the grating made at 10, 15, and 30 keV respectively. The variation in height and FWHM of the gratings formed at the different accelerating voltage of the electron beam can be explained on the basis of difference in the volume of the electron beam irradiated material (interaction volume) and on the dose of the electron beam irradiation at these voltages. At higher electron accelerating voltage, this process occurs with an increased interaction volume along with higher dose. The increased interaction volume results in an overlapping of interaction zones between two adjacent raster scans as shown in the Figure 5.11 of chapter 5. This overlapping ultimately produces a uniform layer of Ag nanoparticles over which the grating structure is formed. The uniform layer of the Ag nanoparticles beneath the grating structure decreases the depth and the FWHM of the gratings fabricated at higher voltages. In the case of a grating fabricated by 15 keV electron beam, the depth lies between the values obtained for the gratings fabricated by 10 keV and 30 keV electron beam. However, a small variation in the depth and the FWHM are possible because of separate processing conditions in the gratings fabricated at different energies.

Similar to the previous chapter 5, morphological imaging, elemental spectra and mapping analysis of the fabricated PNG structure is carried out by the conventional SEM. Figure 6.3(a) represent the SEM images of fabricated grating. The period of the grating is obtained ~10 µm. The EDS spectra shows the presence of only Ag in the fabricated PNG structures. No bromine peaks at ~ 1.75 and 11.8 keV in the EDS spectra is observed. The elemental mapping also depicts the periodicity of ~10 µm of

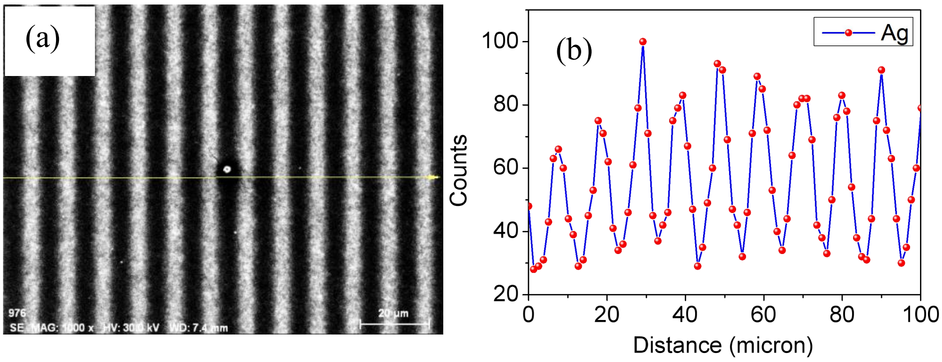

Figure 6.3 (a) SEM image and (b) EDS line scan of fabricated PNG structure.

Ag (Figure 6.3(b)). The AgBr particles in the film reduced into Ag nanoparticles of ~18±2 nm after fabrication process (electron beam exposure, development and fixing process). The size of the Ag nanoparticles is obtained using x-ray diffraction (XRD) pattern recorded by synchrotrons radiation source, similar to our previous reported result [27].

6.3 Optical characterization of PNG structures

Figure 6.4 shows the absorbance spectra of the Ag nanoparticle gratings fabricated using 10, 15 and 30 keV electron beam. The grating fabricated using 10 keV electron beam shows a broad absorption profile peaking at ~400 nm due to excitation of LSPR in the Ag nanoparticles present on the ridges of gratings [27]. In the case of 30 keV grating, the absorption spectrum shows two peaks are at ~420 nm and a more pronounced second peak at ~485 nm wavelength. Moreover, the absorbance of 30 keV grating is higher compared to the 10 keV grating. This increase in the absorbance of 30 keV grating may be due to the presence of a uniform Ag layer below the grating structure, which occurs due to overlapping of the raster scan during its fabrication. The absorbance of 15 keV grating is lower than even 10 keV grating because of its lower relief depth (which corresponds to Ag content) and the absence

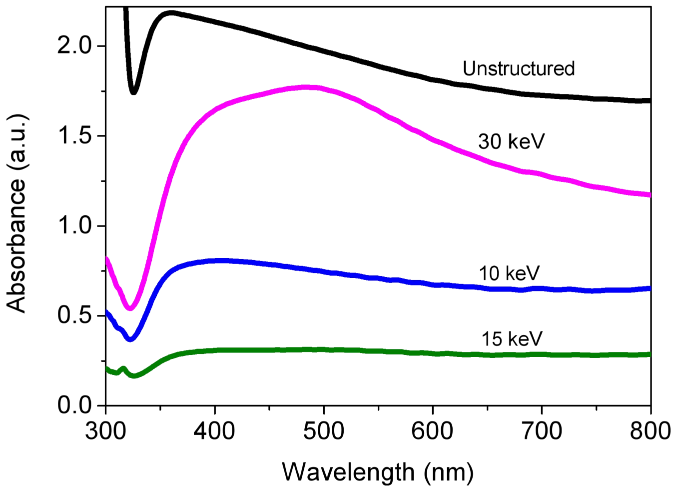

Figure 6.4 Absorbance spectra of the PNG structures (10 µm period) fabricated by electron beam accelerated at 10, 15, and 30 kV as well as a unstructured Ag nanoparticle film generated with the same approach.

of under-layer of Ag nanoparticles (Figure 6.1 and Figure 6.2). Figure 6.4 shows that the absorbance of the gratings mainly depends on its structure. For the gratings fabricated at the lower energies, the absorbance directly corresponds to the height of the grating, which ultimately increases the number density of the Ag nanoparticles. Moreover, an increase in the FWHM of the grating profile also increases the number density of Ag nanoparticles for a constant depth. Furthermore, in the case of higher energy processing condition of 30 keV, the grating height decreases along with the formation of an underneath uniform layer of Ag nanoparticles as discussed above. This uniform Ag nanoparticles layer considerably increases the number density of nanoparticles contributing to a very strong plasmonic resonance peak. However, the observation of two peaks at ~420 nm and ~484 nm, in the case of 30 keV grating, may be due to increase and elongation in the size of the Ag nanoparticles. This may be due to the growth of Ag nanoparticles in the form of non-spherical (elongated) shape under the effect of high energy electron beam and high beam current. Such type of growth in the size of Ag nanoparticles under high energy electron beam irradiation has been reported earlier [28]. The absorbance spectrum of the elongated nanoparticles can provide two plasmon resonance peaks as has been observed in the case of 30 keV grating [29]. The observation of broadening in the LSPR peak may be either due to the comparatively larger size of the nanoparticles or due to increased particle-particle interactions in the grating [30]. Even both the effect may be playing an important role in the broadening. It is observed that once the number of lines on the grating increases the periods of the grating decrease [27]. No grating structure is formed for the grating having 2904 number of lines per frame. This is due to overlapping of the adjacent exposure of electron beam during the raster scan. Finally, it provides a nearly random distribution of Ag nanoparticles (unstructured nanoparticles) on the PET after developing and fixing process. For comparison purpose, optical spectra of such unstructured film are also shown in Figure 6.4, which also indicates similar LSPR with high intensity due to the higher density of Ag nanoparticles.

6.4 Diffraction efficiency testing of PNG structures

The morphological, optical and elemental characterization of set-A and set-B are performed in previous chapter (chapter 5) and in previous section of the current chapter (chapter 6) respectively. The PNG structures of set-A are used as a SERS substrate as described in chapter 5. The DE testing of both set-A and set-B is carried out which is described in subsequent section. The DE of PNG structures was measured using the experimental setup as shown in Figure 2.9 of chapter 2, in the wavelength range 350-800 nm. The transmitted light intensity (I_0) from the virgin PET substrate (without grating structure) and the diffracted light intensity from the fabricated grating into the first order (I_{+1}) were measured. The ratio (I_{+1}/I_0) is defined as the DE, which was determined for each of the grating structures. In the above measurements, scattering and reflection from the grating-PET interface and grating-air interface are not included.

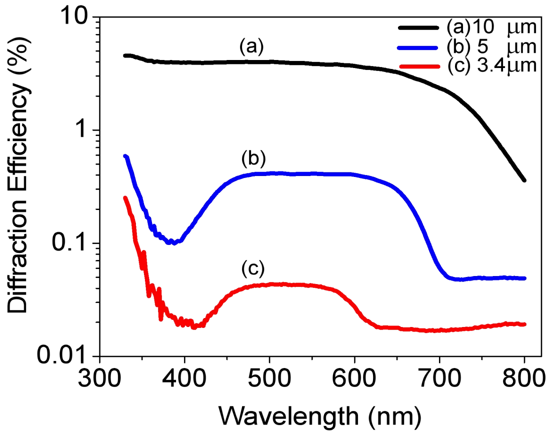

Figure 6.5 Variation in the experimentally measured first order diffraction efficiency and bandwidth for plasmonic surface relief grating structures of different period fabricated at 30 kV electron beam accelerating voltage.

The investigation of optical diffraction properties of all the fabricated PNGs of set-A has been performed to demonstrate its application as a band-pass filter. Figure 6.5 shows the experimentally measured first order DE for the gratings of 10, 5 and 3.4 µm period from 350 to 800 nm visible spectral range. The maximum first order DE of ~4% is observed for 10 µm period grating along band width (BW) of ~450 nm. Moreover, the nature of the DE is remarkably flat over the 350 to 650 nm (flatten BW ~300 nm) spectral range and dropped significantly at the higher wavelength side. As the grating period decreases from 10 µm to 5 µm, the magnitude of DE reduces almost by one order. In addition, suppression in the BW also occurs from both sides of the spectral wavelength that makes DE profile narrower to ~300 nm (~400 to ~700 nm). Nevertheless, flatten nature of DE profile remains same in the suppressed BW. The flat spectral BW reduced to ~200 nm (from ~450 to ~650 nm) for 3.4 µm grating period. In this case, the magnitude of DE again reduces by nearly one order of magnitude than the 5 μm period grating. The comparison of Figure 5.8 and Figure 6.5 shows that the diffraction efficiency, as well as the BW of the gratings, decreases with an increase in the number of lines in the grating (decrease in the period). This is due to a decrease in the height of grating or due to an increase in the number density of Ag nanoparticles in the grating as the period of grating decreases.

The occurrence of flat nature in the DE profiles, reduction in DE magnitude and narrowing in the BW can be understood qualitatively in terms of (1) decrease in the grating period and its height and (2) increase in LSPR based absorption of Ag nanoparticle embedded in the grating material (gelatin matrix) (Figure 5.14). In fact, the fabricated gratings are the "mixed gratings" in which the periodic variation in the height of PNG produces a periodic variation in the extent of Ag nanoparticles that ultimately leads to the modulation of absorption coefficient (α). It can be seen that as the grating period decreases, it accompanies a relative decrease in the height of the grating along with increases in the thickness of the bottom layer. This leads to a reduction in the modulation amplitude of absorption coefficient ($\Delta\alpha_1$) and an enhancement in average absorption coefficient (α_{ave}). The decrease in the $\Delta\alpha_1$ seems to be playing an important role in reducing the BW of diffraction profile of the grating. Whereas, an increase in the α_{ave} produces the significant absorption that ultimately leads to the reduction in the DE of the grating. This increased absorption may be associated with the increased scattering due to the Ag nanoparticles present in the grating. It is reported earlier for the surface relief transmission grating that spectral BW is directly proportional to the period and inversely proportional to the thickness of the grating [31]. In the present case, thickness effect is found opposite or may be negligible. Results indicate that decreasing the thickness of the uniform layer of Ag nanoparticle below grating may increase the efficiency of the grating manifold.

However, full theoretical reproduction of DE profiles required rigorous calculation of Raman-Nath diffraction theory. It seems that DE enhancement and BW shortening/broadening can be tuned by variation in the thickness of the bottom absorbing layer, grating height and grating period by optimizing the EBL technique. Finally, this is a very easy, low cost and less time-consuming technique providing a large BW with a flat DE profile.

Figure 6.6 shows the experimentally measured first order DE profiles of the Ag nanoparticle gratings of set-2. The maximum DE and the bandwidth obtained from the measurements for each grating (Figure 6.6) are presented in Table 6.1. The Ag nanoparticle grating prepared by 10 keV electron beam shows a broad DE profile in the wavelength ranges from 450 nm to 800 nm with a peak DE ~4.6%. However, the grating fabricated with 30 keV electron beam has shown much less DE ~2.8% at 800 nm than those fabricated at low electron beam energy of 10 keV (~4.6%) and 15 keV (~7.2%). Such decrease in the DE of the grating fabricated at 30 keV electron beam

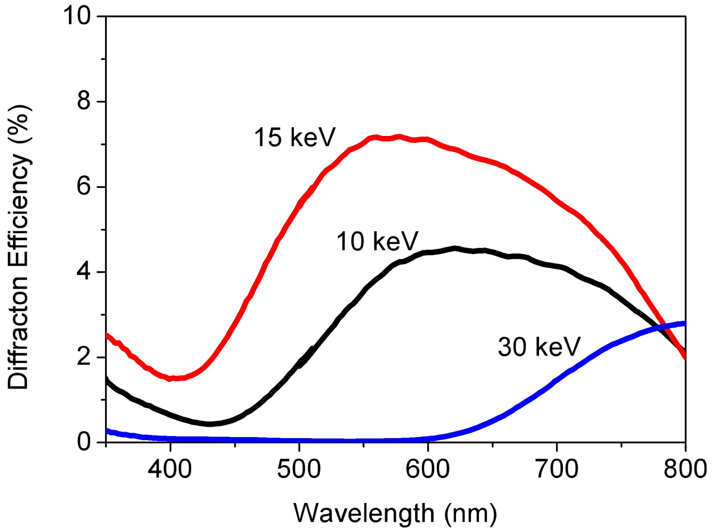

Figure 6.6 Variation in the experimentally measured diffraction efficiency of the PNG structures of 10 μm period, fabricated at 10, 15 and 30 kV electron beam accelerating voltages.

energy seems to be due to the presence of a uniform layer of the Ag nanoparticles below the grating structure as discussed above, which may be contributing significantly towards scattering and/or absorption of the light in the wavelength range from 400-600 nm. In this case, DE is peaking in the near-infrared region. This kind of grating structures having a uniform Ag layer below it and plasmon resonance at higher wavelength find application in the surface-enhanced Raman spectroscopy (SERS) [27].

TABLE 6.1: Experimental data obtained for different gratings.

Exposure energy (keV)	Grating period (μm)	Grating thickness d (nm)	Maximum diffraction efficiency η (%)	Peak position (nm)	Diffraction wavelength band in visible range Δλ (nm)
10	10	400	4.6	610	450-800
15	10	350	7.2	560	420-800
30	10	300	2.8	800	650-800

In the case of grating fabricated at 15 keV, the maximum DE is measured as ~7.2% whereas bandwidth ranges from 420 nm to 800 nm in visible range respectively. This DE is ~6 times larger compared to the value reported in the literature [17]. This result reveals that the grating structures providing maximum DE can be fabricated by using an optimum electron beam energy of ~15 keV. In this condition, the gratings are formed with a maximum depth of modulation without forming a uniform constant absorbing layer of Ag nanoparticles below the grating structure. Also, a blue shift in the peak position of DE is observed for the 15 keV grating. In fact, the DE profiles of the gratings get red shifted (Figure 6.6) as the absorption of the gratings increase (Figure 6.4). This indicates towards the critical role of LSPR in the enhancement of DE as well as in deciding the location of the DE profile. The similar blue shift in the

DE has been reported earlier when a continuous metallic strip present in the grating converted to nanoparticles grating after annealing [19], [20]. The above analysis indicates that the involvement of LSPR can enhance the performance of such gratings, mainly its DE. Even, it can decrease the DE if a layer of the constant thickness of nanoparticles is present below the grating structure. Although, all geometrical parameters of the grating play an essential role in deciding the performance spectra (Table 6.1). But the DE of the gratings, as well as the peak position of the DE profiles, are found correlated with the LSPR profiles.

6.5 Theoretical analysis of diffraction efficiency of PNG structure

Analysis of the DE of the Ag nanoparticle grating of set-B is carried out based on the Raman-Nath diffraction theory to explain the experimental findings. The applicability of the Raman-Nath diffraction theory has been justified by the normalized thickness parameter Q of the grating defined as [4]

$$Q = 2\pi\lambda d \Big/ \Lambda^2 n_{ave} \qquad \textbf{6.1}$$

Here λ, d, Λ, and n_{ave} are the readout wavelength, relief depth, period and the average refractive index of the grating. In the present case, the maximum value of Q for the gratings have been found < 0.018 for all of the possible cases. However, it is seen that the parameter Q has been discussed controversially in the literature [32]. Therefore, another parameter ρ is found equally important to determine the grating behavior, which is defined as [33]

$$\rho = \lambda^2 / \Lambda^2 \Delta n_1 n_{ave} \qquad \textbf{6.2}$$

where Δn_1 is the refractive index modulation in the grating. When $\rho < 1$ then the grating behavior is Raman-Nath like, and it is considered thin, and for $\rho >> 1$ it is thick. In the present case, a maximum value of ρ for all of the gratings is found < 0.058. Both the parameters Q and ρ satisfies the Raman-Nath criteria of the thin grating for all of the PNG structures. In a particular case when the geometrical parameters of the grating d/Λ (grating aspect ratio) < 0.1 and $\lambda/\Lambda << 1$ then the gratings are considered as thin grating, which rarely shows any polarization and angular dependency [9], [34]. In the present case the values of d/Λ and λ/Λ have been found as ≤ 0.05 and ≤ 0.08 respectively for all of the gratings from 300 nm to 800 nm wavelength range, which fulfills the above conditions. It is important to mention here that we observed up to 7 orders of diffracted light in our experimental setup, whereas only zeroth and the first order spots are shown on the screen in Figure 2.9 for clarity in presentation. The above conditions fulfill the Raman-Nath diffraction criteria. Also, when the relief modulation is very small (large period), then both volume holographic and the surface relief grating (SRG) follow Rama-Nath diffraction behavior at normal incidence and can be treated equally with a single formulation [34]. According to Raman-Nath diffraction theory, the first order DE (η) of the thin grating can be written as [16],[26]

$$\eta = \exp(-2\Delta\alpha_1 d)\left| J_1\left(\frac{2\pi\Delta n_1 d}{\lambda}\right) - i\Delta\alpha_1 d \right|^2 \qquad \textbf{6.3}$$

Where $\Delta\alpha_1$ is the modulation in the absorption coefficient of a grating with wavelength, d is the thickness of the grating, J_1 is the first kind Bessel function, Δn_1 is the modulation amplitude in the refractive index for the fabricated grating structure.

In the present case, if the absorption coefficient of the grating medium (Ag embedded in gelatin) and air are written as $\alpha_{(Ag+gelatin)}=\alpha_1$ and $\alpha_{(air)}=\alpha_2=0$ respectively, then the average absorption coefficient α_{ave} and modulation in the absorption coefficient $\Delta\alpha_1$ can be written as

$$\alpha_{ave}=\left(\frac{\alpha_1+\alpha_2}{2}\right)=\frac{\alpha_1}{2} \qquad \textbf{6.4}$$

$$\Delta\alpha_1=\left(\alpha_1-\alpha_{ave}\right)=\alpha_1-\frac{\alpha_1}{2}=\frac{\alpha_1}{2}=\alpha_{ave} \qquad \textbf{6.5}$$

So $\Delta\alpha_1.d$ will be the average absorption of the grating, which can be considered similar to the experimentally measured value of the absorption in the spectra as shown in Figure 6.4 for the calculation purpose. Similarly, if the refractive index of the grating medium (Ag embedded in gelatin) and air are written as $n_{(Ag+gelatin)}=n_1$ and $n_{(air)}=n_2=1$ respectively, then the average refractive index (n_{ave}) and the modulation in refractive index Δn_1 can be written as

$$n_{ave}=\left(\frac{n_1+n_2}{2}\right) \qquad \textbf{6.6}$$

$$\Delta n_1=\left(n_1-n_{ave}\right) \qquad \textbf{6.7}$$

The DE of the gratings has been calculated using equation 6.3 for all the gratings (10, 15 and 30 keV) taking corresponding absorption values ($\Delta\alpha_1.d$) as measured experimentally (Figure 6.4). In this calculation values of n_1 is varied from 1.52 (pure gelatin) to 1.8 (equation 6.7) for each of the gratings to see the variation in their DE(λ) profiles. Here, it is assumed that after the fabrication of the grating refractive index of the pure gelatin increases because of the presence of Ag content in it. An increase in the refractive index of the polymers has also been reported after electron beam irradiation [35].

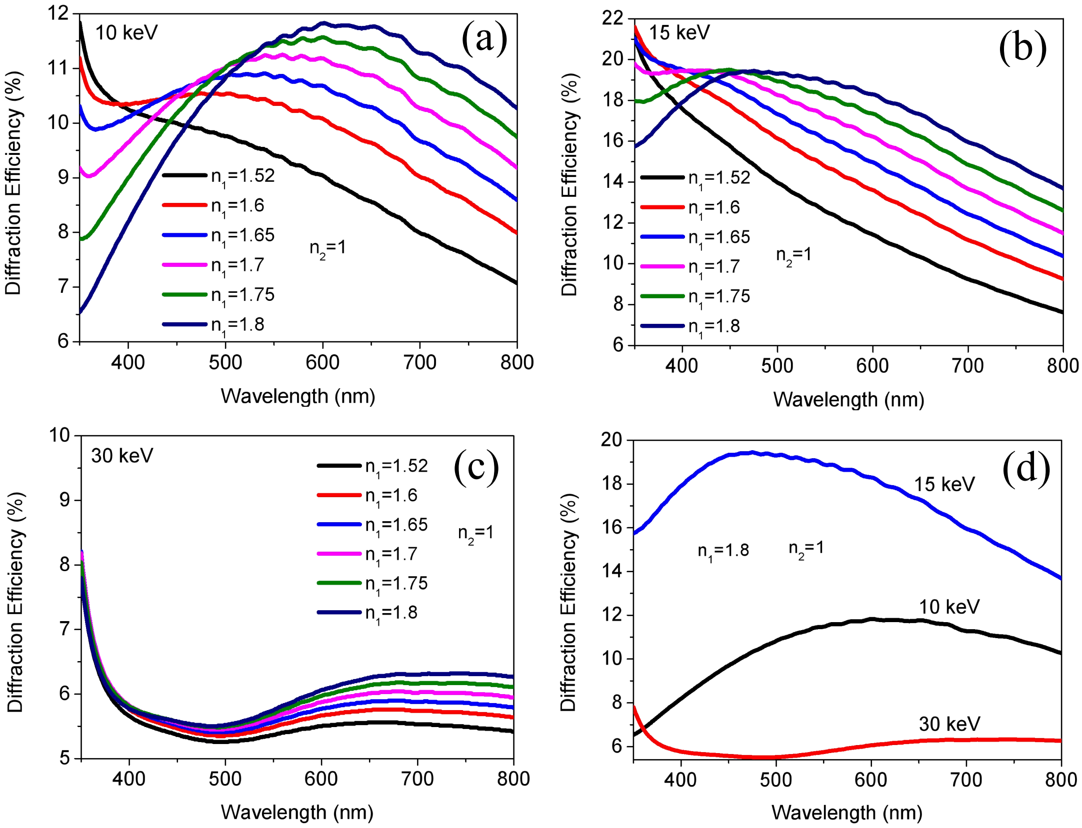

Figure 6.7 Variation in the simulated diffraction efficiency (based on Raman-Nath theory) of 10 μm period gratings with change in the refractive index of the medium (from 1.52 to 1.80) for gratings fabricated at (a) 10 keV, (b) 15 kV and (c) 30 keV electron beam energies.

The theoretically calculated DE profiles of the gratings fabricated at 10, 15 and 30 keV are shown in Figures 6.7(a)-6.7(c) respectively. In the case of 10 keV grating, the DE consistently decreases with an increase in the wavelength for n_l=1.52 (Figure 6.7(a)). However, a broad peak develops and shifts to higher wavelength side with an increase in the values of n_l from 1.52 to 1.80 (Figure 6.7(a)). Similar variation in DE profiles is noted in the case of 15 keV grating (Figure 6.7(b)). However, profiles show a drastic change in the case of 30 keV grating as shown in Figure 6.7(c). Particularly, the DE decreases with a shift in its peak towards higher wavelength side.

TABLE 6.2: The data of the gratings used for simulation of the diffraction efficiency best matching with the experimental results.

Exposure energy (keV)	Grating thickness d (nm)	Refractive index of grating n_1	Refractive index of air n_2	n_{ave}	Δn_1	DE η (%)	Peak position (nm)
10	400	1.8	1	1.4	0.4	11.8	600
15	350	1.8	1	1.4	0.4	19.4	450
30	300	1.8	1	1.4	0.4	6.2	800

Figure 6.7(d) shows the simulated DE curve best fitting (obtained from Figures 6.7(a)-6.7(c)) with the experiential observations (Figure 6.6) for all the three gratings. These plots have been generated by using the values mentioned in Table 6.2 for each type of gratings. Figure 6.7(d) shows that the 10 keV grating has large DE compared to 30 keV as has been observed experimentally, whereas the profiles are qualitatively matching with the experimental results (Figure 6.6). The simulated curve for 30 keV grating shows lowest DE at ~484 nm whereas 15 keV grating shows maximum DE at 450 nm. These features are also in agreement with the experimentally observed DE results. As discussed in the introduction section that periodic variation in the refractive index (n) is the main responsible parameter for diffraction phenomenon. For metal nanoparticle gratings, periodic variation in particle size, number density and periodic variation in surrounding medium of nanoparticle show periodic variation in the absorption coefficient (α) due to LSPR excitation based enhanced absorption and scattering. The periodic variation in absorption coefficient also show diffraction phenomenon. When spacial modulation of both refractive index variation and absorption coefficient variation matches with zero phase difference then diffraction efficiency enhances. In the present case also the PNG structures have zero phase difference between variation in (n) and (α), That is why only PNG structures

shows enhanced diffraction efficiency. However, the overall values of DE (simulated) are higher in comparison to the experimentally observed values that may be due to increased losses occurred as a result of dominant reflection and the scattering process by various interfaces which are not incorporated in the derivation of the theoretical formulations. The qualitative agreement between experimentally observed DE profiles with numerically calculated profiles indicates that the Raman-Nath theory could explain the trends in DE of the PNG gratings. However, further improvement in the formulation of Raman-Nath theory is needed to explain variation in the amplitude of the transmission DE by including various loss terms.

6.6 Conclusions

A good quality and efficient surface relief plasmonic nanoparticle gratings (PNG) has been successfully fabricated by electron beam lithography technique using silver halide (AgBr) based electron microscope film as a substrate and the conventional scanning electron microscope (SEM) as a fabrication tool. Tunable optical diffraction efficiency (DE) along with significantly flat diffraction BW for plasmonic surface relief transmission grating (PSRTG) have been observed due to variation in the grating period and amount of silver (Ag) nanoparticles. First order DE and band width (BW) are measured as 4% and 400 nm in the visible range for the 10 μm period of the grating. The DE and BW are reduced to 0.03 % and 100 nm for 3.4 μm periodicity. The reduction in DE and narrowing in BW are found to be correlated with the localized surface plasmon resonance (LSPR) of Ag nanoparticle embedded in the grating itself and its period respectively. The nature of DE profile was found to be significantly flattened for each of the structure within the BW. Such control on the DE and BW of PSRTG opens up the possibility of potential applications in various optical devices like a band-pass filter for the visible spectral range. The morphological characterization of the gratings fabricated by varying the exposure energy shows that the grating fabricated by 15 keV accelerated electron beam does not have any constant absorbing layer of Ag nanoparticles between the PET and the grating. Absorption spectra of all the gratings show the presence of LSPR having different amplitude and broadening depending on the fabrication process which decides the geometrical parameters of the gratings. The absorption of gratings increases due to increase in the number density of Ag nanoparticles, whereas broadening and shift in the peaks towards higher wavelength side seem to be due to an increase in the size of Ag nanoparticles as well as due to decrease in the inter-particle separation. Maximum DE of ~7.2 % was found in the first order from the grating fabricated by 15 keV electron beam.Variation in the diffraction efficiencies is found correlated with the changes in the geometrical parameters and the corresponding absorption profiles of the gratings. A good qualitative agreement between the experimental DE profile and the theoretical calculation based on the Raman-Nath diffraction theory shows that the profiles of the LSPR of the gratings play an important role in deciding the profile of the DE of PNG gratings.

References:

[1] Heinz Raether, *Surface plasmons on smooth and rough surfaces and on gratings*. Verlag: Springer, 1986.

[2] C. Palmer, *Diffraction grating handbook*, no. 6th edition. Rochester, New York: Newport Corporation, 2005.

[3] H. Kogelnik, “Coupled wave theory for thick hologram gratings,” *Bell Syst. Tech. J.*, vol. 48, no. 9, pp. 2909–2947, 1969.

[4] W. R. Klein and B. D. Cook, “Unified approach to ultrasonic light diffraction,” *IEEE Trans. Sonics Ultrason.*, vol. 14, no. 3, pp. 123–134, 1967.

[5] F. G. Kaspar, “Diffraction by thick, periodically stratified gratings with

complex dielectric constant," *J. Opt. Soc. Am.*, vol. 63, no. 1, pp. 37–45, 1973.

[6] R. Magnusson and T. K. Gaylord, "Analysis of multiwave diffraction of thick gratings," *J. Opt. Soc. Am.*, vol. 67, no. 9, pp. 1165–1170, 1977.

[7] R. Magnusson and T. K. Gaylord, "Diffraction regimes of transmission gratings," *J. Opt. Soc. Am.*, vol. 68, no. 6, pp. 809–814, 1978.

[8] R. Magnusson and T. K. Gaylord, "Diffraction efficiencies of thin absorption and transmittance gratings," *Opt. Commun.*, vol. 28, no. 1, pp. 1–3, 1979.

[9] T. K. Gaylord and M. G. Moharam, "Thin and thick gratings: terminology clarification," *Appl. Opt.*, vol. 20, no. 19, pp. 3271–3273, 1981.

[10] U. Kreibig and M. Vollmer, *Optical properties of metal clusters*. Berlin: Springer, 1995.

[11] B. Yan, A. Thubagere, W. R. Premasiri, L. D. Ziegler, L. D. Negro, and B. M. Reinhard, "Engineered SERS substrates with multiscale signal enhancement: nanoparticle cluster arrays," *ACS Nano*, vol. 3, no. 5, pp. 1190–1202, 2009.

[12] M. Panagopoulou, N. Pantiskos, P. Photopoulos, J. Tang, D. Tsoukalas, and Y. S. Raptis, "Raman enhancement of rhodamine adsorbed on Ag nanoparticles self-assembled into nanowire-like arrays," *Nanoscale Res. Lett.*, vol. 6:629, pp. 2–7, 2011.

[13] J. Gao, H. Qian, S. Xu, and M. Han, "Investigation of 1D siliver nanoparticle arrays for use as molecule concentration-specific SERS substrates," *J. Nanomater.*, vol. 989803, pp. 1–8, 2013.

[14] M. Geissler, K. Li, B. Cui, L. Clime, and T. Veres, "Plastic substrates for surface-enhanced raman scattering," *J. Phys. Chem. C*, vol. 113, pp. 17296–17300, 2009.

[15] J. M. Bingham, J. N. Anker, L. E. Kreno, and R. P. Van Duyne, "Gas sensing with high-resolution localized surface plasmon resonance spectroscopy," *J. Am. Chem. Soc.*, vol. 132, pp. 17358–17359, 2010.

[16] W. C. Hung, W. H. Cheng, M. S. Tsai, Y. C. Juan, I. M. Jiang, and P. Yeh, "Surface plasmon enhanced diffraction in cholesteric liquid crystals," *Appl. Phys. Lett.*, vol. 90, no. 183115, pp. 1–3, 2007.

[17] W. C. Hung, W. H. Cheng, M. S. Tsai, W. C. Chung, I. M. Jiang, and P. Yeh, "Laser pulse induced gold nanoparticle gratings," *Appl. Phys. Lett.*, vol. 93, no. 6, 2008.

[18] W. C. Hung, W. H. Cheng, T. K. Liu, I. M. Jiang, M. S. Tsai, and P. Yeh, "Diffraction of cholesteric liquid crystal gratings probed by monochromatic light from 450 to 750 nm," *J. Appl. Phys.*, vol. 104, no. 7, pp. 10–14, 2008.

[19] T. K. Liu, W. C. Hung, M. S. Tsai, C. Y. Tseng, and I. M. Jiang, "Sensible

measurement of localized surface plasmon based on lithographic gratings," *Proc. SPIE - Int. Soc. Opt. Eng.*, no. 71352I, pp. 1–11, 2008.

[20] T. K. Liu, W. C. Hung, M. S. Tsai, Y. C. Tsao, and I. M. Jiang, "Fabrication of tunable grating with silver nanoparticles," *Proc. SPIE*, vol. 7390, no. 73901A, pp. 1–9, 2009.

[21] T. Hirose *et al.*, "Diffraction efficiency of holographic grating: Formed in Au nano particle-doped sol-gel silica film by laser irradiation," *Jan J. Appl. Phys.*, vol. 42, no. 3, pp. 1288–1289, 2003.

[22] M. Sugiyama *et al.*, "Optical recording media using laser-induced size reduction of Au nanoparticles," *Appl. Phys. Lett.*, vol. 79, no. 10, pp. 1528–1530, 2001.

[23] C. Li *et al.*, "Improvement of volume holographic performance by plasmon-induced holographic absorption grating," *Appl. Phys. Lett.*, vol. 102, no. 6, pp. 3–5, 2013.

[24] C. Li, L. Cao, Q. He, and G. Jin, "Holographic kinetics for mixed volume gratings in gold nanoparticles doped photopolymer," *Opt. Express*, vol. 22, no. 5, p. 5017, 2014.

[25] K. A. Willets and R. P. Van Duyne, "Localized surface plasmon resonance spectroscopy and sensing," *Annu. Rev. Phys. Chem.*, vol. 58, no. 4:35, pp. 267–97, 2007.

[26] W. C. Hung, W. H. Cheng, Y. S. Lin, D. J. Jang, I. M. Jiang, and M. S. Tsai, "Surface plasmons induced extra diffraction band of cholesteric liquid crystal grating," *J. Appl. Phys.*, vol. 104, no. 6, pp. 1–5, 2008.

[27] Sudheer *et al.*, "Fabrication of large area plasmonic nanoparticle grating structure on silver halide based transmission electron microscope film and its application as a surface enhanced Raman spectroscopy substrate," *J. Appl. Phys.*, vol. 118, no. 64303, pp. 1–9, 2015.

[28] F. Stellacci *et al.*, "Laser and electron-beam induced growth of nanoparticles for 2D and 3D metal patterning," *Adv. Mater.*, vol. 14, no. 3, pp. 194–198, 2002.

[29] C. Noguez, "Surface plasmons on metal nanoparticles: The influence of shape and physical environment," *J. Phys. Chem. C*, vol. 111, no. 10, pp. 3806–3819, 2007.

[30] V. N. Rai, A. K. Srivastava, C. Mukherjee, and S. K. Deb, "Surface enhanced absorption and transmission from dye coated gold nanoparticles in thin films," *Appl. Opt.*, vol. 51, no. 14, pp. 2606–2615, 2012.

[31] T. Rasmussen, "Overview of high-efficiency transmission gratings for molecular spectroscopy," *Spectroscopy*, vol. 29, no. 4, pp. 32–39, 2014.

[32] M. G. Moharam and L. Young, “Criterion for Bragg and Raman-Nath diffraction regimes,” *Appl. Opt.*, vol. 17, no. 11, pp. 1757–1759, 1978.

[33] A. Nath and S. C. V Raman, “The diffraction of light by supersonic waves,” *Proc. Indian Acad. Sci.*, vol. 8, pp. 499–503, 1938.

[34] T. M. de Jong, D. K. G. de Boer, and C. W. M. Bastiaansen, “Surface-relief and polarization gratings for solar concentrators,” *Opt. Express*, vol. 19, no. 16, p. 15127, 2011.

[35] S. Asha, Y. Sangappa, and S. Ganesh, “Tuning the refractive index and optical band gap of silk fibroin films by electron irradiation,” *J. Spectrosc.*, vol. 879296, pp. 1–7, 2015.

Chapter 7

Conclusions and future work

7.1 Conclusions

In this thesis, we have presented the studies on fabrication and characterization of nanostructured metallic thin films and periodic structures for plasmonic applications. The nanostructured metallic thin films and periodic structures exhibit a variety of technological applications due to extraordinary excitation of localized surface plasmon resonance (LSPR) [1]. For example, nanostructured metallic thin films are frequently used for surface-enhanced Raman spectroscopy (SERS), chemical and biological sensor, and solar cells [2], [3]. The use of periodic metallic structures is often for the nanophotonic circuitry for the light transport at the nanoscale [4]. Recently, tuning and enhancement in the optical diffraction efficiency of grating structures are also attempted using incorporation of LSPR supported nanoparticles, which also added the interest in such plasmonic nanostructures [5]. In this direction, the prime motivations of the thesis are to investigate growth mechanism and solid-state dewetting dynamics of nanostructured gold (Au) thin films and investigate the instability in the LSPR response of the nanostructured Au thin films against aging at ambient temperature followed by exploring the possible reasons behind the process. On the other hand, the investigation of direct method for the fabrication of large area plasmonic nanoparticle periodic structures in short time for SERS substrate and possible tunability in optical diffraction efficiency of grating.

The morphological investigations carried out by ex-situ transmission electron microscope (TEM) imaging of Au thin film exhibits verity of plasmonic nanostructures (island, percolated and continuous) depending upon the deposition flux and the deposition time. The morphological quantification of nanostructures is performed by analyzing the TEM images in terms of real space parameters (RSP) like particle size, standard deviation in size, circularity, number density, covered area fraction (CAF) (percentage filling factor of the Au film F%) and inter-particle gap. The quantification suggests that for thickness less than ~3 nm isolated spherical particles are formed. The detailed study of post-deposition annealing carried out by in-situ TEM for investigations of dewetting dynamics also suggest that island film having particle size ~9 nm is found highly stable. The circularity of these particles is found maximum ~0.77, which is desirable for plasmonic application to get a narrower optical response. Electron diffraction spectra for the growth and post-deposition annealing (dewetting) of Au thin film is also recorded. During growth only (111) crystal plane appear for island film and other low spacing crystal planes appear for percolated and continuous film. It is also observed that continuous ring in electron diffraction for percolated film converts into a discrete spot during dewetting, which shows that random orientation of the Au grains reduces and grain size significantly increases.

We have performed absorption spectroscopy study for the island, percolated and continuous Au thin films (0.7 nm to 28.2 nm thickness range) grown on a glass substrate, and it is concluded that these nanostructured thin films show a highly unstable plasmonic response on aging even at room temperature. The island film shows ~70 nm blue shift in LSPR peak position and 105 nm reduction in its broadening on 120 days aging. After that, no variation in the optical response of island film is recorded. The dynamics of the instability in the plasmonic response is drawn in terms of rate of blue shift in the plasmonic peak for island film which follow the single exponential decay function having about 20 days time constant. The percolated films also show the similar plasmonic instability but within 30 days of aging, its plasmonic response become stable. Contrary to the behaviour of percolated film, continuous film shows the appearance of significant plasmonic signature near 600 nm after 30 days of aging. The strength of this plasmonic response in continuous thin film increase with aging time. Our analysis shows that instability in the plasmonic response is due to the existence of natural solid-state dewetting and crystallization in nanostructured Au thin film at room temperature. The x-ray reflectivity (XRR), atomic force microscopy (AFM) and grazing incidence x-ray diffraction (GIXRD) were used to verify the existence of natural solid-state dewetting and crystallization in these Au nanostructured thin films. The microstructural studies performed on these island and percolated Au thin films tells that during natural solid-state dewetting reshaping occurs in the nanostructures in which lateral dimensions decreases and vertical dimensions increases. The reshaping in nanostructures also results in enhancement of inter-island gap and reduction in the particle to substrate interface area. The size variation and reshaping in the island and percolated nanostructure during natural solid-state dewetting are the main reasons for change in its plasmonic response. In case of continuous film, voids of about 50 nm in size are formed after 30 days of aging. The size and density of voids increase with aging. These voids can excite LSPR in the Au film and show new plasmonic band in the absorbance spectra. XRR also revels corroborative results to the above microscopy studies which enable us to draw schematic for the mechanism of morphological evolution for natural solid-state dewetting. The GIXRD results show enhancement of crystallization for all thickness of Au films. Minimum thickness film shows maximum enhancement in the crystallization. Finally, the aged films are used as a SERS substrate, in which it has been observed that Raman signal of Rodamine6G (R6G) coated Au thin film substrate shows large enhancement in comparison to the island and percolated film.

A direct method for fabrication of large area (12.5 mm^2) plasmonic nanoparticle grating structures in very short time (19 s) has been developed using conventional SEM on silver halide (AgBr) based film. The period of the grating is mainly controlled by the variation in its exposure and lines per frame at a fixed magnification. The mechanism of the fabrication process and the difference in the period and height of the grating obtained by the AFM are explained by the schematic, which suggests that overlapping of interaction volume of the electron beam in case of low period grating reduces the height of the grating. The results of energy dispersive spectroscopy depict the presence of only Ag in the fabricated structures. The absorption spectroscopy renders the variation in nanoparticle number density. The fabricated nanoparticle grating structures of the different period are used as a SERS substrate. It is concluded that the fabricated grating structures found as a superior SERS substrate in comparison to nanostructured thin film. The 10 μm period grating provides an enhancement by two orders of magnitude in comparison to the sputtered deposited silver (Ag) nanoparticle film. As the period of the grating reduces from10 μm to 2.5 μm additional three-time enhancement in the SERS signal is achieved.

The fabrication process is extended for variation in height and shape of nanoparticle grating structures (fixed period) using change in the energy of electron beam. These plasmonic gratings found application in tuning the optical diffraction efficiency (2.8 to 7.2 %) as well as bandwidth (200-400 nm). Maximum 7.2% optical diffraction efficiency is achieved for grating fabricated at 15 keV. The explanation of tuning in the optical diffraction efficiency is also supported by the theoretical simulation of Raman-Nath diffraction efficiency of the grating.

7.2 Future work

Effect of texturing on the plasmonic properties of Au thin film during growth and dewetting is a new and exciting study. The study of aging effect on nanostructured thin film substrate for SERS application now demands to be examined for application purpose. The initial results of large SERS signal for drop coated R6G on aged Au continuous film in comparison to the island and percolated film may provide a better substrate along with some deeper information about the engineering of SERS substrate for desired sensitivity. As, it has been observed that in case of periodic plasmonic structures, large area grating can be fabricated in a short time using AgBr based films and large SERS signal is recorded for lower period grating. In this direction, it will be quite interesting to investigate further reduction of the Ag grating period by reducing the initial thickness of the AgBr layer. So that, only neck region of exposing electron beam interact with AgBr layer which results in the fabrication of lower period Ag nanoparticle grating. Moreover, crossed grating fabricated by the double exposure on the AgBr based film can provide a 2D-nanoparticle array which may further increase the sensitivity of PNG structure. Further, incorporation of shape parameters in the simulation of optical diffraction efficiency of grating structures is quite useful for quantitative explanation of tuning and enhancement of experimentally observed results.

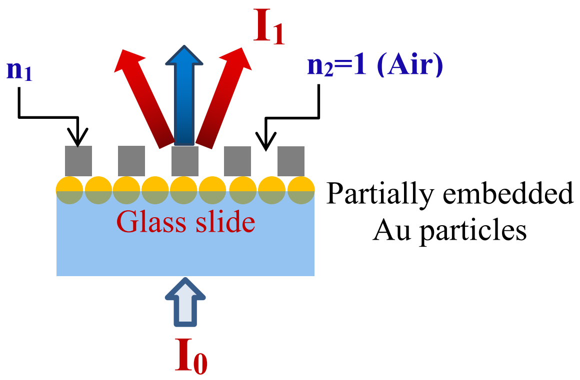

Figure 7.1. Schematic of nanoparticle grating fabricated on the glass substrate. The n_1 and n_2 are the refractive indexes of dielectric medium and air respectively.

Understanding gained from the present work will be used to design nanoparticle grating as presented in Figure 7.1. This will be useful for investigation of optical diffraction efficiency tuning.

Reference:

[1] X. Liu *et al.*, "Tunable dipole surface plasmon resonances of silver nanoparticles by cladding dielectric layers," *Sci. Rep.*, vol. 5:12555, pp. 1–7, 2015.

[2] G. Q. Liu *et al.*, "Surface-enhanced Raman scattering effect of gold nanoparticle arrays: The influence of annealing temperature, excitation power and array thickness," *Optik*, vol. 124, pp. 5124– 5126, 2013.

[3] Y. Akimov *et al.*, "Enhancement of optical absorption in thin-film solar cells through the excitation of higher-order nanoparticle plasmon modes," *Opt. Express*, vol. 17, no. 12, pp. 10195–10205, 2009.

[4] Mark L. Brongersma Pieter G. Kik, *Surface Plasmon Nanophotonics*. Netherlands: Springer, 2007.

[5] W. C. Hung, W. H. Cheng, M. S. Tsai, W. C. Chung, I. M. Jiang, and P. Yeh, "Laser pulse induced gold nanoparticle gratings," *Appl. Phys. Lett.*, vol. 93, no. 6, 2008.